Journal of Materials Chemistry A

ROYAL SOCIETY OF CHEMISTRY

REVIEW

View Article Online
View Journal

Cite this: DOI: 10.1039/c9ta11618d

Biomass-derived porous graphitic carbon materials for energy and environmental applications

Qiang Chen, [ab] Xiaofei Tan, *[ab] Yunguo Liu, *[ab] Shaobo Liu,[cd] Meifang Li,[ab] Yanling Gu,[e] Peng Zhang,[ab] Shujing Ye,[ab] Zhongzhu Yang[ab] and Yuanyuan Yang[ab]

As we all know, environmental protection and sustainable energy utilization are significant challenges for us. Due to their many excellent characteristics, carbon materials have been playing a very important role in energy and environmental applications. Biomass is the only renewable carbon source and crucial precursor of carbonaceous materials and has the advantages of a unique structure, a wide range of sources, biodegradability, and low cost. Developing high-performance carbonaceous materials from biomass is a significant research subject. Biomass-derived porous graphitic carbon materials (BPGCs) have received extensive attention as novel high-performance sustainable carbon materials owing to its well-developed porous structure, good graphitic structure, and heteroatom doping. Here, this review firstly focuses on the principal synthesis methodologies of BPGCs. Next, three electrochemical energy storage and conversion systems that utilize BPGCs are intensively investigated, including supercapacitors (SCs), lithium-ion batteries (LIBs) and fuel cells (FCs). Then, BPGCs are further reviewed in terms of their application in the field of environmental protection, which is also the first systematic summary of BPGCs in environmental applications. Finally, this review points out the direction that is worthy of further research in the future and the essential issues that have not yet been resolved.

Received 22nd October 2019
Accepted 23rd January 2020

DOI: 10.1039/c9ta11618d

rsc.li/materials-a

[a]College of Environmental Science and Engineering, Hunan University, Key Laboratory of Environmental Biology and Pollution Control, Ministry of Education, Changsha, Hunan 410082, PR China. E-mail: tanxf@hnu.edu.cn; liuyunguo@hnu.edu.cn; Fax: + 86 731 88822829; Tel: + 86 731 8373151124

[b]Key Laboratory of Environmental Biology and Pollution Control, Ministry of Education, Hunan University, Changsha 410082, PR China

[c]College of Metallurgy and Environment, Central South University, Changsha 410083, PR China

[d]College of Architecture and Art, Central South University, Changsha 410083, PR China

[e]College of Materials Science and Engineering, Changsha University of Science and Technology, Changsha 410114, PR China

1 Introduction

With the depletion of fossil energy, global warming and increasing environmental pollution, energy and environment have become the focus of the international community. In the face of increasingly severe global energy and environmental problems, the development and utilization of new and renewable energy sources have become the common choice for countries around the world to ensure energy security, combat climate change, and achieve sustainable development. Among

Qiang Chen received his B.S. in environmental engineering from the Guilin University of Technology in 2014. He is currently a postgraduate student under the supervision of Prof. Yunguo Liu at the College of Environmental Science and Engineering, Hunan University, China. His current research includes the preparation of porous graphitic carbon materials derived from biomass and their application in energy and environmental protection.

Xiaofei Tan is an assistant professor at the College of Environmental Science and Engineering at Hunan University. He obtained his education from the Key Laboratory of Environmental Biology and Pollution Control (Hunan University), and earned his PhD in environmental engineering in 2017. His research interests include waste resource utilization, synthesis and application of functionalized carbon materials, water pollution control, and the application of advanced oxidation degradation.

them, supercapacitors, lithium-ion batteries and fuel cells are the most typical and popular electrochemical energy storage and conversion devices.[1,2] Moreover, due to the industrialization and long-term agricultural activities, the environmental quality has deteriorated and it is imperative to efficiently control and remove environmental pollutants.[3] In this context, developing high-efficiency and sustainable materials has shown significant prospects for environmental protection.

Numerous studies have shown that the application of carbon materials is an effective strategy for addressing major challenges of global energy consumption and environmental pollution.[4,5] Carbon materials have been the ideal candidate materials for electrochemical energy storage and conversion and environmental protection because of their diverse structure, rich surface, strong controllability and good chemical stability. In this regard, various types of carbon materials (such as biochar, carbon nanotubes, activated carbon, and graphene), have been extensively explored.[6–9] Porous carbon materials with a high specific surface area and good stability have been widely used as electrode materials for supercapacitors, lithium-ion batteries and fuel cells and as repair materials for environmental pollutant treatment.[10,11] However, at present, porous carbon materials have the following disadvantages: (i) poor graphitic structure and low degree of graphitization that are not conducive to the transmission of ions and electrons; (ii) underdeveloped porous structure and low effective specific surface area; (iii) lack of heteroatom doping. These problems have limited their further application in the field of energy storage and conversion and environmental protection.[5] Graphitic carbon materials have broad application prospects because of their excellent electrical conductivity, improved crystalline structure and unique physicochemical properties, which can facilitate ion diffusion and charge propagation.[12–14] However, graphitic carbon materials (*e.g.*, graphene) also have disadvantages such as high cost, complex synthesis and poor porous structure.[15] In conclusion, in order to overcome the bottleneck in the application of electrochemical energy storage and conversion and environmental protection, the key is to develop carbon materials with an excellent porous structure, graphitic structure and appropriate heteroatom doping. Therefore, it is very urgent to design green and efficient porous graphitic carbon materials through effective ways.

Biomass resources have been the promising carbon precursor of sustainability, economy, and availability to deal with environmental and energy issues.[16–19] Firstly, Biomass-derived carbon materials have inherently unique porous structure. The diversity of biomass provides a broader research space, and the beneficial components and delicate structures of biomass can be fully utilized. Secondly, plentiful biomass contains oxygen, nitrogen, potassium and other elements, which can be doped as heteroatoms, allowing for the generation of additional active sites and acting as a catalyst or activation agent for the subsequent processing process. Thirdly, most biomass comes from agroforestry waste or daily life waste, which greatly highlights environmental and economic advantages. Biomass-derived porous graphitic carbon materials (BPGCs) have three representative characteristics of a porous structure, graphitic structure and heteroatom doping derived from biomass or foreign dopants (Fig. 1), in which heteroatom doping is not necessary and appropriate heteroatom doping is very desirable for the application of BPGCs. Currently, biomass-derived porous graphitic carbon materials (BPGCs) have attracted great interest for electrochemical energy storage and conversion and environmental protection.

2 Fabrication of BPGCs

At present, the preparation approaches of BPGCs can be mainly divided into pyrolysis, chemical activation, catalytic graphitization and catalytic graphitization combined with chemical

Yunguo Liu is currently a professor at the College of Environmental Science and Engineering at Hunan University. He received his PhD from the Shanghai Institute of Physiology and Ecology, Chinese Academy of Sciences in 1998. After that, he worked as a senior research fellow at Kyoto University and Tokyo A&M University, Japan. His research interests include the synthesis and application of functionalized carbon materials, environmental and ecological restoration theory and technology, and ecological environment planning.

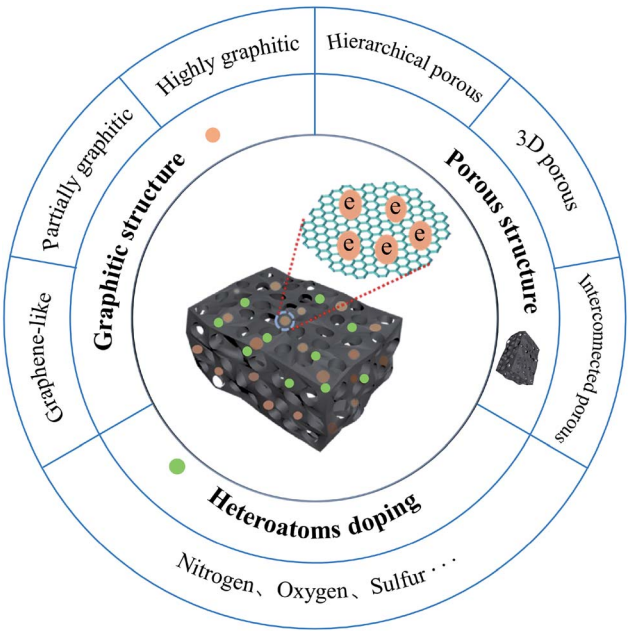

Fig. 1 Schematic diagram showing the structure and properties of BPGCs. Adapted with permission from ref. 251. Copyright 2019 Springer.

Table 1 Feedstocks, structures, properties and synthesis methods reported for BPGCs (P = pyrolysis method, CA = chemical activation method, and CG = catalytic graphitization method)

Biomass	Pre-activation treatment	Synthesis method	Activation catalyst	Graphitic catalyst	S_{BET}[a] (m^2 g^{-1})	Porous structure	Graphitic structure	Ref.
Microalgae	—	P	—	—	29.4	Hierarchical porous structure	A large number of microcrystalline graphitic domains	27
Coffee ground	—	P	—	—	438	Porous structure	Excellent degree of graphitization	248
Spirulina	—	P	—	—	117.9	Hierarchical porous structure	Highly graphitic carbon	242
Hemp bast fiber	Hydrothermal carbonization	CA	KOH	—	1505	Highly interconnected carbon nanosheets, porous structure	Partially graphitic structure	252
Willow catkin	—	CA	KOH	—	645	Three-dimensional porous network structure	High graphitization degree	138
Pomelo peel	Pre-carbonization	CA	KOH	—	2167	Highly microporous structure	High graphitization degree	253
Shell of broad beans	Pre-carbonization	CA	KOH	—	655.4	Highly developed hierarchical porosity network	The presence of graphitic domains	254
Green tea waste	Pre-carbonization	CA	KOH	—	1057.8	Interconnected structure of ultrathin nanoflakes	Relatively high degree of graphitization	50
Pitch pine sawdust	Pre-carbonization	CA	KOH	—	3248	Porous structure	Partially graphitic structure	49
Bamboo	Pre-carbonization	CA	KOH	—	171.5	Hierarchical porous structure	Relatively high degree of graphitization	255
Dry elm samara	—	CA	KOH	—	1947	Three-dimensional scaffolding frameworks of highly porous carbon nanosheets	Partial graphitization	256
Sugarcane bagasse	Pre-carbonization	CA	KOH	—	1786.1	Large-size multiscale wrinkled nanosheet architecture	Short-range graphite lattice fringes	257
Spruce bark	Hydrothermal carbonization	CA	KOH	—	2385	Hierarchical porous structure, 3D interconnected structure	3D vertically aligned graphene nanosheet arrays	130
Mung bean husk	Hydrothermal carbonization	CA	KOH	—	1214	3D hierarchical porous structure	Low degree of graphitization	47
Oil-tea seed shell	Pre-carbonization	CA	$NaNH_2$	—	2965.7	Hierarchical porous systems	Layered graphene-like structures	60
Cork	—	CA	$KMnO_4$	—	831	Hierarchical porous structure	Low graphitization degree	139
Soybean	—	CA	KOH	—	1089.84	Three-dimensional connected porous structure	Graphitic nano-crystals	258
Eulaliopsis binata	Pre-carbonization	CA	KOH	—	2273	Porous structure with balanced micropores and mesopores	Localized graphitic structure	259
Enteromorpha	Pre-carbonization	CA	KOH	—	638.116	Porous structure	Highly graphitic nanosheets	57
Garlic skin	Pre-carbonization	CA	KOH	—	2818	3D hierarchical porous structure	Graphene-phase carbon	51
Softwood sawdust	—	CG	—	$Fe(NO_3)_3$	220	Porous structure	Nanostructured tubular graphitic carbon	69
Coconut shell	—	CG	—	$Fe(NO_3)_3$	—	3D interconnected carbon framework with a hierarchical porous structure	Locally interconnected graphitic nanostructures	84

Table 1 (*Contd.*)

Biomass	Pre-activation treatment	Synthesis method	Activation catalyst	Graphitic catalyst	S_{BET}[a] ($m^2\ g^{-1}$)	Porous structure	Graphitic structure	Ref.
Sawdust	—	CG	—	$FeCl_3$	360.0	Magnetic nanofiber/ mesoporous carbon	The formation of graphitic carbon	97
Coconut shell	—	CA + CG	$ZnCl_2$	$FeCl_3$	1874	2D porous structure	Porous graphene-like nanosheets	91
Bamboo	—	CA + CG	K_2FeO_4	K_2FeO_4	1732	Continuous 3D porous frameworks	High graphitization degree	95
Willow catkin	—	CA + CG	$K_4Fe\ (CN)_6$	$K_4Fe\ (CN)_6$	1066.56	Porous graphitic carbon microtubes	High graphitic degree	260
Disposable chopstick	—	CA + CG	$K_2C_2O_4$	$Fe\ (NO_3)_3$	1651.9	3D interpenetrating porous structure	High graphitization degree	261
Shaddock skin	—	CA + CG	$ZnCl_2$	$FeCl_3$	2327	Hierarchical meso/ microporous systems	Interconnected graphitized carbon nanosheets	262
Coconut shell	—	CA + CG	K_2CO_3	K_2CO_3	1506.19	Three-dimensional porous structure	High degree of graphitization, graphene-like structure	98
Moringa oleifera stem	—	CA + CG	$ZnCl_2$	$FeCl_3$	2250	Hierarchically porous carbon nanosheets	Order structure with a good crystalline degree	94

[a] S_{BET} is the specific surface area calculated by the Brunauer–Emmett–Teller (BET) method.

activation methods. BPGCs have been manufactured from a variety of biomass sources through the four main methods. Table 1 lists some representative examples. It is relatively difficult to produce BPGCs from a wide range of biomass resources by pyrolysis alone, and only a small amount of literature has been reported. In comparison with other methods, chemical activation with potassium hydroxide (KOH) is a comparatively classic and the most widely used method for preparing BPGCs. In recent years, the preparation of BPGCs by simultaneous chemical activation and catalytic graphitization of biomass has gradually emerged and developed. In this section, according to the summary of relevant literature, we focus on the parameters of the method and biomass raw materials for synthesizing BPGCs and analyze their influence on the structure and properties of BPGCs (Fig. 2). Finally, we propose solutions and suggestions for achieving accurate and controlled preparation of BPGCs.

2.1 Pyrolysis

In general, the pyrolysis of biomass is considered as a thermochemical process, in which biomass is mostly converted into gases, liquid bio-oil and solid biochar under the conditions of complete oxygen deprivation or limited oxygen supply.[20–22] Specifically, slow pyrolysis of biomass is regarded as a necessary step to produce BPGCs and generally conducted at a slow heating rate of $\leq$10 °C min^{-1} within an inclusive range of temperatures (300–1000 °C) for a long retention time of the set pyrolysis temperature (>1 h). Biomass pyrolysis is a very complex physicochemical process, and its pyrolysis behavior is related to the characteristics of biomass, pyrolysis parameters, reactor conditions, *etc.*[23,24] There are many factors affecting biomass pyrolysis, which can be basically classified into two categories. One is related to reaction conditions (such as the pyrolysis temperature, heating rate and pyrolysis time), and the other is inextricably linked with raw material properties (for example types of biomass feedstocks, biomass characteristics and biomass particle size).[25] However, due to the complex structure and strong chemical bonds in biomass, it is not easy to prepare BPGCs with an excellent porous and graphitic structure. At present, only a few studies have demonstrated the preparation of BBGCs from biomass by using separate slow pyrolysis.[26]

For example, the pyrolysis of microalgae was carried out at 700 °C, 900 °C and 1100 °C, respectively, for 6 h at a heating rate of 10 °C min^{-1} under nitrogen gas (N_2) by Ru's group.[27] As a result, it was found that the pyrolysis product at 900 °C had many microcrystalline graphitic domains and a hierarchical porous structure. As shown in Fig. 3a–i, the porous structure of the pyrolysis product became more developed with the increase of pyrolysis temperature, especially the mesoporous structure. The increase of pyrolysis temperature might lead to the collapse of micropores formed in the early stage or the combination of micropores into mesopores and macropores. The increased pyrolysis temperature brought about more ordered graphitic carbon in the pyrolysis product (Fig. 3g–i). The X-ray diffraction (XRD) patterns of the obtained product confirmed that the

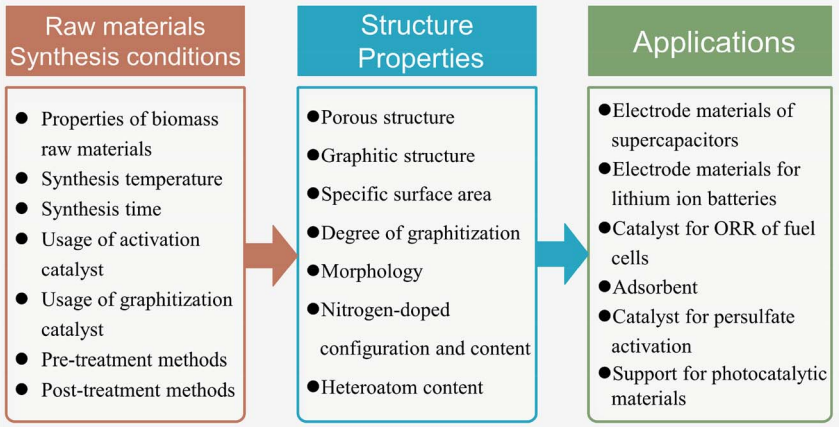

Fig. 2 A summary of the parameters that influence the structure and properties of BPGCs and their application.

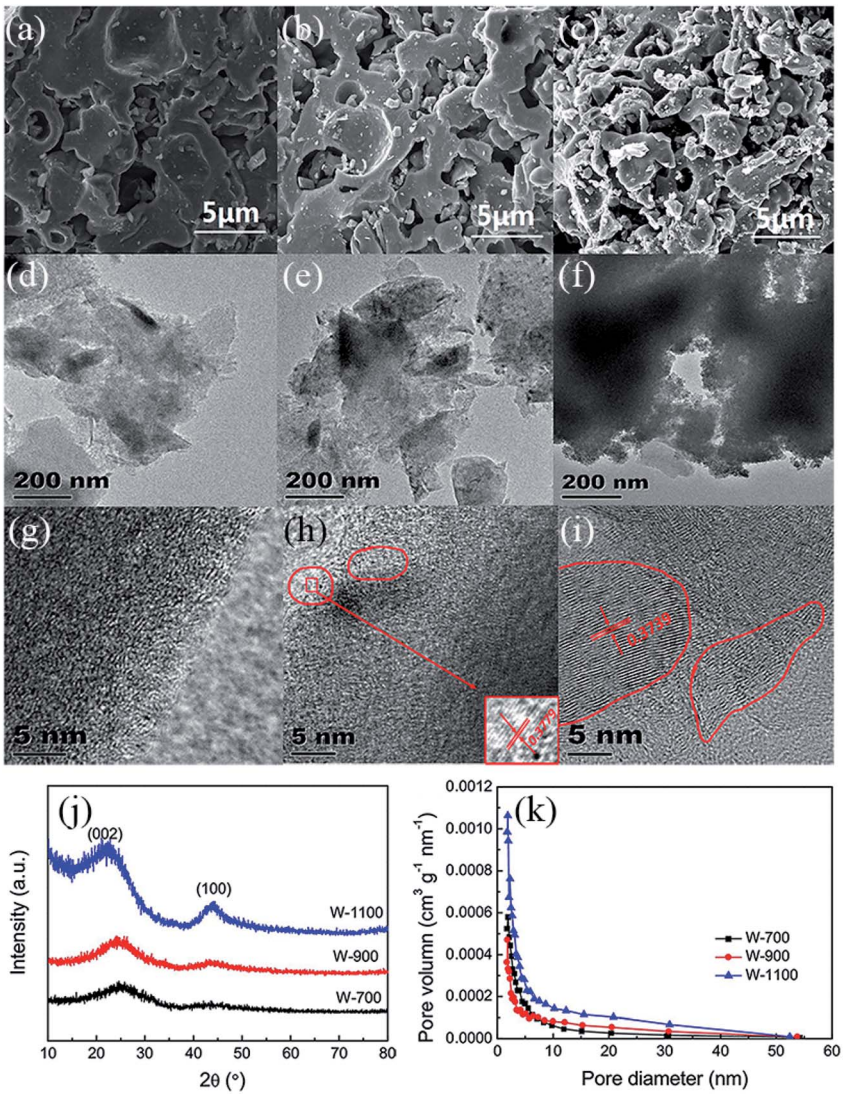

Fig. 3 (a) SEM, (d) TEM, and (g) HRTEM images of the pyrolysis product at 700 °C. (b) SEM, (e) TEM, and (h) HRTEM images of the pyrolysis product at 900 °C. (c) SEM, (f) TEM, and (i) HRTEM images of the pyrolysis product at 1100 °C. (j) The XRD patterns of the pyrolysis product. (k) Pore size distributions of the pyrolysis product. Reprinted with permission from ref. 27. Copyright 2016 Elsevier B. V.

product had more intensive and narrower XRD peaks with the increase of the pyrolysis temperature (Fig. 3j).[28] It was evident from Raman spectra that the integrated intensity ratio (I_G/I_D) of the G band to the D band increased as the pyrolysis temperature increased, indicating that the degree of graphitization became higher. The as-prepared product all showed a hierarchical porous structure, and the specific surface area and pore volume of the products increased significantly as the pyrolysis temperature increased (Fig. 3k).[27] The pyrolysis temperature has an important influence on the porous structure and graphitic structure of biomass.[29–31] Increasing the pyrolysis temperature within a certain range, the number of pores (especially micropores) and the specific surface area of biomass will increase, which is beneficial to the formation of a good porous structure.[32] At the same time, when the pyrolysis temperature increases, the graphitic structure of biomass will gradually develop, and the whole crystal structure tends to be orderly, resulting in an increase in the degree of graphitization.[33] Yu *et al.*[34] gained porous graphitic carbon (PSS-bio) by pyrolysis of shrimp shells at different temperatures. They also detected that pyrolysis temperature is the key element to regulate the porous structure and carbon configuration of PSS-bio. The elevation of pyrolysis temperature promoted the formation of hierarchically macro-/meso-/microporous structure and more graphitic carbon. It was worth noting that the removal order of impurities in biomass feedstocks had a significant impact on the porous structure of the product. As the degree of graphitization of the product increased, pyrrolic N in the product was converted to pyridinic N, which could be further converted into graphitic N. A study by Gao *et al.*[35] also revealed the influence of pyrolysis temperature on the nitrogen-doped configuration and content of BPGCs. At a higher temperature, the product obtained by pyrolyzing amaranth has a lower total nitrogen content. With the increase of pyrolysis temperature, the content of graphitic N and pyrrolic N increased, while the content of pyridinic N decreased. In the few reports available, the effect of pyrolysis temperature on the structure and properties of BPGCs prepared by slow pyrolysis alone has been highlighted. Other influencing factors such as the pyrolysis time, feedstock type and heating rate are rarely mentioned. The proper selection of biomass raw materials is the key to realizing the preparation of BPGCs by slow pyrolysis. The construction process of the porous structure and graphitic structure of biomass should be deeply understood to guide the expansion and further analysis of BPGC preparation by slow pyrolysis in the future.

2.2 Chemical activation

Slow pyrolysis is often considered as a necessary step in the fabrication of BPGCs. Most findings have revealed that BPGCs are less likely to be gained from the slow pyrolysis of biomass unless the pyrolysis is combined with another process (chemical activation or catalytic graphitization). Chemical activation strategies can be employed to further improve the porous structure and graphitic structure and increase the specific surface area (SSA) of biomass.[36,37] The chemical activation method is usually mixing the activator and biomass materials evenly in a certain proportion, followed by slow pyrolysis under the protection of an inert gas atmosphere.[32,38] The common activators are KOH, H_3PO_4, $ZnCl_2$ and K_2CO_3, among which KOH is the most popular chemical activator. By the same token, the chemical activation method based on the KOH activator is the most commonly used method to prepare BPGCs. At present, there are three main conclusions about the activation mechanism of KOH on carbon,[39] which have been widely accepted: (a) chemical activation process: several K-based compounds are used as activators to etch the carbon skeleton by an oxidation–reduction reaction with carbon, as shown in reactions (1)–(3), thus producing a well-developed porous structure.[40] (b) Physical activation process: H_2O generated by reaction (4) and CO_2 generated by reactions (5) and (6) in the activation system all etch carbon,[41–43] which contributes positively to the further development of the porosity of the carbon skeleton. (c) As shown in reactions (1), (7) and (2), the metal K obtained in the reaction can be effectively embedded into the lattice of carbon, thus causing lattice expansion.[44] When the inserted metal K and K-based compounds are removed by washing, the porous structure of carbon will be further enlarged.[44] The process of carbon activation by KOH involves chemical action, physical action, and carbon lattice expansion caused by inserting metal K into the carbon lattice. Multiple synergistic effects result in the formation of a porous structure and a high specific surface area.[32]

$$K_2O + C \rightarrow 2K + CO \quad (1)$$

$$6KOH + 2C \rightarrow 2K + 3H_2 + 2K_2CO_3 \quad (2)$$

$$K_2CO_3 + 2C \rightarrow 2K + 3CO \quad (3)$$

$$2KOH \rightarrow K_2O + H_2O \quad (4)$$

$$CO + H_2O \rightarrow CO_2 + H_2 \quad (5)$$

$$K_2CO_3 \rightarrow K_2O + CO_2 \quad (6)$$

$$K_2O + H_2 \rightarrow 2K + H_2O \quad (7)$$

The KOH activation process of biomass can be divided into two categories. The first type is direct one-step high-temperature activation accompanied by slow pyrolysis (*i.e.* carbonization) of the composite of biomass and KOH.[45] The two-step KOH activation method is more commonly used in preparing BPGCs in comparison with the one-step direct KOH activation. Biomass is always pre-activated by hydrothermal carbonization (HTC),[46] pre-carbonization, or chemical pretreatment before KOH activation. Ma's group[47] compared the effects of three different activation methods based on KOH on the structure and properties of the as-prepared products (Fig. 4a). Three-dimensional hierarchical porous carbon (3DHPC) was prepared from mung bean husk by hydrothermal carbonization combined with KOH activation, while the porous carbon (PC) obtained by pre-carbonization combined with KOH activation and the porous carbon block (PCB) obtained by hydrothermal carbonization combined with pre-carbonization

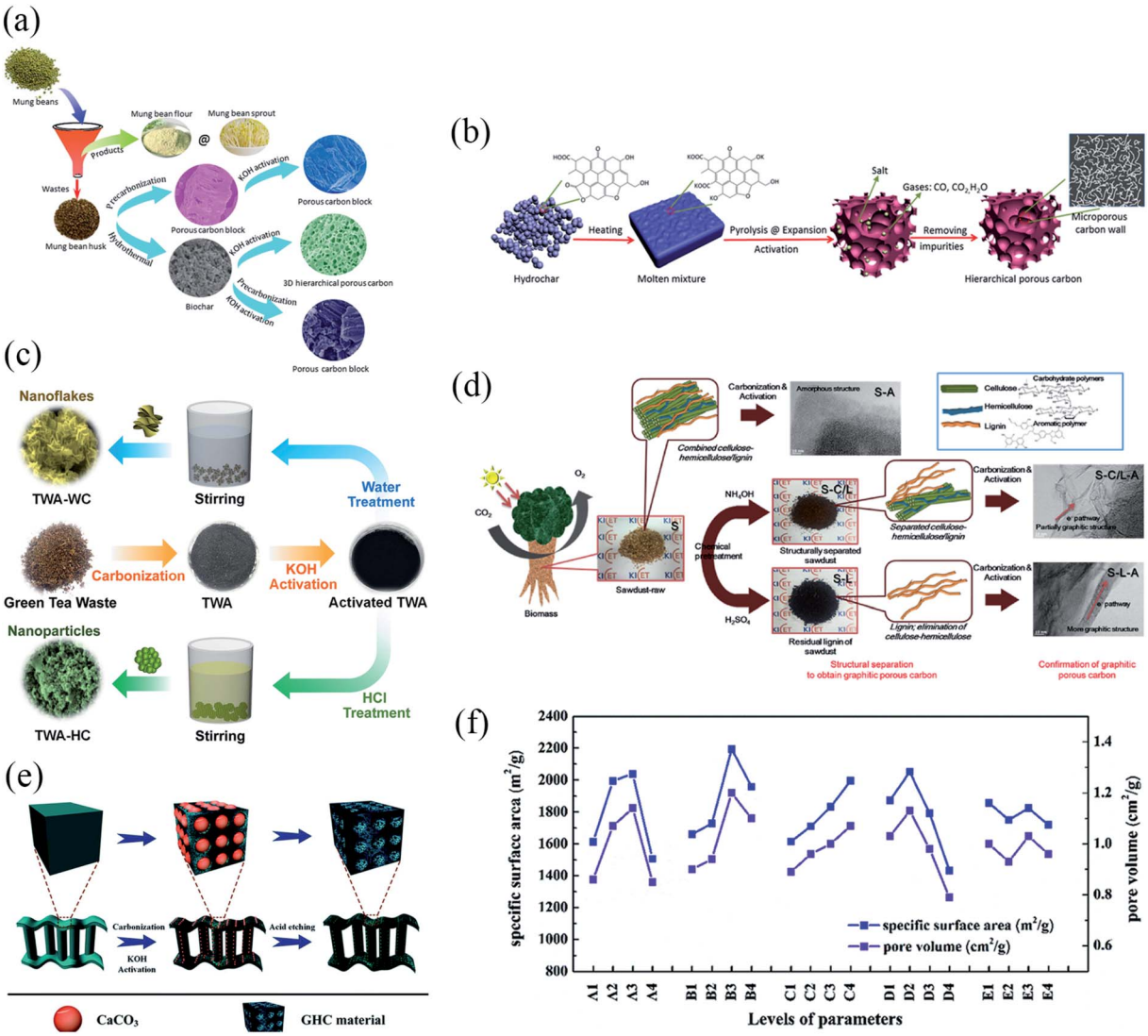

Fig. 4 (a) Schematic illustration of porous carbon prepared by three chemical activation methods based on KOH. (b) Schematic illustration of the constitution process of the three-dimensional hierarchical porous structure. Reprinted with permission from ref. 47. Copyright 2019 Elsevier B. V. (c) Schematic diagram of synthesis of carbon materials by KOH activation with different post-treatment methods. Reprinted with permission from ref. 50. Copyright 2019 Elsevier B. V. (d) Schematic of the evolution of the three samples from the sawdust of pitch pine and HR-TEM image of the samples. Reprinted with permission from ref. 49. Copyright 2017 Elsevier B. V. (e) Schematic of the process of the fabrication of the GHC material. (f) The effect of A (impregnation ratio), B (activation temperature), C (activation time), D (carbonization temperature), and E (carbonization time) on the specific surface area and pore volume of the as-prepared GHC materials. Reprinted with permission from ref. 51. Copyright 2018 the Royal Society of Chemistry.

and KOH activation showed blocky shape with abundant micropores. The oxygen-containing functional groups on porous carbon after hydrothermal carbonization played an important role in promoting the three-dimensional porous structure of 3DHPC (Fig. 4b). 3DHPC and PCB are less graphitized than PC due to their high heteroatom content. They also had a lower specific surface area and more oxygen-containing groups. It can be seen that screening for an appropriate KOH activation method for a certain type of raw material to prepare BPGCs is the basis.

The preparation of BPGCs from biomass by a chemical activation method based on KOH has been extensively studied. The influences of the type of raw material, activation temperature, activator concentration, ratio of activator to raw materials and activation pre-treatment and post-treatment methods on the structure and properties of BPGCs have been emphatically discussed. Xing *et al.*[48] reported porous graphitic carbon with different amylopectin contents obtained from three different raw materials (taro, sweet potato, and potato) through a combination of pre-carbonization and KOH activation. The products with a higher amylopectin content possessed a higher degree of graphitization and lower specific surface area. It is valuable to identify more ingredients which are similar to amylopectin from the raw materials to regulate the porous structure and graphitic structure of BPGCs. Another study converted the biomass of chemical reagent pretreatment into

partially graphitic porous carbon from pitch pine (*Pinus rigida*) *via* KOH activation by Han *et al.*[49] (Fig. 4d). Soaking biomass in NH_4OH solution resulted in the separation of its components. Significantly, the as-separated cellulose and hemicellulose promoted the development of a porous structure, and the as-separated lignin was more conducive to the formation of a graphitic structure after KOH activation.[49] Inspired by this research, adjusting the proportion of cellulose, lignin, and hemicellulose in biomass to control the structure and properties of BPGCs needs attention. Moreover, this study also confirmed that the effects of different pre-treatment methods on the structure and properties of the product may play a decisive role. The pre-treatment methods used to prepare BPGCs also include the most basic washing, drying, grinding and pulverizing at the moment. Similarly, the post-treatment methods for preparing BPGCs also have a great influence on their structure and properties. Lee's team[50] carried out two different post-treatment methods of green tea waste activated with KOH and pre-carbonized, in which interconnected mesoporous graphitic carbon nanoflakes (TWA-WC) were obtained after treatment with water and aggregated nanoparticles (TWA-HC) were obtained after treatment with hydrochloric acid (Fig. 4c). In contrast, TWA-WC has a higher graphitization degree, larger specific surface area and more developed pore structure. Surprisingly, Zhang *et al.*[51] comprehensively analyzed the effects of various preparation conditions on the properties of three-dimensional hierarchical porous graphitic carbon (GHC) derived from garlic skin treated with KOH and pre-carbonized (Fig. 4e). Specifically, by using an orthogonal method, the influence of the impregnation ratio of KOH to carbonized products (A), activation temperature (B), activation time (C), carbonization temperature (D), and carbonization time (E) on the specific surface area and pore diameter was strikingly probed. The following conclusions could be drawn from Fig. 4f: (i) With the gradual increase of the ratio of KOH to the carbonized product, the number of open holes and enlarged holes of GHC increased, and the specific surface area and pore volume increased rapidly. However, excessive KOH resulted in excessive ablation of GHC. The carbon skeleton around some micropores collapsed, making some micropores combine to form mesopores or even macropores, leading to the decrease of the specific surface area and pore volume of GHC. (ii) Increasing the activation temperature made more carbon active sites participate in the reaction with KOH, which significantly improved the specific surface and pore volume. However, there were a certain number of active carbon sites that reacted with KOH. After the optimal temperature, increasing the temperature (especially after 800 °C) caused the undue ablation and collapse of the carbon skeleton. (iii) Increasing the carbonization temperature created more initial pores and promoted the subsequent KOH activation, thus increasing the specific surface area and pore volume of GHC. Nevertheless, when the carbonization temperature was too high, the mechanical strength of the pore structure will be weakened, leading to the collapse of the carbon skeleton in the carbonization process and the subsequent activation process. (iv) The longer the activation time, the better the development of pores and the larger the specific surface area and pore volume. In general, the influence level of preparation conditions on the pore structure of GHC followed the order: carbonization temperature > activation temperature > impregnation ratio > activation time > carbonization time. These conclusions reflected in most studies on the preparation of BPGCs and had an important reference value for the controllable preparation of porous structure. However, the effect of these preparation conditions on the graphitic structure and heteroatomic doping was not described.

During the preparation of BPGCs by chemical activation based on KOH, the influence of preparation temperature on the properties and structure of BPGCs is of the greatest concern. Yuan *et al.*[52] prepared a series of carbon materials (CMCN-*X*, *X* represents the activation temperature) by KOH activation of pre-carbonized peanut residue at 600 °C, 700 °C, 800 °C, 900 °C and 1000 °C, respectively. The products at activation temperatures ranging from 600 °C to 800 °C exhibited interconnected three-dimensional hierarchical carbon nanosheets (Fig. 5a–c and f–h), while the products at activation temperatures of 900 °C to 1000 °C showed a wrinkled graphene-like nanosheet morphology (Fig. 5d–e, i and j). With the increase of activation temperature, the products had more graphitized carbon microcrystals. The Raman spectra and XRD patterns further confirmed that the degree of graphitization of the products was proportional to the activation temperature (Fig. 5k and l). Moreover, when the activation temperature increased, the heteroatom and nitrogen content of the products decreased (Fig. 5m and n). The mesoporous structure of CMCN-900 and CMCN-1000 was particularly obvious, while CMCN-600, CMCN-700, and CMCN-800 possessed a sky-high microporous ratio. From 600 °C to 800 °C, the specific surface area of the products gradually ascended and then begun to descend (Fig. 5o). Chen *et al.*[53] prepared cellular architecture porous carbon from taro epidermis by pre-carbonization integrated with KOH activation. Similarly, they discovered that the content of nitrogen and oxygen of the products at higher activation temperatures decreased and the specific surface area initially enlarged and diminished after 800 °C with the increase of activation temperature. The graphitization degree and crystallinity of the as-prepared products at higher KOH activation temperature slightly weakened, presumably because KOH activation led to more defects in carbon.[39] Another study by Song *et al.*[54] also seemed to support this point. They obtained three-dimensional hierarchical porous carbon (3DHPC) from corn husk through KOH pretreatment and subsequent pyrolysis. When the concentration of KOH solution impregnated corn husk was increased, the graphitization degree of 3DHPC was lower. The higher KOH content in the samples might cause the growing disorder and defects in the carbon structure. However, the study by Li *et al.*[55] found that the graphitization degree of the as-prepared products increased first and then decreased with the increase of activation temperature. The products were obtained from sisal through pre-carbonization and KOH activation. As for the impact of KOH activation temperature on heteroatoms in BPGCs, Ma *et al.*[56] and Chen *et al.*[57] explained that when the activation temperature rose, the proportion of total nitrogen and pyrrolic nitrogen of the as-fabricated products decreased,

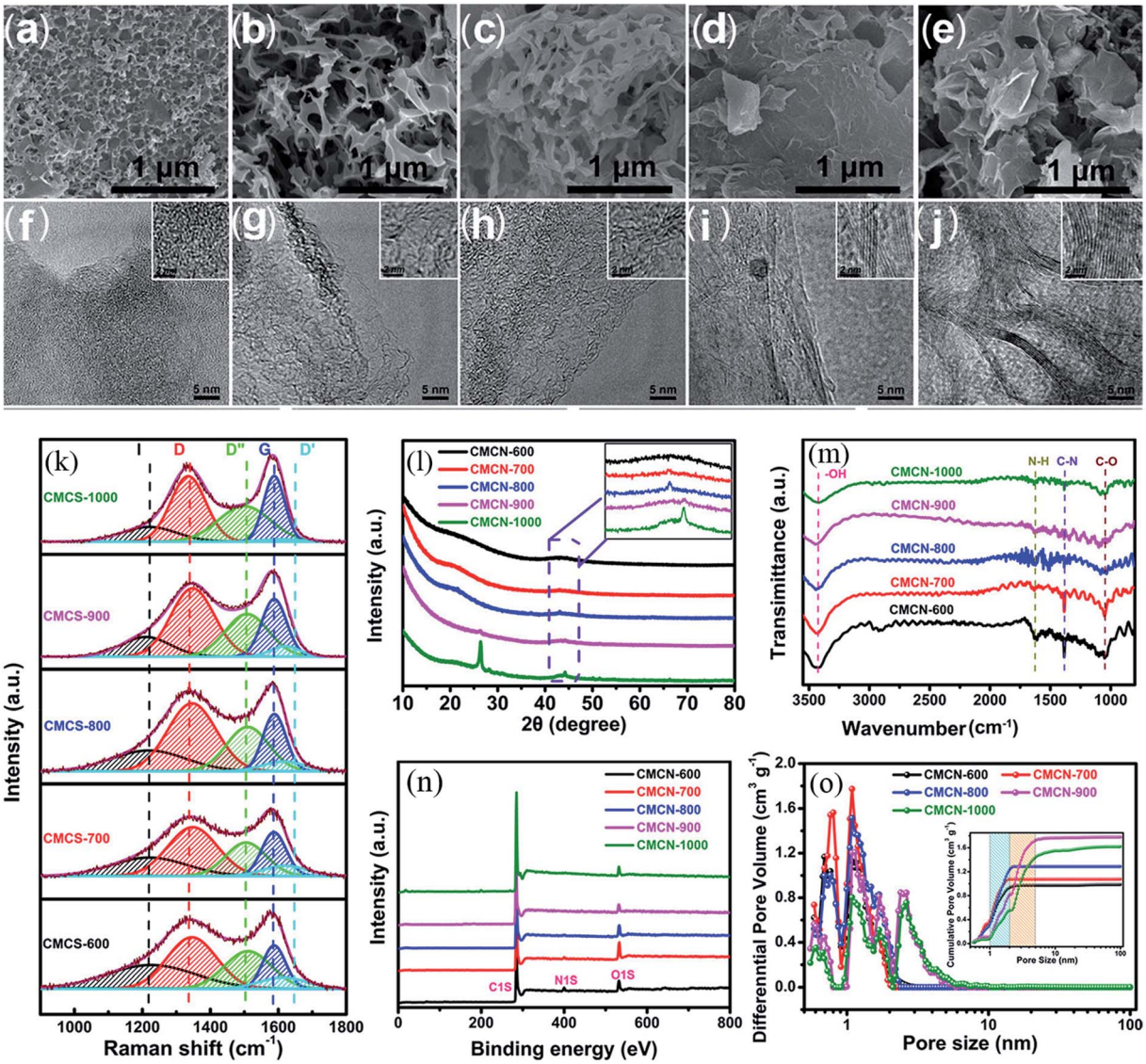

Fig. 5 FESEM images of (a) CMCN-600, (b) CMCN-700, (c) CMCN-800, (d) CMCN-900, and (e) CMCN-1000. HRTEM images of (f) CMCN-600, (g) CMCN-700, (h) CMCN-800, (i) CMCN-900, and (j) CMCN-1000. (k) Fitted Raman spectra of CMCN-*X* (*X* from 600 °C to 1000 °C). (l) XRD patterns, (m) FTIR spectra, (n) XPS spectra, and (o) Pore size distributions of CMCN-*X* (*X* from 600 °C to 1000 °C). The inset in (o) shows the cumulative pore volume. Reprinted with permission from ref. 52. Copyright 2019 American Chemical Society.

while the proportion of graphitic N increased. Ma *et al.*[56] also found that the content of oxygen in the as-fabricated products also decreased with the increase of activation temperature. The reason for the influence of temperature on heteroatoms remains to be further studied, which can vigorously promote the development and utilization of heteroatom-doped BPGCs.

In general, chemical activation methods based on KOH have been widely used to prepare BPGCs, among which the most widely used method is to combine KOH activation with pre-carbonization or hydrothermal carbonization by selecting appropriate pre-treatment and post-treatment methods. However, the current problem is that the relationship between biomass raw materials and various preparation conditions and the structure and properties of BPGCs needs to be further systematically studied and clarified. The effect of activation temperature on the porous structure and specific surface area of BPGCs has been studied thoroughly, but the influence of other factors on the graphitic structure and heteroatom doping of BPGCs needs to be studied. In particular, the synergistic effect of various parameters is rarely analyzed, which is of great significance to balance various preparation conditions to achieve controllable preparation. In addition, the mechanism and deeper reasons behind these effects need to be researched seriously. It is necessary to mention the shortcomings of the KOH activation process, such as corrosive nature and high activation temperature. How to overcome these disadvantages is the research hotspot of chemical activation in the future. Sodium amide ($NaNH_2$) is an emerging activation and nitrogen-doping agent to replace KOH, which helps to prepare BPGCs at relatively low activation temperature.[58,59] Zhang *et al.*[60]

employed solid $NaNH_2$ to synthesize N-rich carbon materials with a layered graphene-like structure and hierarchical porous structure from oil-tea seed shells (OTSSs) through direct chemical activation. Latterly, newly emerged copper bromide,[61] potassium oxalate monohydrate[62], and dicyandiamide[62] have also been reported to supersede KOH to prepare BPGCs.

2.3 Catalytic graphitization

Generally speaking, the hard carbon structure formed in the pyrolysis process of biomass is elusive to mutate into an ideal graphitic structure even when pyrolysis temperature is up to 2500 °C.[63,64] The hard carbon structure is composed of a graphite microcrystalline and amorphous zone, which does not show crystalline properties macroscopically. The porous structure of biomass can be typically developed, but the graphitic structure is ordinarily not perfect after chemical activation.[65–67] Compared with graphitic carbon (GC), biomass with chemical activation has relatively low electrical conductivity, which means that it is needful to improve its graphitic structure to enhance application performance.[49] At present, high temperature pyrolysis and catalytic graphitization are the main methods to prepare carbon materials with an excellent graphitic structure from biomass.[68] High temperature pyrolysis often takes a temperature of 2500 °C or higher temperature to achieve a well-developed graphitic structure of materials. Superhigh temperature conditions consume a lot of energy, which is not in line with the principles of "energy conservation and emission reduction" and green chemistry. Catalytic graphitization refers to the introduction of graphitization catalysts into amorphous carbon.[69,70] Graphitization catalysts cut the activation energy of transition from amorphous carbon to the graphite phase, so that graphitic carbon is obtained at a lower temperature ($\leq$1000 °C).[71,72] Low temperature graphitization retains the original structural characteristics of biomass to the maximum extent, improves the graphitic structure and optimizes the porous structure and surface properties of biomass. Catalytic graphitization is a very complicated process with both physical and chemical changes.[73,74] At present, there are two mechanisms for catalytic graphitization: (a) the dissolution and re-precipitation mechanism.[75,76] Under the action of a graphitization catalyst, the chemical bonds between the carbon atoms are broken, and then the catalyst continuously dissolves the amorphous carbon until it reaches saturation. The energy level of saturated carbon is higher, so it needs to be converted to a low-level graphite crystal state, thereby obtaining a graphitic carbon material. (b) The carbide transformation and decomposition mechanism:[77,78] the graphitization catalyst first combines with the carbon material to form a carbide and then decomposes to form graphitic carbon.[79,80] It should be pointed out that the above two mechanisms are relatively clear about the catalytic graphitization. The mechanism of catalytic graphitization of biomass is very complex, and there are still many to be explored. Until now, the most commonly used graphitization catalysts are transition metal elements (such as Fe, Co, and Ni) and their oxides (such as Cr_2O_3 and MnO_2).[70,79] These graphitization catalysts sometimes act not only as catalysts but also as hard templates to accelerate the pore formation.

The structure and properties of BPGCs formed by catalytic graphitization are influenced by the biomass precursor, the categories and concentrations of the graphitization catalyst, the post-treatment methods, and so on.[81–83] Sevilla *et al.*[74] acquired graphitic carbon (GC) by pyrolyzing sawdust impregnated with iron nitrate or nickel nitrate at 900 °C and 1000 °C. In order to get pure graphitic carbon to the greatest extent, it is particularly important to carry out effective post-treatment. The as-acquired samples after pyrolysis and acid pickling contained amorphous carbon and graphitic carbon (Fig. 6a and b). Sevilla *et al.*[74] made use of an oxidant (potassium permanganate) to remove amorphous carbon from the as-acquired samples to obtain high purity graphitic carbon (GC) (Fig. 6c). It was found that iron had better catalytic graphitization performance than nickel. When the pyrolysis temperature increased, the graphitization degree of GC increased and the specific surface area decreased. Liu *et al.*[84] employed iron nitrate as a graphitization catalyst to pyrolyze coconut shells in the range of 500–100 °C to prepare graphitic carbon with a three-dimensional interconnected and hierarchical porous structure. They also found that the graphitization degree of the products increased with the increase of temperature. Interestingly, Thompson *et al.*[69] revealed that the graphitization degree and graphitic structure of porous graphitic carbon prepared from cork sawdust had almost no fluctuation by reducing the concentration of the graphitization catalyst iron (Fig. 6d), while its specific surface area gradually increased and the pore structure changed (Fig. 6e). They also hypothesized that the resulting liquid iron carbide (Fe_3C) nanoparticles, which acted as the graphitization catalyst, dissolved amorphous carbon when they etched and flowed through the carbon matrix. The Fe_3C nanoparticles catalyzed the formation of graphitic nanotubes later, which was related to the mechanism of dissolution and reprecipitation. Gutiérrez-Pardo *et al.*[85] obtained porous graphitic carbon by using iron to catalyze beech. It was also speculated that the catalytic graphitization mechanism is similar to that of Thompson *et al.*'s[69] study (Fig. 6f). In addition, Wu *et al.*[86] introduced iron (III) acetylacetonate into degreasing cotton and obtained graphitic carbon through subsequent pyrolysis. Catalytic iron nanoparticles also catalyzed the formation of graphitic shell layers by the dissolution and re-precipitation mechanism.

It can be seen that the research on the preparation of BPGCs from biomass by catalytic graphitization is not sufficient, which also hinders the analysis and generalization of the effects of this method parameters on the structure and properties of the products. Highly graphitic carbon materials can be obtained from biomass by catalytic graphitization, but it is difficult to obtain carbon materials with an excellent porous structure. It has great potential to improve the catalytic graphitization method to prepare BPGCs with an excellent graphitic structure and porous structure. Wang *et al.*[87] obtained graphitic carbon nanostructures from Fe/conducting polymer/biomass composites by microwave-assisted pyrolysis. After the microwave-assisted pyrolysis, the unique and complex morphologies and

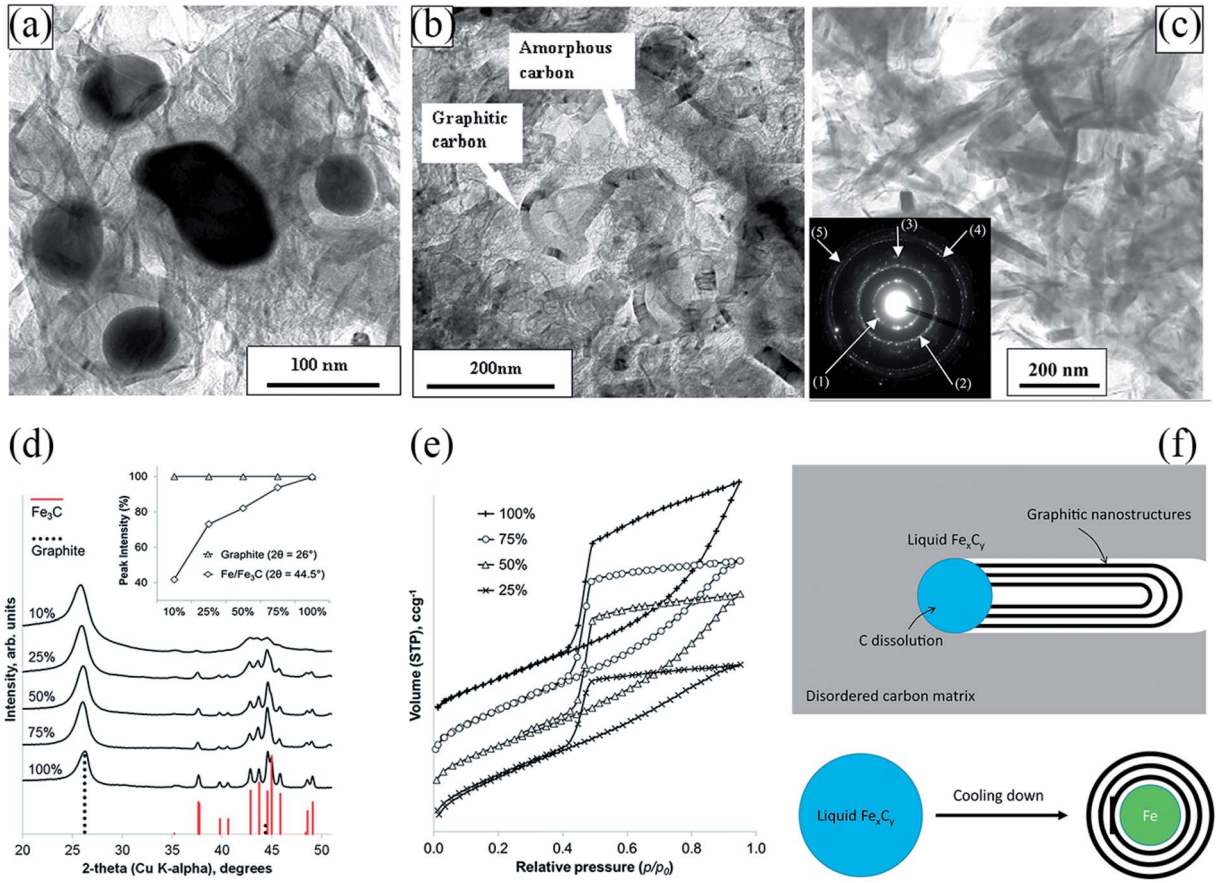

Fig. 6 TEM images of (a) the iron-carbon nanocomposite (iron nanoparticles are the dark areas) and (b) the carbonized sample after the removal of iron nanoparticles. (c) The graphitic carbon obtained after the removal of amorphous carbon (inset, SAED pattern of this sample). Reprinted with permission from ref. 74. Copyright 2007 American Chemical Society. (d) PXRD patterns and (e) N_2 sorption isotherms (vertically offset) for sawdust carbonized with a range of iron concentrations (values in mol%); inset shows the plot of the relative intensities of main Fe/Fe_3C and graphite peaks with changing iron : biomass ratio. Reprinted with permission from ref. 69. Copyright 2015 the Royal Society of Chemistry. (f) Schematic of the catalytic mechanism responsible for the formation of partially graphitized carbon (formation of Fe_xC_y droplets and growth of graphitic structures by solution-precipitation and decomposition of Fe_xC_y into Fe nanoparticles surrounded by a graphitic shell). Reprinted with permission from ref. 85. Copyright 2015 Elsevier B. V.

microstructures of biomass were reserved, and highly porous graphitic materials were obtained at the same time. Indeed, it would be foremost to develop graphitization catalysts that have the ability to develop good porous structures for biomass.

2.4 Catalytic graphitization combined with chemical activation

2.4.1 Using two different catalysts. Generally speaking, the methods for preparing porous carbon materials from biomass are chiefly based on chemical activation. However, the graphitic structure of BPGCs obtained by chemical activation is not desirable, which sometimes needs to be further graphitized in practical applications.[88] Catalytic graphitization by means of transition metals is an effective way to get carbon materials with a good graphitic structure. From the previous discussion, it can be known that the promotion of the graphitization degree caused by the graphitization catalyst is able to balance the reduction of the graphitization degree caused by activation agents such as KOH. Accordingly, the combination of chemical activation and catalytic graphitization is a promising pattern of preparing BPGCs. Two different catalysts are used for chemical activation and catalytic graphitization, respectively. Among them, the catalysts for catalytic graphitization are primarily metal salts containing Fe, Co, and Ni, and the reagents for chemical activation are mostly KOH, $ZnCl_2$, and K_2CO_3. The porous and graphitic structure or heteroatom doping of BPGCs primarily depends on the characteristics of biomass raw materials, methods of pretreatment and operating parameters (especially temperature).[26]

Chang *et al.*[89] prepared carbon materials treated with different activators (KOH, NaOH, $ZnCl_2$, and H_3PO_4) using Chinese parasol fluff as the precursor and cobalt nitrate (Co$(NO_3)_2$) as the graphitization catalyst (Fig. 7a). The results showed that the carbon materials prepared under the activation treatment of KOH had a unique hierarchical interconnected porous skeleton (Fig. 7b–i), the highest graphitization degree and an optimal pore size distribution. Yang *et al.*[90] used Co$(NO_3)_2$ and KOH as the graphitization catalyst and activation

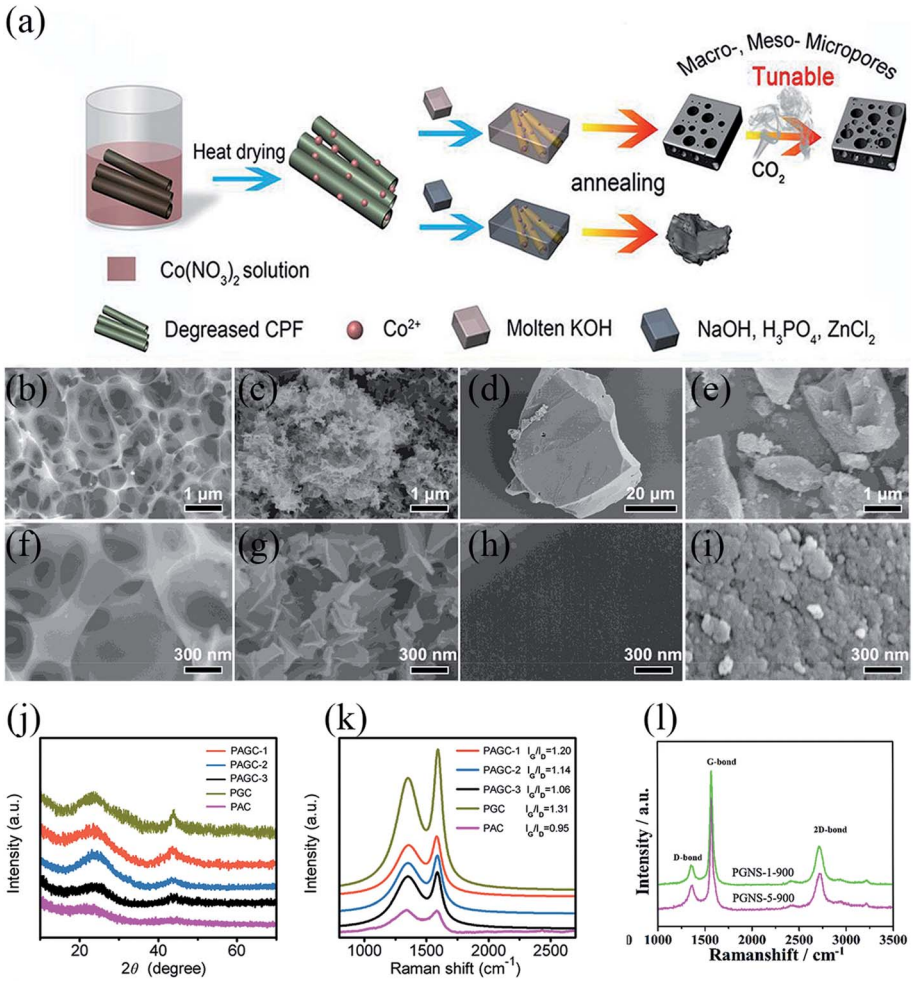

Fig. 7 (a) Schematic of the evolution of the as-prepared carbon materials treated with different chemical activators. (b) and (f) SEM images of the as-prepared carbon materials treated with KOH. (c) and (g) SEM images of the as-prepared carbon materials treated with NaOH. (d) and (h) SEM images of the as-prepared carbon materials treated with $ZnCl_2$. (e) and (i) SEM images of the as-prepared carbon materials treated with H_3PO_4. Reprinted with permission from ref. 89. Copyright 2019 American Chemical Society. (j) XRD patterns of PAGC-*X* (*X* represents the mass ratio between KOH and biomass raw material). (k) Raman spectrum of PAGC-*X*. Reprinted with permission from ref. 90. Copyright 2019 Elsevier B. V. (l) Raman spectra of PGNS-1-900 and PGNS-5-900 samples. Reprinted with permission from ref. 91. Copyright 2013 the Royal Society of Chemistry.

agent respectively to manufacture hierarchical porous carbon (PAGC) with a high graphitization degree and heteroatom content from bio-waste shaddock endothelium by one-pot pyrolysis. The results displayed that when the mass ratio of KOH to biomass feedstock increased, the graphitization degree of the products weakened (Fig. 7j and k), and the specific surface area of the products first increased and then decreased. These results also verified our previous conclusions. Introducing Co $(NO_3)_2$ into bio-waste shaddock endothelium in the preparation of the products relieved the negative impact on the decreased graphitization degree caused by KOH treatment.[90] Instead of Co $(NO_3)_2$ and KOH, $FeCl_3$ was combined with $ZnCl_2$ to simultaneously graphitize and activate coconut shells to fabricate porous graphene-like nanosheets (PGNSs) with a high specific surface area for supercapacitor electrodes by Sun *et al.*[91] It could be seen that changing the amount of activator $ZnCl_2$ had no obvious effect on the graphitization degree of the PGNSs (Fig. 7l). In the beginning, the specific surface area of the PGNSs increased with the increase of the activator amount, but the excessive activator was not conducive to the formation of the porous structure, resulting in a lower specific surface area. The graphitization degree of the PGNSs increased with the increase of carbonization temperature. The high temperature was conducive to the transformation of carbon materials from amorphous carbon into crystalline carbon, but too high temperature led to the collapse of the carbon skeleton and decrease the specific surface area. A study by Wan *et al.*[92] found a similar effect of temperature change on the degree of graphitization and specific surface area. They obtained nitrogen and sulfur co-doped hierarchical porous graphitic carbon from rape pollen through catalytic graphitization and activation with $FeCl_3$ and $ZnCl_2$. They also found that with the increase of pyrolysis temperature during the preparation of materials, the content of heteroatoms decreased, and the content of different

nitrogen configurations had no obvious law of change. However, Jin *et al.*[93] got three-dimensional interconnected porous graphitic carbon from rice straw through graphitization and activation with nickel nitrate and KOH. When the KOH activation temperature was increased, the graphitization degree of the products first increased and then decreased. It should be noted that this study did not directly pyrolyze the mixture of the graphitization catalyst, activator and biomass raw materials. Cai *et al.*[94] prepared hierarchical porous graphitic carbon from *Moringa oleifera stem* using $FeCl_3$ and $ZnCl_2$ as the graphitization catalyst and chemical activator, respectively. The increase of graphitization catalyst ($FeCl_3$) concentration promoted the enhancement of the graphitization degree and the increase of the specific surface area. For the preparation of BPGCs using a graphitization catalyst and chemical activator, more attention has been paid to the influence of temperature and activator dosage on the porous structure and graphitic structure of BPGCs. However, there is no complete theory to adjust the influence of these parameters on the structure and properties of BPGCs. What is clear is that both the temperature and the dosage of the activator may have a value that gives the best effect. In practical applications, how to regulate these parameters and make BPGCs with the best performance is our goal. In the future, more attention should be paid to the effect of the graphitization catalyst on the structure and properties of the products, as well as the effect of these parameters on the regulation of heteroatoms.

2.4.2 Using one catalyst. It is found that BPGCs can be synthesized by using two different catalysts, in which the activation catalysts are used to stimulate and develop the porous structure and the graphitization catalysts catalyze the formation of the graphitic structure. Unfortunately, the majority of the above activators and catalysts are highly corrosive or toxic substances, which will cause corrosion of the production equipment and environmental pollution. Using two different catalysts is time-consuming and complex for operation. Therefore, compared with two different catalysts, using only one catalyst to realize simultaneous activation and graphitization of biomass is less time-consuming, more efficient and less pollution. Gong *et al.*[95] proposed a "one catalyst" method to fulfil the synchronous activation and graphitization of bamboo for preparing highly porous graphitic carbon by using potassium ferrate (K_2FeO_4) as the catalyst. According to reaction (8), potassium ferrate was thermally decomposed to form KOH and Fe $(OH)_3$, wherein KOH was responsible for the activation process and Fe $(OH)_3$ was related to the graphitization process.[39,96,97]

$$4K_2FeO_4 + 10H_2O \rightarrow 8KOH + 4Fe(OH)_3 + 3O_2 \quad (8)$$

Xia *et al.*[98] developed a low temperature graphitization method to achieve efficient preparation of coconut shell biochar from a hard carbon structure to three-dimensional porous graphene-like sheets (3DPGLS) at 900 °C by utilizing carbonate as the molten salt medium and catalyst (Fig. 8a). The formation process of the graphene-like structure of coconut shell biochar is shown in Fig. 8b and c. Firstly, the sp^3 cross-linking carbon atoms in hard carbon were chemically cut by potassium carbonate (K_2CO_3). The detached graphite crystallites could move freely in the molten salt. When the reaction temperature gradually rose to 600 °C, K_2CO_3 started to react with carbon, according to reaction (9).[99,100] Then, under the catalysis of alkali metal atoms (K), the graphene microcrystals have merged and grown to form a graphene lamellar structure. At the same time, the pore-forming effect of alkali metal carbonate (K_2CO_3) made the material have a porous structure, and three-dimensional porous graphene-like sheets with a high specific surface area were obtained.[98]

$$K_2CO_3 + 2C \rightarrow 2K + 3CO\uparrow \quad (9)$$

Although catalytic graphitization combined with chemical activation is an effective way for producing BPGCs, simpler processes are still needed to prepare BPGCs.[36] Consequently, it is a key requirement and major challenge to develop a more effective and simple method for preparing BPGCs from existing natural renewable biomass. For the preparation strategy, it should not only match with biomass sources with different characteristics, but also have extensibility. It is urgent to explore more green and efficient activators and optimize the existing catalytic and activation process.

2.5 For precise and controlled preparation

As we all know, biomass has the characteristics of rich sources, diverse structures and properties. In recent years, how to prepare BPGCs accurately and controllably from a wide range of biomass resources has attracted much attention. At present, there seems to be no systematic theory and method to guide the accurate and controlled preparation of BPGCs. To this end, we put forward the following possible solutions and suggestions including the smart selection of suitable biomass raw materials, development of common and effective synthesis strategies, and establishment of a biomass feedstock–synthesis parameter–structure and property evolution model.

(i) The smart selection of suitable biomass raw materials. In view of the main structure and properties of BPGCs (*i.e.*, porous structure, graphitic structure, specific surface area and heteroatom doping), it is necessary to prepare BPGCs by using the characteristics of specific biomass with a natural structure and composition. There are many research studies on BPGCs from certain biomass. In order to expand the production, it is important to systematically summarize the commonness of biomass sources. Niu *et al.*[101] summarized that collagen-based porous carbon (CPC) prepared from collagen-enriched biomass has rich heteroatom doping, developed porosity and a unique morphology. Bi *et al.*[10] reviewed the preparation of porous carbon materials with a one-dimensional or two-dimensional or three-dimensional structure by using the natural biological structure of biomass. Zhou *et al.*[6] summarized the preparation of carbon materials with a three-dimensional porous structure from biomass. These studies provide a good reference for us to choose biomass raw materials. However, the preparation of carbon materials with

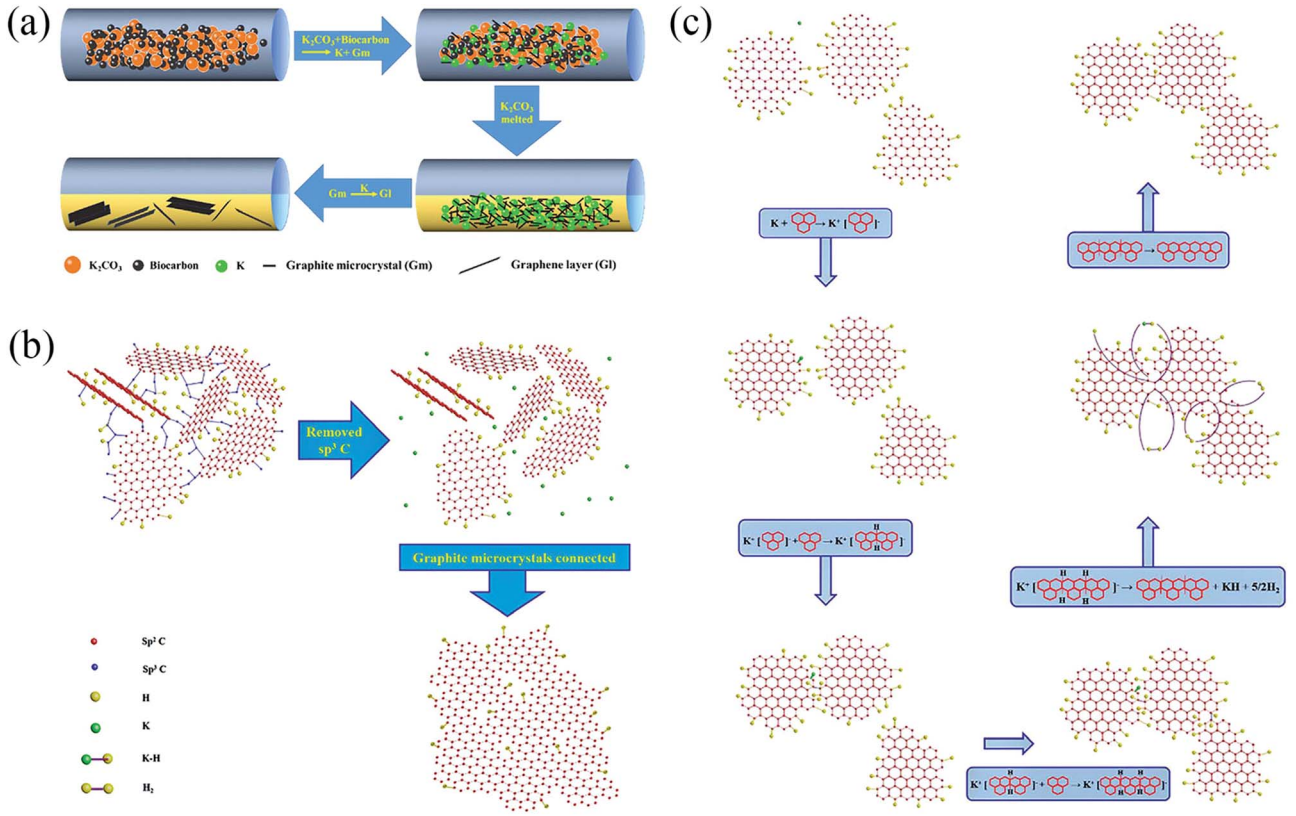

Fig. 8 (a) Synthetic procedure of 3DPGLS. (b) Simulation of the biochar graphitization process: transition from hard carbon to graphene-like sheets. (c) Detailed processes of catalysis graphitization. Reprinted with permission from ref. 98. Copyright 2018 the Royal Society of Chemistry.

a graphitic structure from biomass has not been systematically summarized. Choosing a suitable precursor of biomass is to make full use of the characteristics of biomass and maximize its utilization value, so as to lay the foundation for the subsequent preparation.

(ii) Development of common and effective synthesis strategies. The controlled preparation of BPGCs from a single biomass type has been extensively explored, and how to replicate the synthesis of BPGCs from a variety of biomass sources is worthy of attention. Li *et al.*[102] took $Mg_5(OH)_2(CO_3)_4/ZnCl_2$ as a double template through high-temperature carbonization and activation to explore a universal synthesis method for the synthesis of hierarchical porous heteroatom-doped carbon materials from a variety of biomass sources. In addition, Xia *et al.*[98] also prepared porous graphitic carbon materials from several biomass materials by high-temperature activation of K_2CO_3.

(iii) Establishment of a biomass feedstock–synthesis parameter–structure and property evolution model. At present, it is necessary to analyze and summarize the influence of the biomass types, preparation methods and parameters on the structure and properties of BPGCs. The mechanism of action of each parameter needs to be described and analyzed at the micro-level. At the same time, the interaction mechanism of the different parameters is worthy of deep exploration, and the biomass feedstock-synthesis parameter–structure and property evolution model is sought to establish. So that the structure and properties of BPGCs can be systematically regulated and predicted, and the accurate and controllable large-scale preparation can be realized.

3 BPGCs for energy applications

3.1 Supercapacitors

In recent years, supercapacitors (SCs) have received great attention as a type of leading electrochemical energy storage device and are regarded as the most promising green energy technology in this century.[103] Compared with conventional capacitors and secondary batteries, the main advantages of SCs are as follows: fast charge–discharge process, high power density, high specific capacity, long-term cycle stability, wide operating temperature range and energy conservation.[104–107] According to their different energy storage mechanisms, supercapacitors can be divided into three types: electrical double layer capacitors (EDLCs) based on non-faradaic mode, pseudocapacitors based on faradaic mode and hybrid capacitors based on the above two principles of energy storage.[108] Among them, EDLCs are the most widely studied and have been commercialized at the same time. EDLCs have been applied in many fields, including power, transportation, national defense, military industry, new energy vehicles, electronics and mobile communications, and the related research is a hot topic at the

Table 2 Representation of the performance of BPGCs from various biomass precursors as electrodes for SCs

Biomass	Electrolyte	Specific capacitance/current density	Energy density/power density	Rate capability (%)	Cycles	CR[a] [%]	Ref.
Reed membrane	6 M KOH	353.6 F g^{-1} at 0.5 A g^{-1}	11.6 W h kg^{-1} at 210 W kg^{-1}	76.9% at 10 A g^{-1}	10 000	96.1	263
Willow catkin	6 M KOH	340 F g^{-1}, 52.7 mF cm^{-2} at 0.1 A g^{-1}	—	231 F g^{-1} at 10 A g^{-1}	3000	92	138
Pomelo peel	1 M TEA BF_4-PC	163 F g^{-1} at 0.5 A g^{-1}, 116 F g^{-1} at 10 A g^{-1}	50.95 W h kg^{-1} at 0.44 kW kg^{-1}, 25.3 W h kg^{-1} at 21.5 kW kg^{-1}	—	10 000	91	253
Shell of broad beans	6 M KOH	202 F g^{-1} at 0.5 A g^{-1}, 129 F g^{-1} at 10 A g^{-1}	—	—	3000	90	254
Garlic skin	6 M KOH	427 F g^{-1} (162 F cm^{-3}) at 0.5 A g^{-1}, 315 F g^{-1} (120 F cm^{-3}) at 50 A g^{-1}	14.65 W h kg^{-1} at 310.67 W kg^{-1}, 11.18 W h kg^{-1} at 27.3 kW kg^{-1}	74% at 50 A g^{-1}	5000	94	51
Bamboo	1 M H_2SO_4	318 F g^{-1} at 0.2 A g^{-1}	42.1 W h kg^{-1} at 95 W kg^{-1}	—	2000	82	255
Dry elm samara	6 M KOH	470 F g^{-1} at 1 A g^{-1}, 310 F g^{-1} at 1 A g^{-1}	—	72% at 200 mV s^{-1}, 64% at 20 A g^{-1}	50 000	98	256
Taro	6 M KOH	397 F g^{-1} at 0.5 A g^{-1}, 276 F g^{-1} at 50 A g^{-1}	22.59 W h kg^{-1} at 148 W kg^{-1}	69.5% at 50 A g^{-1}	20 000	97	48
Firmiana simplex fluff	2 M H_2SO_4, 2 M Li_2SO_4	836 F g^{-1} at 0.2 A g^{-1}	36.50 W h kg^{-1} at 140 W kg^{-1}		10 000	92.96	140
Sugarcane bagasse	6 M KOH	339 F g^{-1} at 0.25 A g^{-1}, 280 F g^{-1} at 100 A g^{-1}	11.77 W h kg^{-1} at 34.11 W kg^{-1}	82.6% at 100 A g^{-1}	10 000	97.9	257
Spruce bark	6.0 M KOH	398 F g^{-1} at 0.5 A g^{-1}	—	69.1% at 50 A g^{-1}	10 000	96.3	130
Eucommia ulmoides oliver	1 M H_2SO_4	158 Fg^{-1} at 0.2 Ag^{-1}	—	—	5000	93	264
Mung bean husk	6 M KOH	353 F g^{-1} at 1 A g^{-1}	6.2 W h kg^{-1} at 4376 W kg^{-1}	76.48% at 50 A g^{-1}	5000	85.59	47
Oil-tea seed shell	6 M KOH	350.2 F g^{-1} at 0.5 A g^{-1}	6.0 W h kg^{-1} at 47.6 W kg^{-1}	74.2% at 10 A g^{-1}	8000	98	60
Cork	6 M KOH, 1 M Na_2SO_4	290 F g^{-1} at 0.2 A g^{-1}	14.7 W h kg^{-1} at 395 W kg^{-1}	72.4% at 70 A g^{-1}	10 000	95.2	139
Eulaliopsis binata	6 M KOH	373 F g^{-1} at 0.5 A g^{-1}		81.2% at 0.5 A g^{-1}	10 000	94.6	259
Kraft pulp	6 M KOH [BMIM][BF_4]/AN	353 F g^{-1} at 1 A g^{-1}	120.1 W h kg^{-1} at 375 W kg^{-1}, 80.4 W h L^{-1} at 250 W L^{-1}	—	—	—	265
Corn husk	6 M KOH 1 M Na_2SO_4	356 F g^{-1} at 1 A g^{-1}, 300 F g^{-1} at 20 A g^{-1}	21 W h kg^{-1} at 875 W kg^{-1}, 11 W h kg^{-1} at 5600 W kg^{-1}	88% at 10 A g^{-1}	2500	95	54
Tea leaves	6 M KOH, 1 M Na_2SO_4	167 F g^{-1} at 1 A g^{-1}	47.86 W h kg^{-1} at 1580.72 W kg^{-1}	81.42% at 30 A g^{-1}	16 000	96.66	266
Waste shaddock endothelium	1 M H_2SO_4, 1 M $BMIMBF_4$/AN	550 F g^{-1} at 0.2 A g^{-1}	46.88 W h kg^{-1} at 300 W kg^{-1}	—	10 000	93.7	90
Green tea waste	1 M H_2SO_4	162 F g^{-1} at 0.5 A g^{-1}	—	—	5000	121	50
Garlic skin	6 M KOH	427 F g^{-1} at 0.5 A g^{-1}	14.65 W h kg^{-1} at 310.67 W kg^{-1}	74% at 50 A g^{-1}	5000	94	51
Natural silk	$EMIMBF_4$	242 F g^{-1} at 0.1 A g^{-1}	90.0 W h kg^{-1} at 875 W kg^{-1}	64% at 10 A g^{-1}	10 000	92	172
Coconut shell	6 M KOH, 1 M Et_4NBF_4-PC	268 F g^{-1} at 1 A g^{-1}, 196 F g^{-1} at 1 A g^{-1}	54.7 W h kg^{-1} at 10 kW kg^{-1}	184 F g^{-1} at 30 A g^{-1}	5000	99.5	91
Bamboo	6 M KOH KOH/polyvinyl alcohol (PVA) gel, EMIM TFSI	222.0 F g^{-1} at 0.5 A g^{-1}	6.68 W h kg^{-1} at 100.2 W kg^{-1} 20.6 W h kg^{-1} at 12 kW kg^{-1}	49.9% at 20 A g^{-1}	5000	95	95

Table 2 (*Contd.*)

Biomass	Electrolyte	Specific capacitance/current density	Energy density/power density	Rate capability (%)	Cycles	CR[a] [%]	Ref.
Willow catkin	0.05 M Mn $(CH_3COO)_2$, 0.1 M Na_2SO_4	550.8 F g^{-1} at 2 A g^{-1}	—	61.8% at 50 A g^{-1}	5000	89.6	260
Disposable chopstick	6 M KOH, 1 M Na_2SO_4	234.1 F g^{-1} at 0.2 A g^{-1}	6.4 W h kg^{-1} at 98 W kg^{-1}	—	10 000	96.6	261
Shaddock skin	Mixture of EMI TFSI and EMI BF_4	152 F g^{-1} at 1 A g^{-1}	56 W h kg^{-1} at 93 kW kg^{-1}	87% at 100 A g^{-1}	10 000	97.6	262
Coconut shell	1 M $TEMABF_4$/ propylene carbonate (PC)	91.15 F g^{-1} at 0.2 A g^{-1}	23.07 W h kg^{-1} at 135 W kg^{-1}	89.23% at 2 A g^{-1}	5000	85.1	98
Moringa oleifera stem	1.0 M Na_2SO_4, 1.0 M H_2SO_4, 6.0 M KOH	283 F g^{-1} at 0.5 A g^{-1}	25.8 W h kg^{-1} at 89 W kg^{-1}	72% at 50 A g^{-1}	20 000	95	94
Rape pollen	1.0 M Na_2SO_4, 6 M KOH	361.6 F g^{-1} at 1 A g^{-1}	32.2 W h k g^{-1} at 0.089 kW kg^{-1}, 10.7 W h k g^{-1} at 4.1 kW kg^{-1}	60% at 100 A g^{-1}	20 000	94.5	92

[a] CR = capacitance retention.

moment.[1,109–111] The energy storage of EDLCs is based on the reversible adsorption and desorption of ions in the electrical double-layer at the electrode/electrolyte interface.[112–114] The basic components of supercapacitors are electrodes, electrolytes and diaphragms. Among these components, electrode materials determine the main performance parameters of supercapacitors, accounting for more than 30% of the total cost of supercapacitors.[115,116] Because electrode materials are the core of realizing the industrialization of supercapacitors, the current research on supercapacitors mainly focuses on electrode materials.[117,118] Although supercapacitors have shown excellent performance and great potential in all aspects, there are still problems to be solved, including low energy density, high cost, high self-discharge rate and poor rate performance.[108] High cost and low energy density are the biggest obstacles for the application of supercapacitors.[119] To overcome these difficulties, the most effective solution is to develop an electrode material with low cost and excellent performance. So far, carbon materials are the most mature electrode materials for supercapacitors.[120,121] An ideal choice for electrode material of supercapacitors should meet the following conditions:[107,122] (a) the electrode material should have a reasonable porous structure to ensure that it has a higher electrochemical activity specific surface area to obtain better capacity performance and improve the rate performance. (b) A good graphitic structure gives the electrode material excellent electrical conductivity, which provides a low resistance path for electrons. (c) Introducing heteroatoms into a electrode material can not only make the carbon material itself have a high pseudocapacitance, but also maintain a high cycling stability. (d) The raw materials of electrode material are widely available and the price is low. Therefore, BPGCs are suitable electrode materials for EDLCs due to their good porous and graphitic structure and heteroatom doping (Table 2).

It is found that micropores (<2 nm) with ion accessibility can provide large capacitance, while larger pores (mesopores: 2–50 nm; macropores: >50 nm) can offer channels for ion transport, reduce diffusion resistance and improve the speed performance of supercapacitors.[122–124] Therefore, it is very important to develop hierarchical porous carbon with interconnected pores of different scales. The porous structure is essential for the application of BPGCs in EDLCs. At present, the hierarchical porous structure in which micropores, mesopores and macropores coexist and the porous structure with three-dimensional (3D) interconnected framework can provide good application conditions for the design of high-performance supercapacitor electrodes.[125–129] Sun *et al.*[130] developed 3D vertically aligned graphene nanosheet arrays (VAGNAs) from spruce bark by combining hydrothermal carbonization and KOH activation methods (Fig. 9a). The as-synthesized VAGNAs not only maintained the excellent properties of graphene nanosheets, such as high conductivity and high degree of graphitization, but also derived an interconnected three-dimensional hierarchical framework and large specific surface area (Fig. 9b–e).[130] For supercapacitor applications (Fig. 9f–k), the obtained 3D VAGNAs exhibited a high specific capacitance of 398 F g^{-1} at a current density of 0.5 A g^{-1} and long-term cycling stability with 96.3% capacitance retention after 10 000

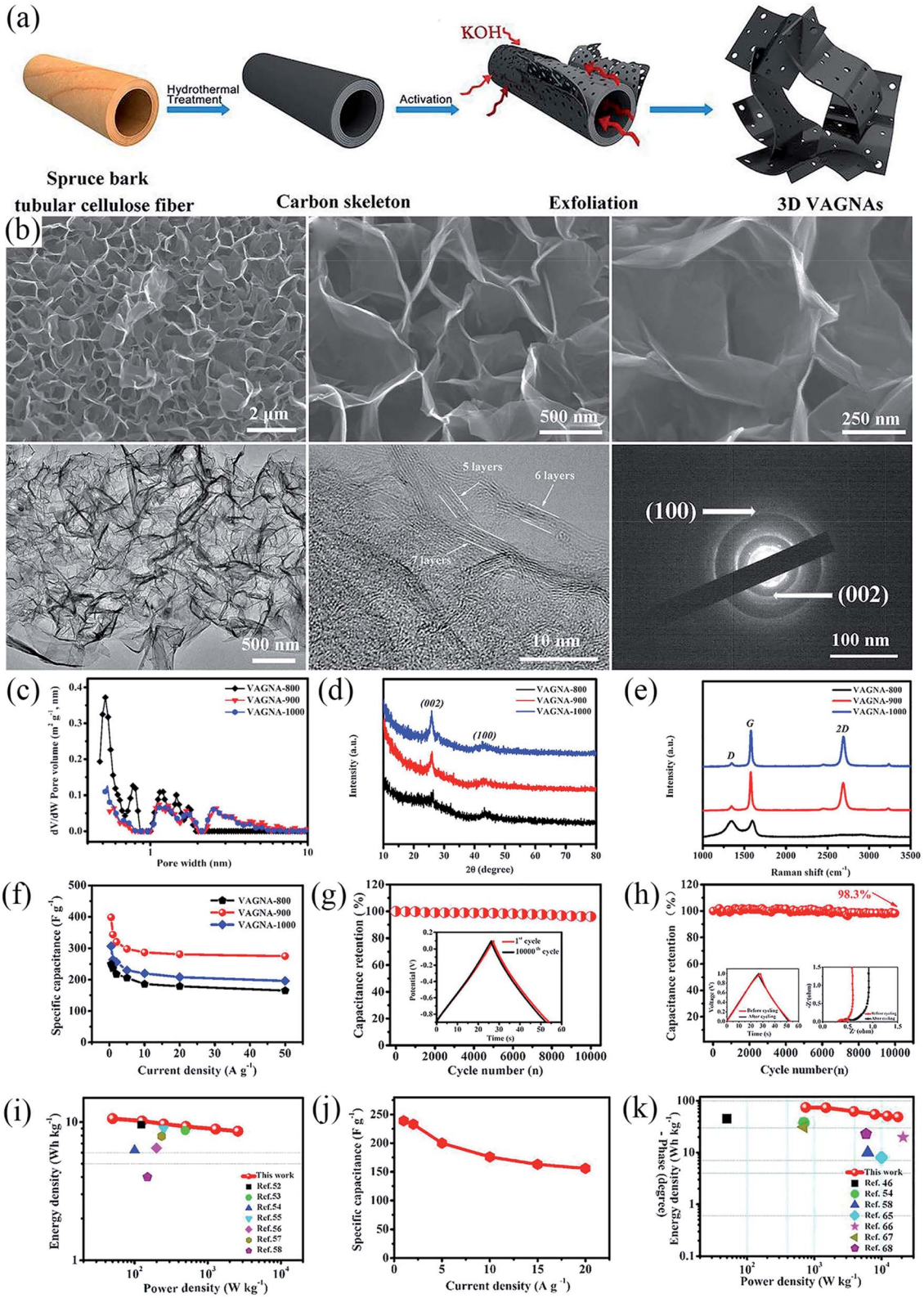

Fig. 9 (a) Schematic of the synthesis process of 3D VAGNAs. (b) SEM, high-magnification SEM, TEM, HR-TEM and SAED image of VAGNA-900. (c) Pore size distribution curves. (d) XRD patterns. (e) Raman spectra. (f) The gravimetric capacitance of VAGNAs. (g) Cycling performance of VAGNA-900 with the inset showing GCD curves. (h) Capacitance retention of VAGNA-900 with the inset showing GCD curves and EIS spectra. (i) Ragone plot of the as-assembled symmetric supercapacitors. (j) Rate performance of VAGNA-900. (k) Ragone plot of symmetrical VAGNA-900 based supercapacitors. Reprinted with permission from ref. 130. Copyright 2018 Elsevier B. V.

cycles. Moreover, a symmetric supercapacitor based on VAGNA-900 presented a high specific capacitance of 239 F g^{-1} at 1 A g^{-1} and a high energy density of 74.4 W h kg^{-1} at a power density of 743.7 W kg^{-1}. 3D VAGNAs could overcome the restacking of graphene sheets and supply intimate structural interconnectivities, a large accessible surface area for electron/ion transport, and better conductive contacts to lower the resistance of nanosheets. Gong *et al.*[95] put forward a "one catalyst" synthesis to convert bamboo into three-dimensional porous graphitic biomass carbon (PGBC). The PGBC was tested as the electrode material of supercapacitors, and the results showed that: (a) in a three-electrode system, the electrode provided a specific capacitance of 222.0 F g^{-1} at 0.5 A g^{-1} and offered superb rate performance and low impedance. (b) The solid-state symmetric supercapacitor assembled with this electrode had good energy-power output performance and showed an energy density of 6.68 W h kg^{-1} at a power density of 100.2 W kg^{-1}. (c) The coin-type symmetric supercapacitor assembled with this electrode could reach a higher energy density of 20.6 W h kg^{-1} at a power density of 12 kW kg^{-1}. Recently, Han's team[51] successfully synthesized three-dimensional hierarchical porous graphitic carbon materials (GHCs) from garlic skin by carbonization and activation, which exhibited excellent electrochemical performance and cycling stability when they were used as electrode materials for supercapacitors. It was found that micropores, especially those in the range of 0.4 to 1.0 nm, contributed the most to the capacitance. The three-dimensional hierarchical porous structure of GHCs ensured the efficient operation of ion accumulation (micropores), transport and diffusion (mesopores), and adsorption and storage (macropores), thus shortening the ion diffusion distance and reducing the diffusion resistance, which was conducive to ion transport (Fig. 10a). The high conductivity of GHCs reduced the resistance of the device, and oxygen functional groups ensured good wettability and increased the contact surface area of the ions. In addition, Zheng's team[131] used *Moringa oleifera* leaves as the precursor to prepare three-dimensional hierarchical porous carbons (HCPCs) with multidirectional porosity and a highly crumpled morphology. When the HCPCs were used as electrode materials of supercapacitors, they still had high capacitance retention and good cycle stability after 20 000 cycles of tests, with a specific energy density as high as 21.6 W h kg^{-1}. The surface morphology of HCPCs and the three-dimensional hierarchical interconnected porous structure provided more adsorption sites for electrolyte ions and also furnished a low resistance path for electrons (Fig. 10b). Their other study also found that carbon materials with a three-dimensional interconnected hierarchical porous structure were more conducive to electrochemical energy storage than those with a simple lamellar structure of horizontal stacking or vertical alignment (Fig. 10c).[52]

Heteroatom doping is a simple and efficient method to improve the performance of carbon-based electrode materials.[132,133] The influence of heteroatom doping on the performance of supercapacitors is mainly that the introduction of heteroatoms will affect the electrochemical interface energy of carbon materials and the properties of the electrical double layer, such as wettability, conductivity and ion adsorption properties.[134,135] In addition, heteroatom doping will change the electronic structure of the material and increase the pseudocapacitive effect. Nitrogen doping can improve the electronic mobility and hydrophilicity of carbon materials.[136,137] At present, a variety of nitrogen-doped BPGCs with excellent properties have been reported. Wang *et al.*[138] synthesized porous activated carbons with a high degree of graphitization *via* KOH activation of willow catkins. Interestingly, the electrochemical performance of porous activated carbons was more dependent on heteroatom contents than the specific surface

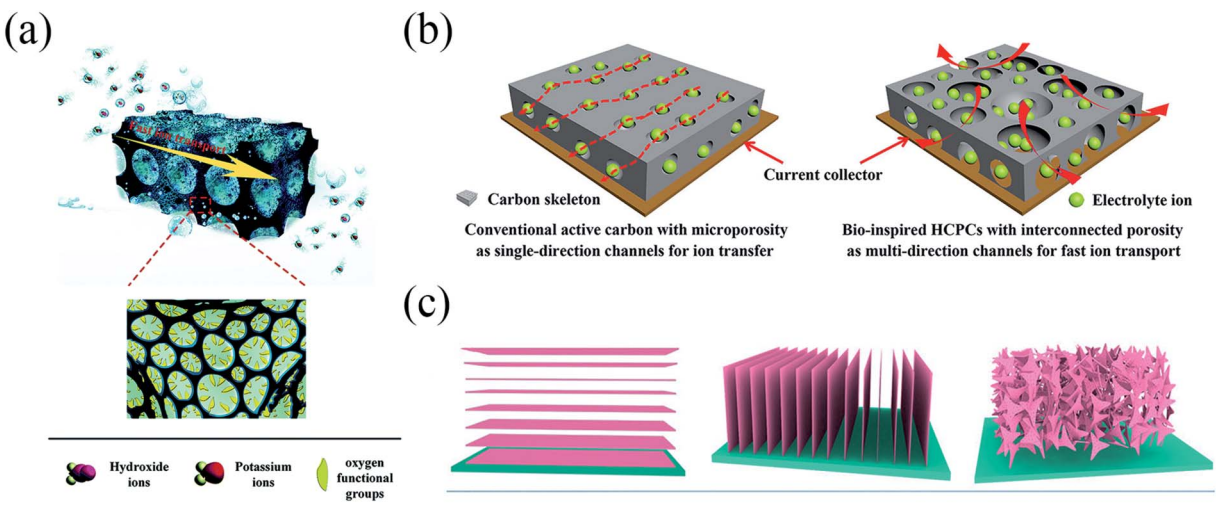

Fig. 10 (a) Schematic illustration depicting the interaction between GHCs and ions on the electrode. Reprinted with permission from ref. 51. Copyright 2018 the Royal Society of Chemistry. (b) Illustration of the carbon skeleton with single-direction porosity or multidirectional porosity for ion transfer. Reprinted with permission from ref. 131. Copyright 2018 American Chemical Society. (c) From left to right, a schematic diagram of the electrode material with a horizontally stacked layered structure, vertically aligned layered structure and three-dimensional interconnected hierarchical porous structure. Reprinted with permission from ref. 52. Copyright 2019 American Chemical Society.

area. The better electrochemical performance was an indication of the combination effects of electrical double layer capacitance and pseudocapacitance caused by the existence of active nitrogen and/or oxygen heteroatoms. Qiu *et al.*[139] reported the synthesis of oxygen-enriched hierarchical porous carbon (OHPC) through oxidation and activation of $KMnO_4$. The as-synthesized OHPC electrode showed a high specific capacitance of 290 F g^{-1} at a current density of 0.2 A g^{-1}. Meanwhile, the OHPC-based symmetric supercapacitors demonstrated superb long-term cycling stability (95.2% capacitance retention after 10 000 cycles) and an energy density of 14.7 W h kg^{-1}. The surface oxygen and nitrogen functional groups with a high content play an important role in the electrochemical performance of the electrode. Most of the biomass is rich in heteroatoms that can be embedded *in situ* into the carbon lattice during carbonization. The introduction of heteroatoms enhances electron conductance, improves surface wettability, and provides additional faradaic pseudocapacitance for enhanced electrochemical performance.

In a recent study by Chang *et al.*,[140] the effects of a hierarchical porous structure and heteroatom doping on the electrochemical properties of the prepared materials were also investigated simultaneously. Firmiana simplex fluff pre-impregnated with Co^{2+} was mixed with KOH and urea, and then nitrogen-doped hierarchical porous carbon materials (HN-DP-FSFC) with an appropriate graphitization degree were produced through a two-step calcination process (Fig. 11a). It was worth noting that urea acted not only as a source of heteroatom doping, but also as a template to achieve high micro-porosity and small mesoporous size (2–4 nm) (Fig. 11b–d). As shown in Fig. 11e–g, the electrode material assembled from HN-DP-FSFC exhibited groundbreaking high gravimetric capacitance (836 F g^{-1} at 0.2 A g^{-1}), excellent cycling stability (93% capacitance retention after 10 000 cycles), and high energy/power density (36.50 W h kg^{-1} at 140 W kg^{-1}). Considering the excellent performance of HN-DP-FSFC, the following two factors need to be taken seriously: (a) the effective microporous structure easily accepted ions and electrons and the mesopores with a size of 2–4 nm served as the high-speed channels of ion diffusion. (b) Nitrogen doping and graphitic structure enhanced the conductivity of HN-DP-FSFC and reduced the resistance of ion transport. The porous structure of

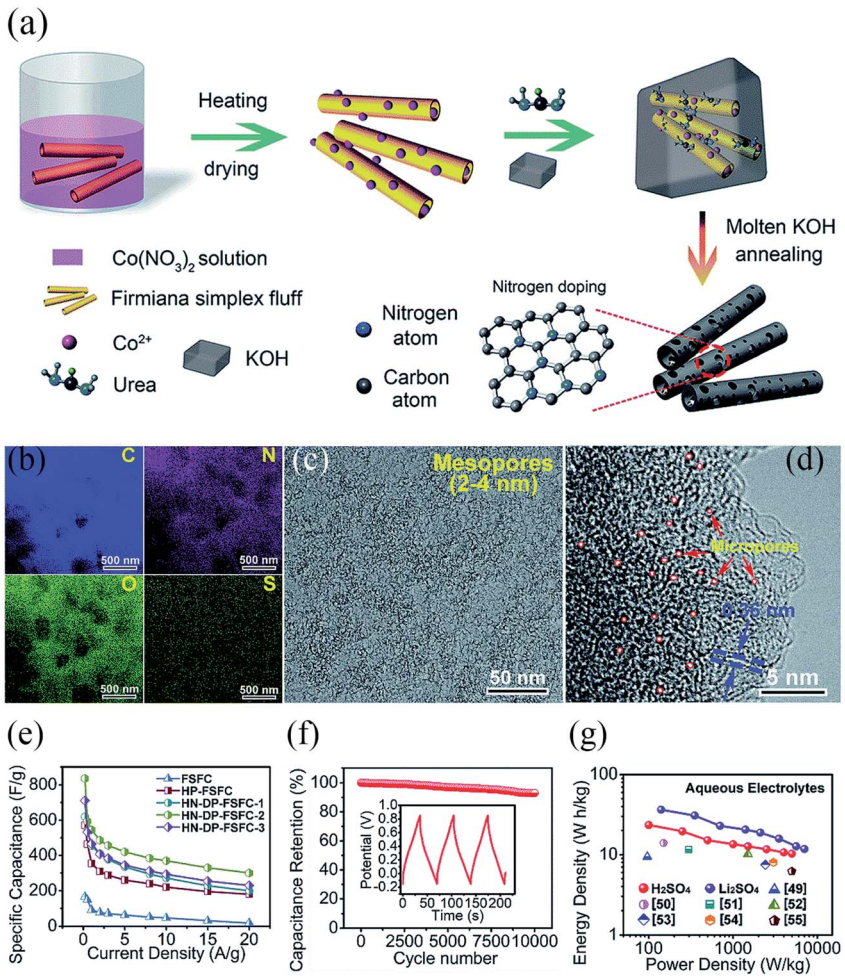

Fig. 11 (a) Graphical illustration of the fabrication of HN-DP-FSFC. (b) Corresponding elemental mapping images. (c) TEM image. (d) HR-TEM image. (e) Rate capability. (f) Cycling performance with the inset showing GCD curves. (g) Ragone plot in different electrolytes. Reprinted with permission from ref. 140. Copyright 2019 the Royal Society of Chemistry.

BPGCs plays an important role in improving the permeability of the electrolyte, rate of ion diffusion and electron transport, and area of ion adsorption caused by charges. The graphitic structure of BPGCs has a significant influence on their electrochemical performance. The better the graphitic structure is, the faster the electron transfer rate is, which is advantageous for reducing the internal resistance of the electrode material, improving rate performance, energy and power transmission efficiency. In addition, by introducing nitrogen and other heteroatoms into the carbon structure, more active sites can be obtained and the electrochemical properties of carbon materials can be improved. Therefore, it is necessary to rationally design a porous graphitic structure with heteroatom doping.

3.2 Lithium-ion batteries

As an important member of clean energy storage devices, the battery industry has become a new hot spot in global exploration.[141–144] Nowadays, lithium-ion batteries (LIBs) are widely used in portable electrical equipment, electric vehicles, aerospace and other fields, which have broad development and application prospects.[2,144,145] The lithium-ion battery, as a secondary battery, is the most outstanding comprehensive battery system with a high specific capacity, high operating voltage, high energy density, low self-discharge rate, no memory effect and other advantages at present.[2,146–148] For the battery system, the performance of the electrode material is the primary factor that determines the electrochemical properties and application value of the battery.[149,150] Graphite has been widely employed as a negative electrode material for LIBs for a long time. However, the theoretical capacity is low (372 mA h g^{-1}) and the rate performance is very limited, which makes it impossible to be commercially popularized.[151–154] Other materials with high theoretical capacity, such as silicon (4200 mA h g^{-1}),[155,156] suffer from serious capacity attenuation due to volume expansion in the charging and discharging process.[157–159] Therefore, it will become particularly important to explore new electrode materials with higher theoretical capacity and energy density. Various alloys (such as P, Sn, Sb or Ge)[160–164] and transition metal oxides (TMOs) (such as MnO, Fe_3O_4, Co_3O_4 or NiO)[165–169] have been proposed to replace graphite as the anode for LIBs. Unfortunately, the commercial application of these materials is still limited because they often undergo extremely severe volumetric changes during lithium insertion/extraction processes, while their inherent electronic conductivity is poor in the case of transition metal oxides.[144,170] In addition to improve the performance of lithium-ion batteries, parameters including high safety, sustainability, environmental friendliness and low cost also need to be considered.[142,171] Carbon-based anodes are still regarded as the most suitable choice for practical applications. According to current research, among all kinds of materials, biomass-derived carbon materials are promising negative electrode materials for lithium-ion batteries due to their extensive resources, low cost and stable electrochemical performance. BPGCs are conducive to the rapid transport of ions and electrons and the loading of active

Table 3 Representation of the performance of BPGCs from various biomass precursors as electrodes for LIBs

Biomass	Specific capacity	Rate capability	Cycling stability	Ref.
Microalgae	Specific charge capacities of 445 mA h g^{-1} and 370 mA h g^{-1} at 1C, respectively	Charge capacities of 445 and 370 mA h g^{-1} at 0.1C and 1C, respectively	Capacity retention of 95% after 500 cycles at 1C	27
Shell of broad beans	Initial discharge capacity of 845.2 mA h g^{-1} at 0.5C	—	Discharge capacity of 261.5 mA h g^{-1} after 100 cycles	254
Soybean	Storage capacity of 360 mA h g^{-1} in the 100th cycle at 0.5C	Around 190 mA h g^{-1} and 125 mA h g^{-1} at 8C and 16C, respectively	310 mA h g^{-1} in the 500th cycle at 2C, 275 mA h g^{-1} at 4C after 1000 cycles	258
Degreasing cotton	Discharge/charge capacities of 1298.1/860 mA h g^{-1} in the first cycle	950 mA h g^{-1} after 100 cycles at 1C, 850 mA h g^{-1} after 200 cycles at a 2C rate	Reversible capacity of 1070 mA h g^{-1} after 430 cycles at 0.2C	86
Natural silk	Specific capacity of 1865 mA h g^{-1} at 0.1 A g^{-1}	Reversible capacity of 212 mA h g^{-1} at 37.2 A g^{-1} (100C)	Specific capacitance retention of 92% after 10 000 cycles at 2 A g^{-1}	172
Hair	Discharge/charge capacities of 1006/689 mA h g^{-1} in the first cycle	387 mA h g^{-1} at 6 A g^{-1}	No capacity fading in 1000 cycles	174
Agaric	Discharge/charge capacities of 1465.1/894.5 mA h g^{-1} in the first cycle	Discharge capacities of 218.3 mA h g^{-1} at 10 A g^{-1}	Almost no decay in the specific capacities after 1000 cycles	267
Peanut dregs	Irreversible capacity of 1288 mA h g^{-1} in the initial cycle	Initial reversible capacity of 731 mA h g^{-1} at 100 mA g^{-1}	A capacity of 286 mA h g^{-1} at 1000 mA g^{-1} over 1000 charge/discharge cycles	173
Fish scale	Reversible capacities of 500 and 480 mA h g^{-1} at 75 mA g^{-1}	Discharge capacities of 224.7 and 232.5 mA h g^{-1} at 2000 mA g^{-1}, respectively	Capacity retention of about 80%	268

substances, thereby inhibiting the high concentration of active nanoparticles and buffering large volume changes of active materials. Therefore, as far as we know, BPGCs have been used as the anode material of LIBs (Table 3).

For the anode materials of LIBs, the following characteristics are particularly critical: (a) higher specific surface area can provide more active sites, thus providing a larger electrode/electrolyte interface, accelerating charge transfer and promoting Li^+ adsorption to increase capacity and minimize the polarization effect. (b) Hierarchical porous nanostructures can shorten the ion transport distance. Micropores and mesopores can ensure sufficient mass transport and further provide a convenient transport channel for the rapid movement of ions. (c) A higher degree of graphitization and nitrogen doping further improve the electrochemical activity, defects and conductivity of the material. For example, nitrogen-doped nanosheets with a high degree of graphitization and hierarchical porous structure were prepared through a simple and scalable one-step "activation-graphitization" joint route from natural silk by Hou *et al.*[172] The nanosheets were used as negative electrode materials for LIBs with an ultrahigh capacity of 1865 mA h g^{-1} (that of graphite is 372 mA h g^{-1}). Zhou *et al.*[154] found that high performance anode materials could be derived from biomass waste, where the hydrothermal process and graphitization treatment were used to convert wheat stalk into interconnected highly graphitic carbon nanosheets (HGCNS) (Fig. 12a). The highly ordered porous structure of HGCNS could provide abundant sites for Li ion storage and promote the rapid transmission of electrons and Li ions (Fig. 12b). Besides, HGCNS showed a low and flat charge–discharge potential due to the high degree of graphitization and the excellent graphitic structure, which greatly reduced the voltage hysteresis.[154] The obtained HGCNS had good electrochemical energy storage characteristics, and the HGCNS achieved an attractive capacity

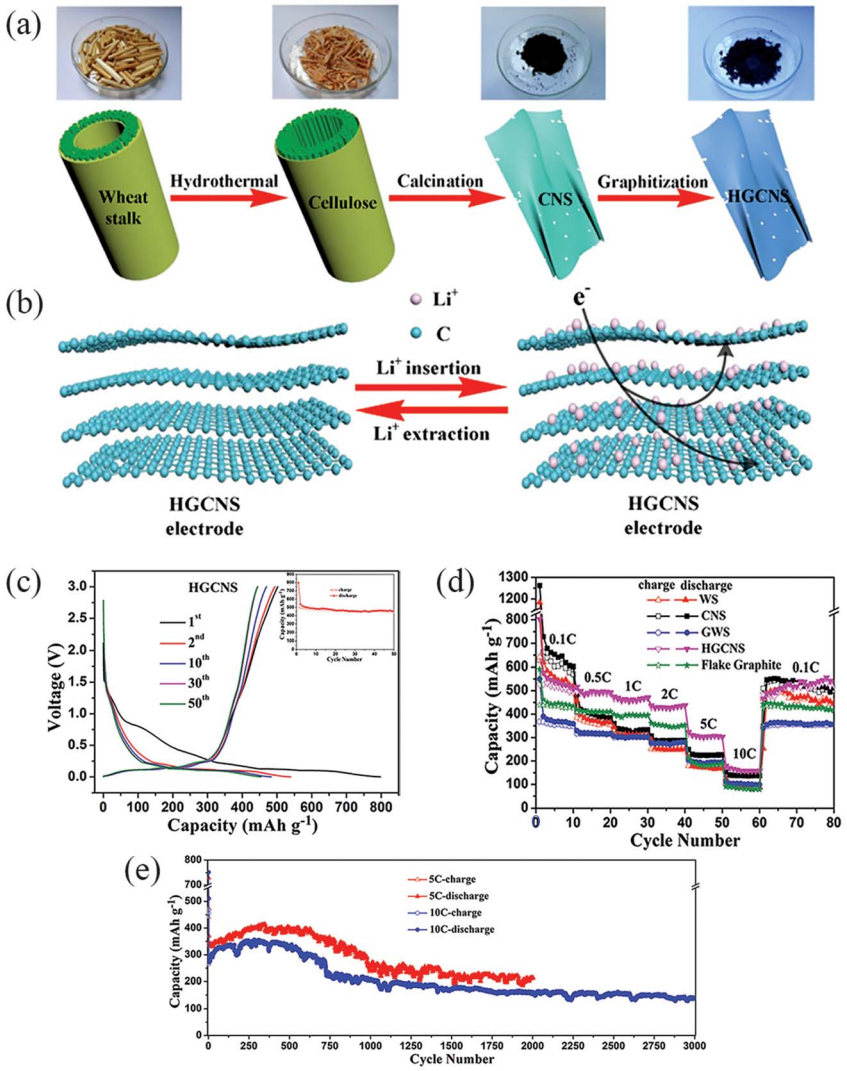

Fig. 12 (a) Schematic illustration of the synthesis process of HGCNS. (b) Schematic diagram of electron transmission and Li^+ storage in the HGCNS electrode. (c) Galvanostatic discharge/charge curves. (d) Rate performance. (e) Cycle performance. Reprinted with permission from ref. 154. Copyright 2016 the Royal Society of Chemistry.

of 502 mA h g^{-1} (Fig. 12c), excellent rate capability (Fig. 12d), and superior cycling performance (215 mA h g^{-1} at 5C after 2000 cycles and 139.6 mA h g^{-1} at 10C after 3000 cycles) (Fig. 12e) when it was used as the anode of LIBs.

It is very important to design and control the porous structure, graphitic structure and heteroatom doping of BPGCs to achieve high-performance LIBs. Yuan *et al.*[173] prepared carbon materials with a high graphitization degree, graphene-like structure and predominant mesopores from peanut residue by pre-carbonization and KOH activation. When it was applied as the anode of lithium ion batteries, the as-obtained product showed a high reversible capacity of 731 mA h g^{-1} at a current density of 100 mA g^{-1}, and retained a capacity of 286 mA h g^{-1} after 1000 cycles at a current density 1000 mA g^{-1}. The synergistic effects of the high graphitization degree, graphene-like structure, and major micropores greatly facilitated diffusion, intercalation/deintercalation of lithium ions and rapid electron transfer. Zhu *et al.*[174] ingeniously synthesized porous graphitic carbon microtubes (GP-CMTs) with deep pores and heteroatom co-doping by catalytic activation with nickel nitrate hydroxide from human hair (Fig. 13a). When they were used as the negative electrode material of lithium ion batteries, the GP-

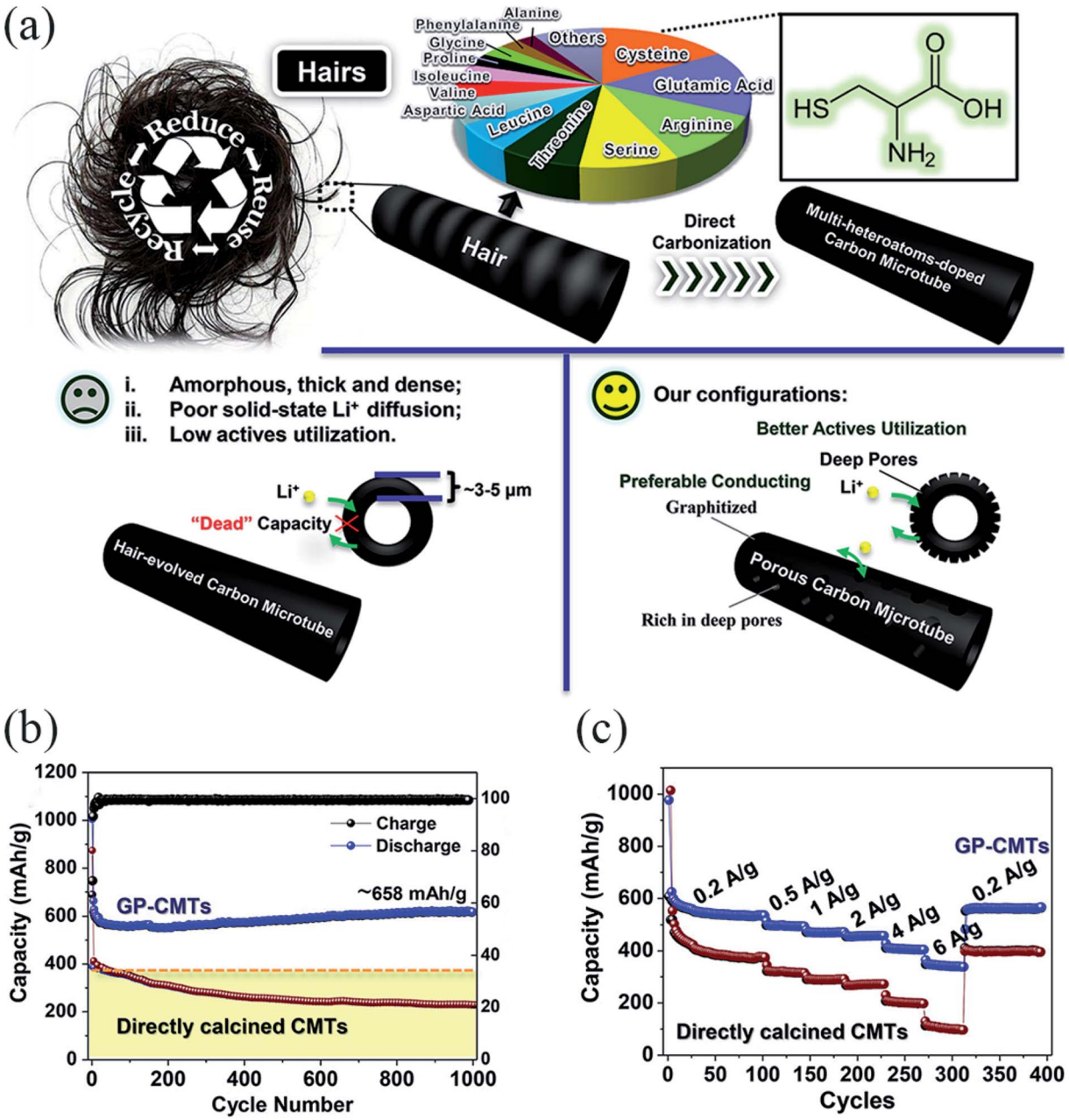

Fig. 13 (a) Schematics displaying the design idea of GP-CMTs for LIB applications. (b) Galvanostatic cycling behavior of G-PCMTs in a half-cell testing system. (c) Programmed cycling records of GP-CMTs in a half-cell testing system. Reprinted with permission from ref. 174. Copyright 2018 American Chemical Society.

CMTs had a high capacity of 387 mA h g^{-1} at a high current density of 6 A g^{-1} (Fig. 13c). The GP-CMTs had no capacity attenuation and still provided a high capacity of 658 mA h g^{-1} after 1000 cycles (Fig. 13b). The highly porous structure of GP-CMTs had the following functions: (i) it was beneficial to the effective contact between the electrode and the electrolyte and provided more active sites for redox reactions and increased the specific capacity of the electrode; (ii) it was beneficial to the rapid transmission of electrons and ions, thus improving the electrochemical utilization of the active materials of the electrode; (iii) it was beneficial to the repeated intercalation/deintercalation of ions in the reaction process, so as to improve the cycle stability of electrode materials. In addition, the high graphitization degree of the GP-CMTs realized rapid electron transfer in the electrochemical reaction process and promoted the electrochemical reaction. The heteroatoms supported on the carbon skeleton further improved the electrochemical activity, defects and conductivity of the GP-CMTs, providing a fast Faraday reaction and additional Li storage capacity.

3.3 Fuel cells

Fuel cells (FCs) are a new type of environment-friendly electrochemical energy conversion device that can directly convert chemical energy into electric energy without the combustion process.[175] They are characterized by high energy density, high energy conversion efficiency and cleanliness and have broad application prospects in the world.[176,177] The oxygen reduction reaction (ORR) of the cathode of FCs is a dynamic slow process involving multi-electron and multi-step elementary reactions,[178,179] which constitutes the rate control step in the overall ORR and largely determines the efficiency and cost of FCs.[180] In the practical application of FCs, the most critical restriction factor is the cathode ORR catalyst. At present, noble metal platinum (Pt)-based catalysts are still the most widely used catalysts with high catalytic activity for the ORR, and have a high price, poor stability/durability, weak CO poisoning resistance and tolerance to fuel (*e.g.* methanol) cross-over, thus greatly restricting the large-scale commercialization of FCs.[181,182] The catalysts are the core component of FCs, and provide the guarantee of normal and efficient operation and commercial applications of FCs. The demand for the grand scale applications of FCs has been more urgent with the increasing pressure of current environmental pollution. It is well known that green renewable biomass resources can be widely and comfortably obtained from nature and themselves contain naturally abundant heteroatoms (*e.g.*, N, O, and S). Biomass-derived carbon materials have begun to be studied as non-precious metal catalysts for the ORR.[183,184] Among them, BPGCs have attracted widespread attention as ORR catalysts due to their low cost, easy preparation, and high electrocatalytic performance (Table 4).

Doping nitrogen into BPGCs is essential for catalyzing the ORR. BPGC-derived nitrogen-doped non-metal catalysts have been extensively explored. Nitrogen doping can significantly improve the performance of catalyzing the ORR, mainly regarding the following three points:[185–187] (i) the introduction of nitrogen atoms breaks the electric neutrality of the carbon surface, resulting in the uneven distribution of charge density. Furthermore, the nitrogen atoms stimulate the electron delocalization of the adjacent carbon atom, resulting in a high positive charge density and spin density environment, thus promoting the adsorption and reduction reaction of O_2 on the carbon surface; (ii) nitrogen doping will import the carbon defect structure to adjust the electronic structure of sp^2 carbon to stimulate electrocatalytic activity; (iii) nitrogen doping enhances the conductivity of the catalyst and accelerates the ORR. The content and configuration of nitrogen doping are the two key factors affecting the electrocatalytic performance of BPGCs. Chatterjee *et al.*[188] prepared nitrogen-doped carbon nano-onions (N-CNO) by simply pyrolyzing nitrogen-rich goat skin trimming wastes to catalyze the ORR. Compared with other samples, it was known that the product obtained by pyrolysis at 750 °C for 8 hours had the best electrocatalytic performance and was superior to that of Pt/C catalysts in alkaline electrolytes due

Table 4 Representation of the performance of BPGCs from various biomass precursors as ORR electrocatalysts in FCs

Biomass	Onset potential (ORR activity)	Half-wave potential (ORR activity)	ORR stability	Ref.
Goat skin trimmings	50 mV *vs.* Ag/AgCl		About 10% decrease in current after 6 h	188
Taro stem	About 0.87 V *vs.* Hg/HgO		96.5% current retention after 20 000 s	189
Amaranth	0.27 V *vs.* Hg/HgO		Reduction current with a well-defined cathodic peak after 1000 cycles	35
Water lettuce		0.887 V *vs.* RHE	91% current retention after 30 000 s	192
Eclipta prostrata	0.25 V *vs.* Hg/HgO		94% current retention after 18 000 s	194
White beech mushroom	0.11 V *vs.* Hg/HgO		Superior long-term stability	199
Catkin	−98 mV *vs.* Ag/AgCl	−194 mV *vs.* Ag/AgCl	88.9% current retention after 20 000 s	201
Kelp	0.90 V *vs.* RHE	0.74 V *vs.* RHE	Less than 5% of initial activity loss during the 9 h test period	202
Rape pollen grain		0.86 V *vs.* RHE	99% current density retention after 20 000 s	203
Soybean	0.910 V *vs.* RHE	0.821 V *vs.* RHE	91.22% current retention after 7200 s	269
Chlorella		0.87 V *vs.* RHE	96% current density retention after 50 000 s	270
Reed stalk	0.99 V *vs.* RHE		94.8% current retention after 20 000 s at 0.8 V	271
Pomelo peel		0.86 V *vs.* RHE	92.5% current retention after 10000 s	272

to its highest total nitrogen and pyridinic N concentration. Pyridinic N as an active site played a leading role in the ORR activity of the N-CNO sample, and the mesoporous structure, hollow onion-like graphitic structure and high specific surface area contributed to better electrocatalytic performance. He *et al.*[189] obtained three-dimensional (3D) porous carbon through the KOH chemical activation and freeze-drying technology from taro stems for the first time, and then co-pyrolyzed it with melamine to prepare 3D nitrogen-doped porous carbon (3DNPC). Compared with commercial Pt/C catalysts, the 3DNPC catalyst had better stability and methanol tolerance. The electrocatalytic performance of the 3DNPC catalyst mainly came from the doping effect of the high content of graphitic N, the appropriate amount of total nitrogen and the developed 3D porous structure. Interestingly, Gao *et al.*[35] prepared a BPGC-based nitrogen-doped ORR catalyst with sparkling electrocatalytic properties by one step direct pyrolysis of amaranth. The catalytic performance of the prepared product at 800 °C was comparable to that of commercial Pt/C catalysts in alkaline medium. It was found that pyridinic N and graphitic N were the main active sites and promoted the fall of overpotential in the ORR process. In addition, the high specific surface area and cracking electrical conductivity of the prepared material also increased the catalytic activity. At present, compared with other nitrogen-doped types, pyridine N and graphite N have been more commonly found to produce or act as ORR active sites in

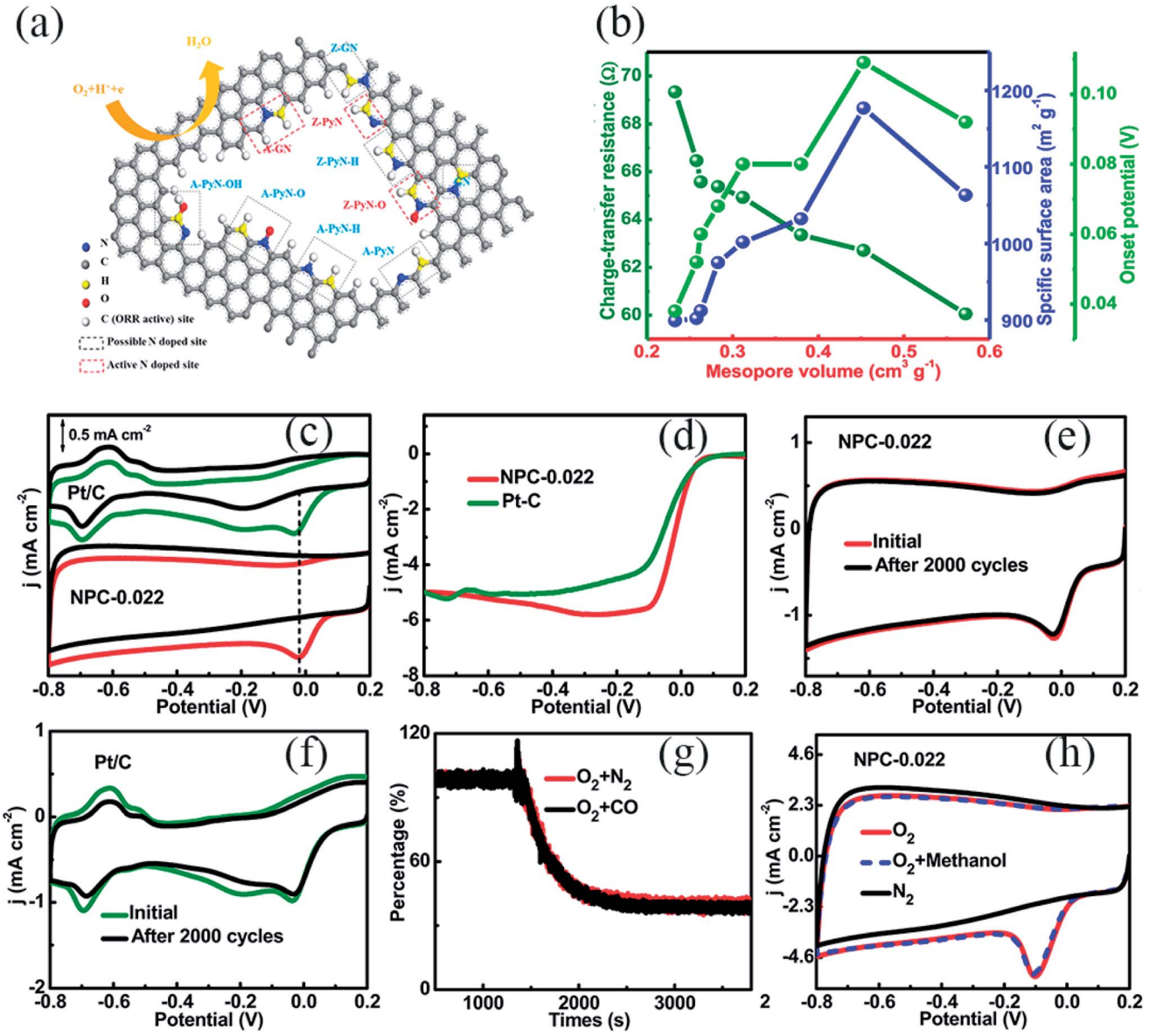

Fig. 14 (a) The structure of simulated ORR active sites according to density functional theory (DFT) calculations. (b) The significant influence of mesopore volume (vertical coordinate) on the charge-transfer resistance, specific surface area and ORR performance of NPC-*X*. (c) CV curves of NPC-0.022 and Pt/C. (d) LSV curves of NPC-0.022 and Pt/C. (e) The stability tests of NPC-0.022. (f) The stability tests of Pt/C. (g) The CO tolerance tests of NPC-0.022. (h) The methanol tests of NPC-0.022. Reprinted with permission from ref. 199. Copyright 2019 Elsevier B. V.

nitrogen-doped BPGCs.[190] The exact relationship between different forms of nitrogen doping configuration and active catalytic sites and the specific function and mechanism of catalyzing the ORR are still under exploration. Density functional theory (DFT) calculations to understand the role of pyridinic N and graphitic N in catalyzing the ORR have attracted attention.[191] Liu *et al.*[192] prepared nitrogen-doped hierarchical porous carbon nanosheets (N-HPCNSs) by a two-step carbonization method from water lettuce. The N-HPCNSs had respectable ORR catalytic activity under alkaline, neutral and acid conditions and showed bodacious cathode performance in a Zn-air fuel cell, microbial fuel cell and direct methanol fuel cell. The results showed that pyridinic N and graphitic N in N-HPCNSs are the key configurations to enhance the electrocatalytic performance. DFT calculations further showed that the porous structure on the surface of graphitic N was beneficial to the promotion of ORR activity and nitrogen doping of the edge sites played a leading role in the construction of ORR active sites (Fig. 14a). Due to the synergistic effect between different heteroatoms, heteroatoms co-doped may exhibit better electrocatalytic performance than nitrogen-doped BPGCs.[193–196] In another study by Gao *et al.*,[194] they produced N-, S-, and P-tridoped carbon nanorings from one-step pyrolysis of *Eclipta prostrata*. The as-prepared catalyst presented surpassing ORR performance with preferable fuel tolerance and long-term stability. Its ORR activity under alkaline conditions rivaled that of commercial Pt/C catalysts. For the catalytic performance of BPGC-derived non-metal catalysts with heteroatom doping, the configuration and position of doped nitrogen and the synergistic effect of heteroatom co-doping may be more critical than the total doped nitrogen contents.

In addition to heteroatomic doping, the exploration of the effect of the porous structure of BPGCs on catalyzing the ORR is also a worthwhile job.[182,197] The porous structure not only

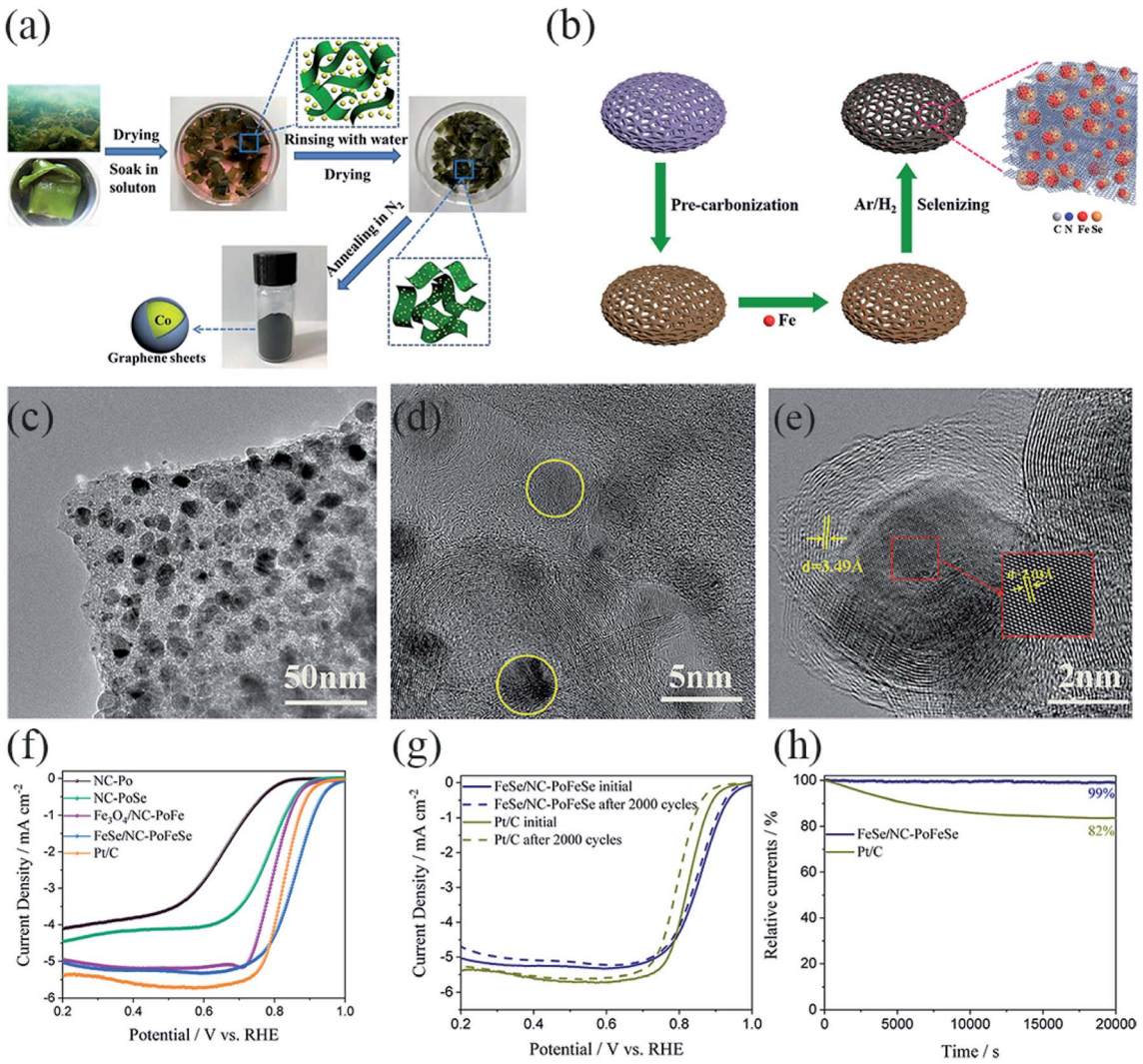

Fig. 15 (a) Fabrication procedure of Co/KCM. (c), (d) and (e) TEM images of Co/KCM-1000. (b) Schematic of the fabrication process of FeSe/NC-PoFeSe. Reprinted with permission from ref. 202. Copyright 2019 American Chemical Society. (f) LSV curves of the as-obtained materials. (g) Accelerated durability measurement of FeSe/NC-PoFeSe and Pt/C. (h) Chronoamperometric curves of FeSe/NC-PoFeSe and Pt/C at 0.85 V. Reprinted with permission from ref. 203. Copyright 2019 American Chemical Society.

enhances the performance of active sites by improving the mass transfer but also may lead to additional performance improvements by initiating new catalytic processes.[182,198] Li *et al.*[102] developed a simple double-template method to prepare nitrogen/oxygen-doped porous carbon materials from a variety of biomass using a mixture of $Mg_5(OH)_2(CO_3)_4$ and $ZnCl_2$ as the hard template. Through a series of comparative experiments, the prepared catalyst with a hierarchically macro-/meso-/microporous structure had better ORR electrocatalytic activity than the catalysts with a meso-/microporous or macro-/mesoporous skeleton. For the catalysts with a macro-/meso-/microporous structure, those with a larger ratio of mesoporous and macroporous volume possessed superior ORR electrocatalytic activity. The hierarchical porous structure was not only conducive to the mass transfer process but also exposed more active sites with a larger specific surface area. This study by Li *et al.*[102] mainly delineated the relationship between the pore size ranges (the horizontal coordinates of the pore size distribution (PSD)) of BPGCs and ORR performance. Zhao *et al.*[199] further elucidated how the changes of the vertical coordinates of PSD of BPGCs affect their electrocatalytic performance. The vertical coordinates of PSD mainly determine the number and volume of macropores, mesopores and micropores, which significantly affects the mass transfer and the density of the ORR active sites in catalyzing the ORR process. They fabricated a series of nitrogen/oxygen-doped microporous/mesoporous catalysts (NPC-*X*) with the same pore size ranges from white beech mushrooms for the ORR by hydrothermal carbonization and high temperature calcination. The vertical coordinate change of PSD of the as-prepared catalysts was achieved only by the change of mesopore volume, and the morphology, graphitization degree, specific surface area and chemical composition of these catalysts are virtually consistent. The results showed that NPC-0.022 with a mesopore volume of 0.453 $cm^3\ g^{-1}$ had the best electrocatalytic performance (Fig. 14b), which had a catalytic activity that was roughly the same as that of commercial Pt/C catalysts (Fig. 14c and d) and had better long-term cycle stability (Fig. 14e and f), excellent methanol resistance and CO resistance than commercial Pt/C catalysts (Fig. 14g and h). The ORR usually occurs in the gas/liquid/solid three-phase boundary region of the catalyst, involving electron and proton transfer, O_2 and product water inflow or outflow. Appropriate porous structures, such as an interconnected hierarchical porous structure and three-dimensional open porous structure, are conducive to the penetration of the electrolyte and the rapid transport of ions and O_2, so as to improve the ORR activity.

Biomass-derived transition metal nitrogen-doped carbon (B@M-N-C, M = Fe, Co, Ni) materials have been considered to be promising ORR catalysts. There are several possible explanations for the loss of activity of M–N–C catalysts:[200] (i) the etching and loss of metal ions; (ii) the corrosion of active sites by H_2O_2 and other radicals generated in the reaction; (iii) the protonation of active sites and subsequent adsorption of other cations lead to the deactivation of sites. The presence of transition metals in B@M–N–C catalysts is critical for the formation of highly graphitic carbon nanostructures *in situ*, which is momentous for the high corrosion resistance and stability of the B@M–N–C catalysts to inhibit their deactivation. Li *et al.*[201] used the one-pot pyrolysis of a mixture of a catkin, $FeCl_3$, and melamine to construct iron and nitrogen co-doped carbon fibers with highly graphitic carbon nanotubes for the ORR. The carbon nanotubes generated by catalytic graphitization of the doped iron contributed to the high specific surface area and good porous structure of the as-prepared catalyst, which significantly strengthened the electrocatalytic performance. It was also found that Fe–N clusters, pyridinic N, and graphitic N served as the catalytic active sites of the ORR. The active transition metal nanoparticles in B@M–N–C catalysts could suffer from instability. It is an effective strategy to encapsulate them in nitrogen-doped BPGCs or anchor them on nitrogen-doped BPGCs to prevent them from poisoning and agglomeration. At the same time, it can avoid the dissolution and migration of the active transition metal nanoparticles and improve the overall cycle life of the catalysts. Wu *et al.*[202] obtained heteroatom-doped carbon (Co/KCM) by directly carbonizing kelp pre-impregnated with $Co(NO_3)_2$, in which Co nanoparticles were encapsulated by multilayer graphene (Fig. 15a). Co nanoparticles are uniformly dispersed in Co/KCM, and the surface of the particles is encapsulated by multiple layers of graphene (Fig. 15c–e). The prepared Co/KCM-1000 catalyst exhibited highly efficient electrocatalytic activity, high stability and methanol tolerance in 1.0 M KOH solution. Encapsulating transition metal active particles into nitrogen-doped BPGCs is considered to be a very promising method to improve the activity and stability of electrocatalysts. First, the heteroatom-doped carbon shell has conductivity and porosity, which facilitates electron transfer and electrolyte penetration. Second, the heteroatom-doped carbon shell prevents the corrosion of transition metal nanoparticles in acidic and alkaline solutions. Wang *et al.*[203] used rape pollen grains as a biomass precursor and mixed ferric ammonium sulfate and selenium powder to obtain nitrogen-doped hollow carbon (FeSe/NC-PoFeSe) anchored with FeSe nanoparticles through pyrolysis and activation (Fig. 15b). Compared with Pt/C catalysts, the ORR half-wave potential of FeSe/NC-PoFeSe was positively shifted by 30 mV, and the catalyst durability was remarkable (Fig. 15f–h). The catalyst had an interconnected porous carbon skeleton, which easily transported substances and electrons. It was coupled with FeSe nanoparticles to increase ORR catalytic activity. In general, the research of nitrogen-doped BPGC-derived oxygen reduction electrocatalysts has entered the "deep water area" of electronic structure modulation, heteroatom-doped configuration regulation and porous structure control of nitrogen-doped BPGCs, and many valuable ideas, strategies and opinions have been presented. The following problems need to be focused on and solved in the future: (i) it is difficult for most of the nitrogen-doped BPGCs to show high enough activity and stability under acidic conditions. The reason for the difference in the electrocatalytic activity of the catalyst in electrolyte solutions in different pH ranges needs to be analyzed. (ii) Although most of the prepared catalysts have good durability in the catalytic process, the specific stability mechanism has not been further discussed. (iii) The type,

composition and structure of catalytic active sites need to be further defined. The construction process of the ORR catalytic active center and the catalytic principle of each active site for oxygen reduction need to be further studied. The DFT theoretical calculation method and more advanced *in situ* characterization equipment are also needed.

4 BPGCs for environmental applications

4.1 Adsorbent materials

Biomass-derived porous carbon materials have been extensively explored in recent years.[16,204–208] In addition, activated carbon has also widely used in environmental protection due to its large specific surface area and developed porous structure. BPGCs with a good porous structure, graphitic structure and heteroatom doping have also been explored as environmental remediation materials differing from activated carbon (Table 6). As shown in Table 5, they were distinguished. As far as we know, BPGCs have also been studied as highly efficient adsorbents for the removal of contaminants.[209–215] For instance, highly porous graphitic carbon with heteroatom doping was fabricated by Liu *et al.*[209] from fish waste. The as-prepared porous graphitic carbon presented a maximum adsorption capacity of 285.71 mg g^{-1} for acid orange 7. The macropores and mesopores of the porous graphitic carbon promoted mass transportation, and the high surface area and heteroatom doping provided sufficient active sites. The π–π interaction formed between the graphene-like structure on the surface of carbon materials and the aromatic ring of organic pollutants was conducive to the adsorption of pollutants. Zhong *et al.*[212] prepared magnetic biochar (MBC) by microwave-assisted pyrolysis of a rice husk and $FeSO_4$ mixture. The adsorption and reduction mechanism of hexavalent chromium [Cr(VI)] in the aqueous phase by porous graphitic MBC was studied. It was found that MBC with high conductivity easily acted as an electron conducting medium to promote the transfer of electrons from persistent free radicals in MBC to Cr (VI), thus achieving the reduction of Cr(VI) to trivalent chromium [Cr(III)] with low toxicity (Fig. 16a).

Graphene is a two-dimensional nanomaterial with a high theoretical surface area (2630 $m^2 g^{-1}$), strong π–π interaction, and excellent mechanical, electrical, optical and other properties,[216,217] and is often considered as a new type of high-efficiency adsorption material in the field of water purification.[218–220] Recently, graphene-based porous carbon materials derived from biomass have received extensive attention in the adsorption and removal of organic pollutants (including dyes). Gupta *et al.*[210] reported an effective strategy for the synthesis of a graphene-like porous carbon nanostructure (BGBH-C-K) *via* alkali-activation from Bengal gram bean husk (BGBH). BGBH-C-K showed excellent adsorption performance toward methylene blue (MB) and methyl orange (MO) with adsorption capacities of 469 mg g^{-1} and 418 mg g^{-1}, respectively. The large pore volume and high specific surface area of BGBH-C-K provided sufficient channels for the adsorption of MB and MO, and the large number of micropores well intercepted pollutants on the adsorption sites. In addition, the π–π interaction between the graphene-like thin layer in BGBH-C-K and the aromatic ring of MB and MO was mainly responsible for the adsorption performance of BGBH-C-K (Fig. 16b and c). Xiao *et al.*[211] used sugarcane bagasse treated with the activation and graphitization process to obtain a graphene-like material (FZS900) with a vertical stacking structure of graphene-like nanosheets and a high specific surface area (2280 $m^2 g^{-1}$). The study found that FZS900 had an extremely high adsorption capacity for four aromatic organic pollutants (naphthalene, phenanthrene, 1-naphthol and methylene blue). The co-assembly adsorption mechanism of the FZS900 adsorption process was proposed, which was small molecule induced graphene nanosheet layer structure reorganization. Interestingly, naphthalene (or phenanthrene) broke the framework of the originally stable FZS900 graphene nanosheet layer structure. Furthermore, the formation of the large area π–π interaction between naphthalene (or phenanthrene) and graphene nanosheet layer led to the ordered nanoring structure. For 1-nanophenol and methylene blue, because they contained hydrophilic functional groups, the coassembly process could not occur, so they produced a more dispersed or more agglomerated phenomenon. The above phenomena are shown in Fig. 16d–m. Heteroatom doping can

Table 5 Comparison of BPGCs with graphitic carbon materials (GCs) and activated carbon materials (ACs)

Source, structure or property	BPGCs	GCs	ACs
Precursor	Biomass (excluding biomass-derived chemicals)	Graphite, carbon nanotubes, graphene *etc.*	Coal, asphalt, biomass *etc.*
Porous structure	Mainly hierarchical porous structure, three-dimensional interconnected porous structure	Poor porous structure	Well-developed porous structure
Graphitic structure	Containing amorphous carbon and graphitic carbon	Graphitic carbon	Amorphous carbon
Graphitization degree	Relatively high graphitization degree	High graphitization degree	Low graphitization degree
Specific surface area	Large specific surface area	Small specific surface area	Large specific surface area
Heteroatom doping	High heteroatom content	No heteroatom doping	Low heteroatom content

Table 6 Summary of BPGCs in environmental applications

Environmental applications	Biomass feedstock	Substances to be removed	Performance	Ref.
Adsorbent materials	Fish waste	Acid orange 7	The maximum adsorption capacity was 285.71 mg g^{-1}	209
	Rice husk	Cr(VI)	The removal efficiency and adsorption capacity of Cr(VI) were 84.3% and 8.35 mg g^{-1}, respectively	212
	Bengal gram bean husk	Methylene blue and methyl orange	Excellent adsorption capacities for methylene blue (469 mg g^{-1}) and methyl orange (418 mg g^{-1})	210
	Sugar cane	Naphthalene, phenanthrene and 1-naphthol	The adsorption capacities for naphthalene, phenanthrene, and 1-naphthol were 615.8, 431.2, and 2040 mg g^{-1}, respectively	211
	Oil tea shell	Cr(VI)	The maximum adsorption capacity for Cr(VI) was 355.0 mg g^{-1}	221
	Oil tea shell	SO_2	The SO_2 adsorption capacity of 10.7 mmol g^{-1} at 298 K and 1.0 bar	223
	Shrimp shell	CO_2	The adsorption capacity for CO_2 was 6.82 and 4.20 mmol g^{-1} at 273 and 298 K and 1 bar, respectively	224
	Algae	CO_2	The adsorption capacity of CO_2 was 5.7 and 3.9 mmol g^{-1} at 273 and 298 K, respectively	225
	Algae	C_3H_8, C_3H_6, C_2H_6, and C_2H_4	The adsorption capacities were 11.5, 11.3, 6.84, and 5.71 mmol g^{-1} for C_3H_8, C_3H_6, C_2H_6, and C_2H_4, respectively	222
Catalyst for persulfate (PS) activation	Shrimp shell	2,4-Dichlorophenol	The removal efficiency for 2,4-dichlorophenol reached 100% in 120 minutes	34
	Myriophyllum Aquaticum	Bisphenol A and Tartrazine	The removal efficiencies for bisphenol A and tartrazine were 98% and 95% in 100 minutes, respectively	244
	Corn	Orange II	Complete orange II removal in 6 minutes	241
	Spirulina residue	Sulfamethoxazole	Complete sulfamethoxazole removal in 45 minutes	242
	Enteromorpha	Paracetamol	Complete paracetamol removal in 60 minutes	57
	Coffee ground	Bisphenol A.	The removal efficiency for bisphenol A was around 99% in 60 minutes	248
	Human hair	Bisphenol A	The removal efficiency for bisphenol A was 98.4% in 60 minutes	56
Support for photocatalytic materials	*Camellia oleifera* shell	Cr(VI)	Complete Cr(VI) removal	249
	Straw	Tetracycline hydrochloride	High efficiency for tetracycline hydrochloride removal	250

effectively regulate the surface electron characteristics of porous carbon materials, thus enhancing their adsorption capacity to heavy metal ions.[221] Chen *et al.*[221] prepared nitrogen and phosphorus co-doped porous carbon materials from oil tea shells, whose maximum adsorption capacity for Cr(VI) was up to 355.0 mg g^{-1}. Nitrogen-containing and phosphorus-containing

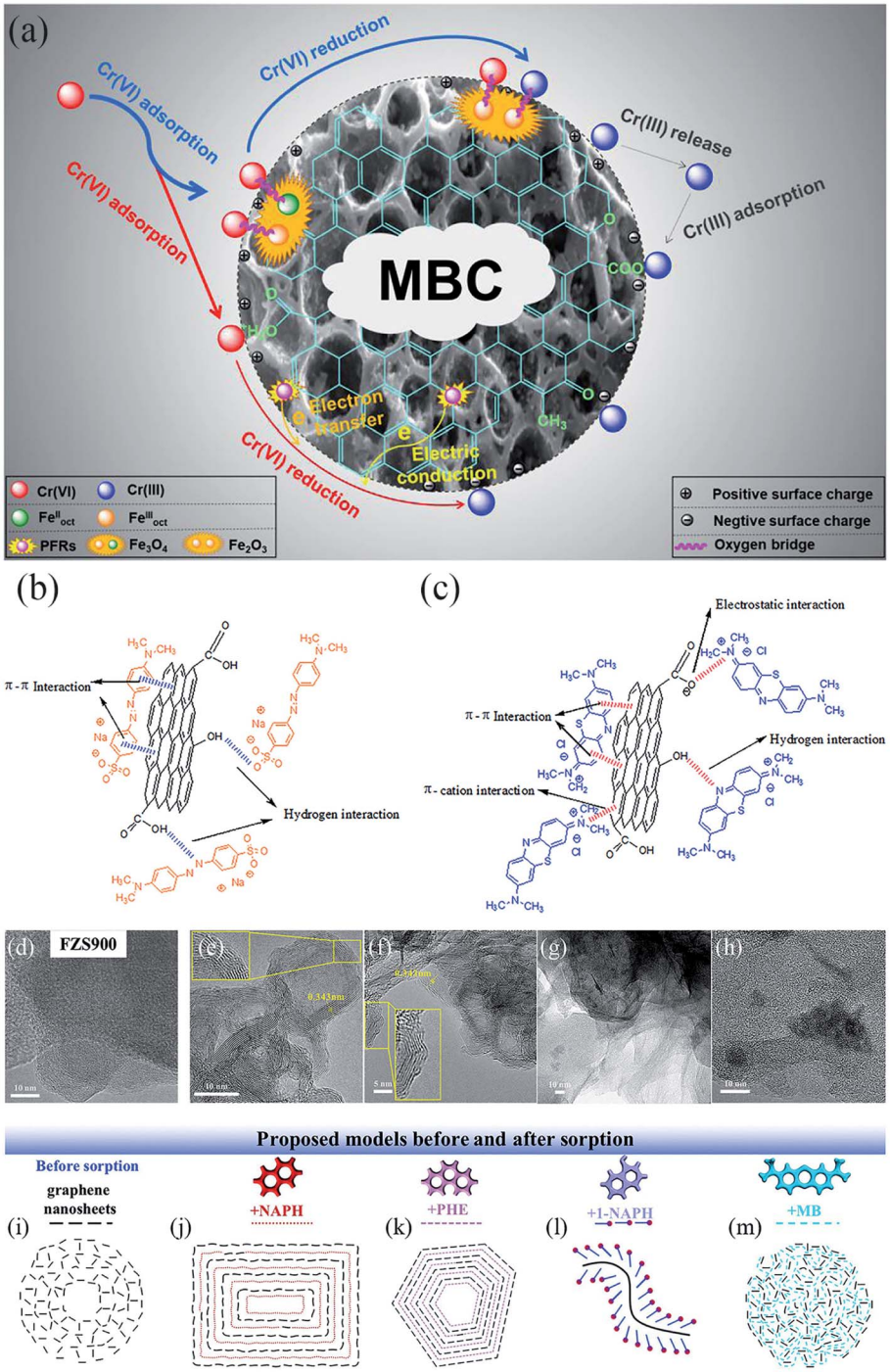

Fig. 16 (a) Schematic diagram of the Cr(VI) removal mechanism. Reprinted with permission from ref. 212. Copyright 2018 Elsevier B. V. (b) Illustration of the interactions of BGBH-C-K with MO dye molecules. (c) Illustration of the interactions of BGBH-C-K with MB dye molecules. Reprinted with permission from ref. 210. Copyright 2019 Elsevier B. V. HR-TEM images of FZS900 (d) before and after (e) NAPH, (f) PHE, (g) 1-NAPH, and (h) MB were adsorbed. (i) Synthetic illustration of the graphene nanosheet structure of FZS900. (j)–(m) The simulated structure of FZS900 with the absorption of NAPH, PHE, 1-NAPH, and MB, respectively. Reprinted with permission from ref. 211. Copyright 2017 American Chemical Society.

functional groups brought about by the doping of nitrogen and phosphorus played an important role as adsorption sites in the removal of Cr(VI).

BPGCs can be used not only as adsorbents to remove heavy metals and organic pollutants from the environment, but also for gas adsorption and mixed gas separation.[222,223] Yang *et al.*[224] prepared porous carbon materials from nitrogen-rich shrimp shells by KOH activation. Due to the synergistic effect of their abundant microporous structure, large specific surface area and high nitrogen content, the as-prepared samples had high CO_2

adsorption performance. At 273 and 298 K and 1 bar, the CO_2 adsorption capacity was 6.82 and 4.20 mmol g^{-1}, respectively. In addition, the as-prepared sample also had outstanding separation performance towards mixed gases. The nitrogen element in porous carbon materials changes the surface chemical properties of carbon materials and has a certain influence on the structure of carbon materials, so that they have high selectivity and high adsorption capacity for CO_2 adsorption.[225,226] Using algae, which have a wide range of sources and relatively high nitrogen content, can effectively overcome the disadvantages of the current preparation methods of nitrogen-doped carbon materials. Wang *et al.*[225] obtained a nitrogen-doped porous carbon adsorbent by high-temperature KOH activation with algae (*N. Salina*) as the precursor. At different temperatures of 273 K and 298 K, the adsorption capacity of the adsorbent for CO_2 was 5.7 and 3.9 mmol g^{-1}, respectively. More importantly, the adsorbent also showed good selectivity for CO_2/N_2, CO_2/CH_4 and CH_4/N_2. The good performance of the adsorbent was mainly due to the combination of the high content of pyridinic-N, large specific surface area and lots of tiny holes. In addition to its excellent performance in the adsorption and separation of CO_2, algae-derived nitrogen-doped porous carbon materials were also used in the selective separation of light hydrocarbons. Zhang *et al.*[222] obtained nitrogen-doped porous carbon adsorbents by pyrolyzing mixtures of algae, $K_2C_2O_4$ and melamine. The adsorbent had excellent adsorption capacities of 11.5, 11.3, 6.84, and 5.71 mmol g^{-1} for C_3H_8, C_3H_6, C_2H_6, and C_2H_4, respectively. The adsorbent possessed outstanding separation selectivity for C3/C1 (189), C2/C1 (15.3), and C3/C2 (9.81) at 298 K and 1.0 bar. For gas adsorption, microporous structures general show better performance, and hierarchical structures with micropore, mesopore and macropore coexistence can significantly improve the mass transfer during the separation process, thus improving the dynamic separation ability and further optimizing adsorption performance. In addition, doping of heteroatoms improves the intrinsic polarity of carbon-based skeletons and constructs more active adsorption sites, which is an effective means to significantly change and enhance the adsorption activity of BPGCs.

4.2 Catalyst for persulfate (PS) activation

In recent years, advanced treatment of water pollution based on oxidative degradation of organic pollutants by persulfate (PS) activation has attracted much attention.[227–229] The construction of a highly efficient catalytic system is the main research direction of PS oxidation technology, the core of which is the design of a high-performance catalyst.[230,231] However, metal ions will inevitably spill during the use of traditional metal-based catalysts, which lead to secondary pollution of water and threaten the water ecological environment, drinking water safety and human health.[229,232] Therefore, the development of safe, efficient and economical non-metallic carbon-based catalysts is the key to the construction of green PS oxidation systems. At present, carbon nanomaterials (*e.g.* carbon nanotubes, graphene and nanodiamonds) are showing more and more attractive prospects as a promising class of non-metallic active catalysts in environmental pollution control.[233–238] However, the preparation of carbon nanomaterials is complex and costly, which hinders their practical application.[239] Using biomass wastes to prepare functional carbon materials can not only provide cheap materials for environmental restoration, but also solve the problem of waste disposal at the same time. It is a very ideal strategy of "treating wastes with wastes". As far as we know, BPGCs have begun to emerge as catalysts for persulfate (PS) activation.[34,57,240–245]

Due to the superior porous and graphitic structure of BPGCs, the BPGCs/PS system has a dual effect of adsorption and oxidative degradation of organic contaminants. The porous structure of BPGCs realizes the pre-adsorption of pollutants, which is an important step for the subsequent catalytic degradation of pollutants, and it can also promote the electron transfer of the PS activation process. The good conductive surface created by the graphitic structure of BPGCs can be used as a good medium to achieve simple and efficient transfer of electrons, which is often found in a non-radical pathway that activates PS. Yu *et al.*[34] obtained an excellent catalyst with a high graphitization level and hierarchical pore structure by one-step direct pyrolysis of shrimp shells for activating peroxydisulfate (PDS) to degrade 2,4-dichlorophenol (2,4-DCP). The hierarchical porous structure and graphitic carbon had proved to be two important positive factors that affect the activation process of PDS. The prepared catalyst promoted rapid electron transfer from pollutants to PDS by its strong adsorption on PDS and 2,4-DCP and as a key electron transfer medium. Fu *et al.*[244] prepared porous graphitic biochar *via* modifying *Myriophyllum aquaticum* with K_2FeO_4, whose graphitic structure acted as a bridge for electron transfer from *p*-hydroxybenzoic acid (HBA) to peroxymonosulfate (PMS) in the secondary non-radical pathway of oxidative degradation of pollutants. The degree of graphitization and porous structure were closely related to the rate and efficiency of electron transfer. Another study conducted by Fu *et al.*[241] successfully loaded $MnFe_2O_4$ nanoclusters onto graphitic hierarchical porous carbon through hydrothermal synthesis to activate PMS to degrade organic pollutants (such as livestock and poultry farming antibiotics) in water. The synthesized catalyst from corn stalks showed the best catalytic performance, which was mainly attributed to the optimum balance between the degree of graphitization and the pore volume of micropores, and the uniform distribution of $MnFe_2O_4$ nanoclusters. This study proposed the mechanism of degradation of organic pollutants: a radical pathway based on $^{\bullet}SO_4^-$ and $^{\bullet}OH$, a non-radical pathway based on $^1O_2$, and a non-radical pathway based on electron transfer (Fig. 17a).

Furthermore, some studies have begun to focus on BPGCs with nitrogen doping, which can effectively improve the catalytic activity of BPGCs.[246,247] Ho *et al.*[242] utilized C-phycocyanin extracted (C-CP) *Spirulina* residue (SDBC) to produce N-doped porous graphitic carbon *via* thermal pyrolysis for peroxydisulfate (PDS) activation. The SDBC had excellent oxidation efficiencies for various aqueous microcontaminants. Nitrogen doping can introduce different N configurations (graphitic N, pyridinic N and pyrrolic N). The amount of nitrogen doping and

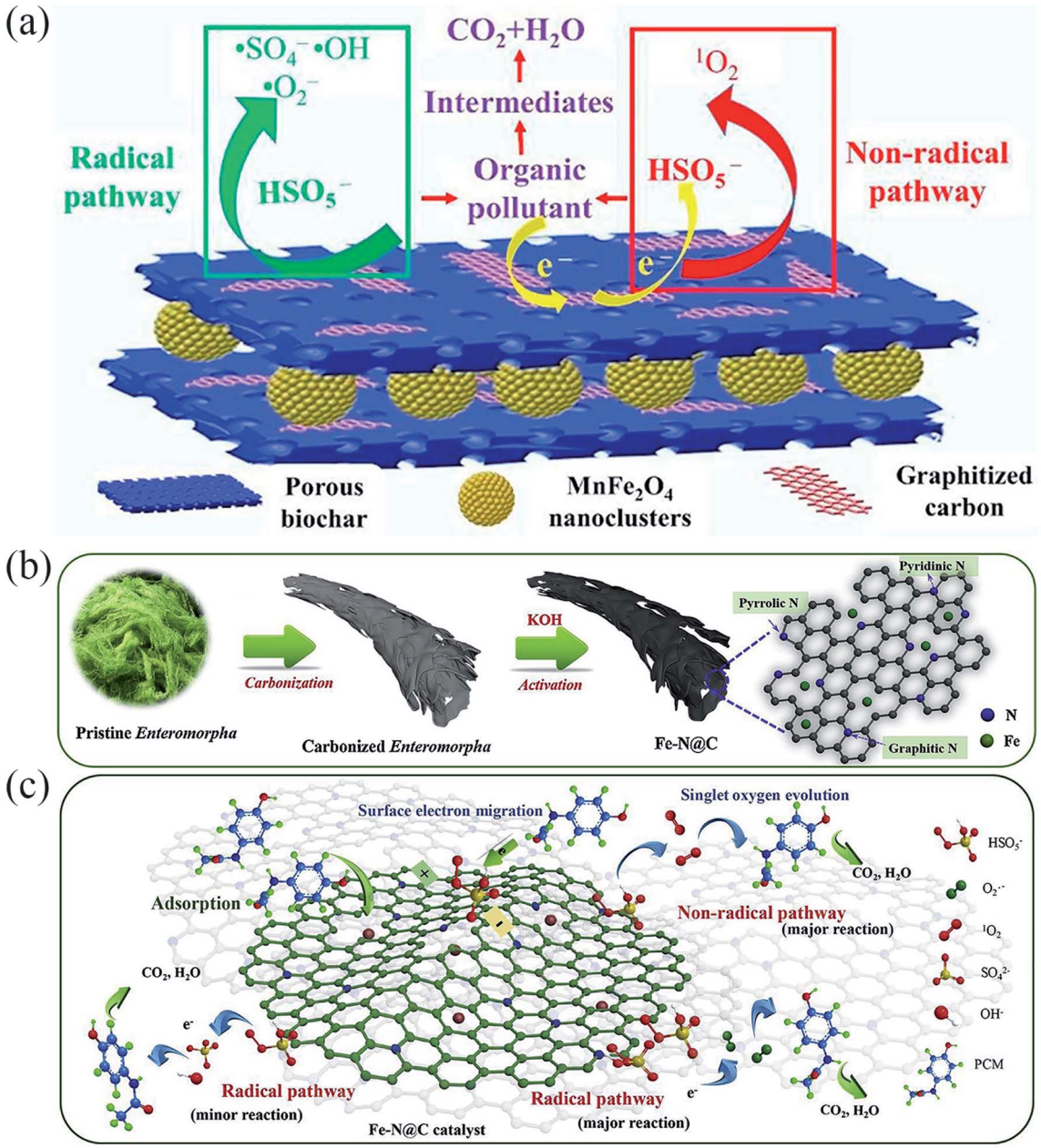

Fig. 17 (a) The proposed mechanism for organic oxidation. Reprinted with permission from ref. 241. Copyright 2019 Elsevier B. V. (b) Schematic of the synthesis process of Fe–C@N from *Enteromorpha* biomass. (c) Schematic Mechanism of PCM removal in the Fe–N@C/PMS system. Reprinted with permission from ref. 57. Copyright 2019 Elsevier B. V.

the composition of nitrogen configuration in BPGCs will affect their catalytic activity. Chen *et al.*[57] prepared a green and highly efficient Fe–N co-doped *Enteromorpha*-based carbon material (Fe–N@C) to activate peroxymonosulfate (PMS) for the degradation of paracetamol (PCM) based on the characteristics of *Enteromorpha* with high contents of N and Fe, and successfully built a new catalytic oxidation system (Fe–N@C/PMS) using the *Enteromorpha*-based carbon material as the PMS catalyst (Fig. 17b). There was a high linear positive correlation between the content of graphitic N in the catalyst and the removal rate constant of organic pollutants. The presence of graphitic N promoted the adsorption of PMS on the Fe–N@C material, thereby enhancing the activation of PMS. In the Fe–N@C/PMS system, both the radical pathway and non-radical pathway were responsible for PCM removal (Fig. 17c). Oh *et al.*[248] revealed that coffee ground with urea as a nitrogen dopant pyrolyzed at 1000 °C had the best catalytic performance to activate PMS to remove bisphenol A, which could be attributed to the combination of its high graphitization properties, the best N bonding configuration ratio and the large surface area. It was found that the conversion of graphitic N to pyridinic N could be closely related to the activation of PMS. The durability of catalyst surface activity could be enhanced by increasing the content of graphitic N (obtained from the reduction of pyridinic N) *via* heating treatment.

4.3 Support for photocatalytic materials

BPGCs have been developed as good functional materials for photocatalyst modification due to their abundant pore structure, remarkable electrical conductivity and light absorption. The combination of the photocatalyst and BPGCs can not only improve the stability of the photocatalyst, but also reduce the reaction distance between pollutants and the photocatalyst, thus increasing the efficiency of photocatalytic degradation. Therefore, BPGCs combine with the high-efficiency

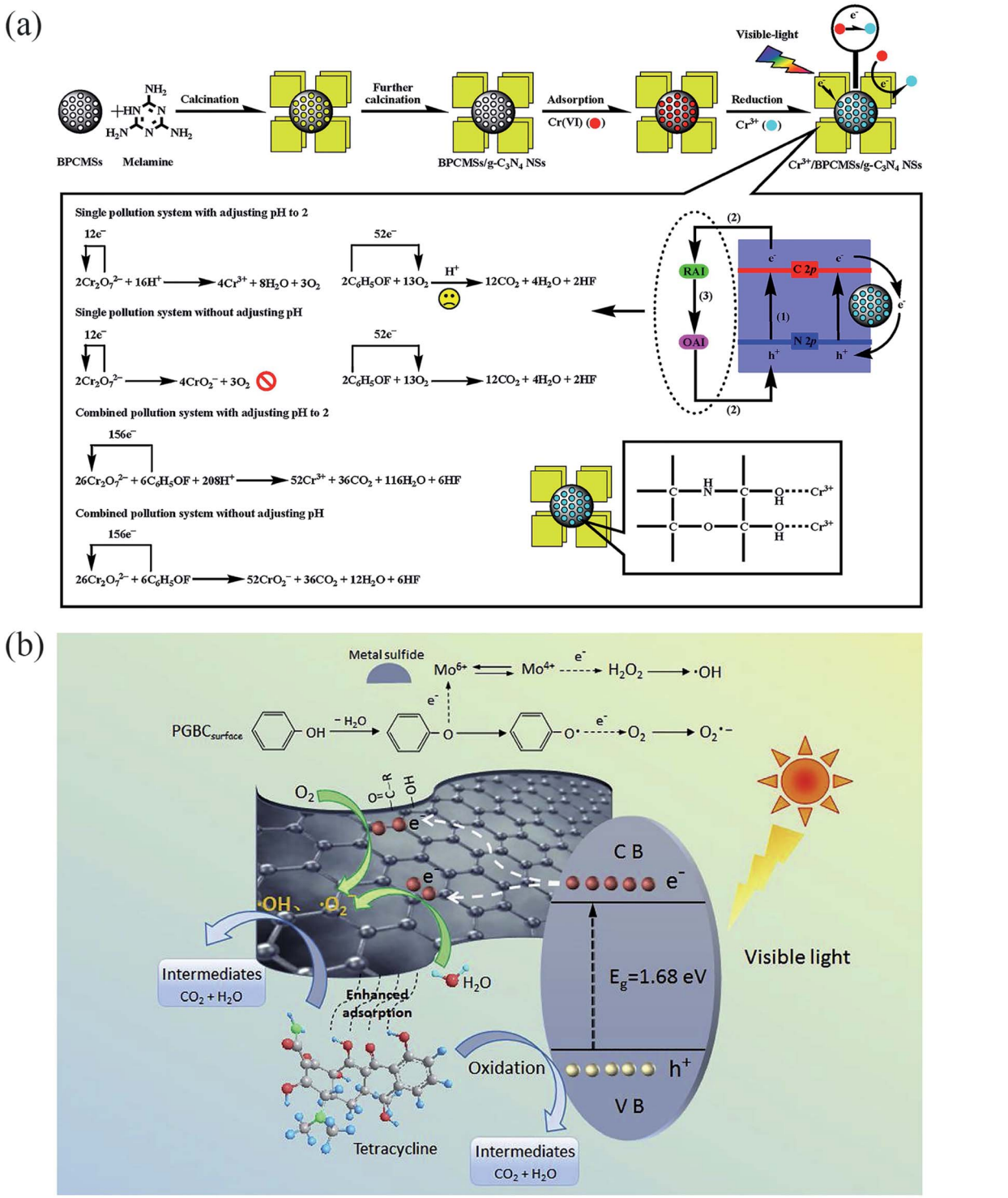

Fig. 18 (a) Schematic for the synthesis of BPCMSs/g-C_3N_4 NSs and recycled Cr^{3+}/BPCMSs/g-C_3N_4 NSs and related reactions of photogenerated electrons. Reprinted with permission from ref. 249. Copyright 2019 Elsevier B. V. (b) The proposed mechanism for the degradation of TC molecules by the g-MoS_2/BPGC nanocomposite. Reprinted with permission from ref. 250. Copyright 2019 Elsevier B. V.

photocatalysts to exhibit a "synergistic benefit" of adsorption and photocatalytic degradation. BPGCs have high electronic conductivity, and the photogenerated electrons generated by the excitation of the photocatalyst can be rapidly transferred through graphitic carbon, inhibiting the recombination of photogenerated electrons and holes and effectively improving the photocatalytic activity. For example, Li *et al.*[249] successfully combined melamine with biomass-derived porous carbon microspheres (BPCMSs) to obtain BPCMS-coupled graphitic carbon nitride nanosheets (BPCMSs/g-C_3N_4 NSs), in which BPCMSs were fabricated by hydrothermal carbonization and KOH activation of *Camellia oleifera* shells (Fig. 18a). Thanks to the synergistic effect of adsorption and photocatalytic reduction, BPCMSs/g-C_3N_4 NSs could substantially remove Cr(VI) or total chromium from an aqueous solution. The photogenerated electrons produced by graphitic carbon nitride nanosheets were mediated to the surface of BPCMSs by the excellent graphitic structure of BPCMSs, so as to reduce the Cr(VI) adsorbed on the surface of BPCMSs. The generated Cr(III) was fixed and recycled through subsequent treatment. The electron conduction ability that resulted from the graphitic structure of BPCMSs reduced the probability of electron–hole recombination.

Ye *et al.*[250] presented a study on the production of BPGCs from straw through a synchronous carbonization and graphitization process, in which potassium ferrate (K_2FeO_4) were employed as the catalyst. Furthermore, a new structure of g-MoS_2/BPGCs was constructed by adding g-MoS_2 into BPGCs, in which BPGCs played the role of supporting and charging media. This facile assembled biomass-based nanocomposite g-MoS_2/BPGCs exhibited considerable removal efficiency towards tetracycline hydrochloride (TC) by a combination of adsorption and photocatalysis under visible light.[250] The porous graphitic carbon as a load was considered to be the charge transporter with good conductivity, which promoted the flow transfer of photogenerated charge carriers and hindered the recombination of electron–hole pairs (Fig. 18b). However, there is still a lot of room to study the combined use of BPGCs and photocatalysts to eliminate pollutants, and the binding mechanism and the optimization of composite properties need to be further studied.

5 Conclusions and prospects

As is known to all, renewable biomass resources with a rich carbon content provide a sufficient raw material basis for the future development and application of carbon materials. Porous graphitic carbon materials derived from biomass have become increasingly attractive materials for addressing severe environmental issues and energy crises. Valuable studies have been conducted to illustrate the synthesis mechanisms and the application of electrochemical energy storage and environmental protection of BPGCs, which are elaborated in this review.

However, it is important to be aware of some of the obstacles to improve BPGC applications, as follows:

(1) Although BPGCs are continuously prepared, their high preparation cost is still an important obstacle hindering their application. Among them, high temperature pyrolysis is an indispensable step, and the dependence on energy is quite high. How to develop a low-energy production process route and reduce costs is an important topic of current research. For example, solar energy can be used to improve high temperature pyrolysis and new high-efficiency activators and self-activation systems can be sought.

(2) Feedstocks with different natural characteristics, production conditions and synthetic parameters can significantly affect the properties of the obtained BPGCs. Therefore, the selection of suitable biomass sources and process methods enables efficient preparation of BPGCs. Screening out suitable biomass sources and corresponding preparation methods to form a complete and systematic method is needed in further research. Future research will require the selection of raw materials with the right ingredients and optimization of production conditions and synthetic parameters to accurately design BPGCs that are tailored to a specific application.

(3) Graphitization of porous carbon materials with other kinds of catalysts or mixed catalysts is also a hot research direction at present. Various methods and processes for preparing BPGCs can be further explored and the effects of different catalysts on the properties of BPGCs can be discussed. For example, for lignocellulosic biomass, BPGCs can be obtained by separation and different treatment of easily graphitizable or highly porous components.

(4) The applications of BPGCs are mainly focused on electrochemical energy storage, and it is necessary to strengthen the application of environmental protection. In addition, many potential applications of BPGCs should be explored in the future. For instance, they may be used as an adsorbent for greenhouse gases, catalysts for the hydrogen evolution reaction (HER) and efficient (photo)catalysts.

(5) In terms of energy applications, the main advantages of BPGCs over porous graphitic carbon materials synthesized from other fine precursors (such as graphene, carbon nanotubes, and ethanol) are their wide availability, low cost, ease of synthesis, and environmental friendliness. When BPGCs were used as electrode materials for supercapacitors, lithium-ion batteries, and fuel cells, their performance is still a bit behind that of porous graphitic carbon materials synthesized from other precursors. It is urgent to improve their performance and to carry out in-depth research on the factors restricting their performance improvement and related mechanisms.

(6) To date, BPGCs have been widely used for supercapacitors and LIBs; however, a few studies were reported for their application in lithium–sulfur batteries and sodium ion batteries. Moreover, some new types of energy storage and conversion systems such as Mg (Al, Mn)-ion batteries have been rarely explored. Considering that BPGCs are mechanically robust with adjustable structures and surface/interface chemistry, they can be readily used as a green material solution for newly emerging energy storage and conversion systems through customized control of their structure and characteristics.

(7) Notwithstanding that biomass raw materials rarely contain heavy metals or other toxic and harmful substances that cause environmental hazards, organic or inorganic pollutants

that may occur in the preparation of BPGCs from biomass and their environmental risks cannot be ignored. In particular, heavy metals contained in biomass raw materials may be concentrated in BPGCs and thus have an impact on their subsequent utilization. To our knowledge, the impact of heavy metal contaminants in BPGCs on their utilization as electrode materials and environmental remediation materials has not been reported, which needs to be emphasized and explored. For heavy metals in BPGCs that may have negative effects, it is necessary to remove them by leaching them with strong acid solution or other agents so as to achieve the desorption and recovery of heavy metals. In addition, it is also a worthwhile method to recover heavy metals by rapid pyrolysis of biomass raw materials.

(8) BPGCs after utilization will inevitably remain in the environment. Because most BPGCs are biocompatible and environmentally friendly, if they can be recycled and reused efficiently, they will undoubtedly form a good green cycle path. Magnetizing BPGCs is one way to achieve recovery, especially in the field of environmental protection. In addition, how to improve the reuse efficiency of BPGCs as electrode materials and environmental restoration materials is also a problem that needs to be paid attention to. It is worth exploring that the reuse of BPGCs can be achieved through simple treatment (such as pyrolysis).

(9) Biomass often has "specificity", and even the same type of biomass may have different properties due to various other factors. How to realize the large-scale replication of BPGCs is still rarely studied. This is also related to the industrial production and large-scale practical application of BPGCs. This requires us to select the biomass raw materials with strong reproducibility and achieve good scalability for their applications through the mature template method.

Hence, exploring an eco-friendly and efficient approach with simplified operation to build high-performance BPGCs materials on a large scale is the ultimate goal in the future.

Conflicts of interest

There are no conflicts to declare.

Acknowledgements

This research was financially supported by the National Natural Science Foundation of China (51521006, 51809089 and 51609268), the Natural Science Foundation of Hunan Province, China (2018JJ3040 and 2018JJ3096), the Research and Development Plan of Key Areas in Hunan Province (2019NK2062) and the Research and Development Project of Changsha Municipal Public Works Bureau, Hunan Province, China (QT201801-QT4).

References

1 F. Wang, X. Wu, X. Yuan, Z. Liu, Y. Zhang, L. Fu, Y. Zhu, Q. Zhou, Y. Wu and W. Huang, *Chem. Soc. Rev.*, 2017, **46**, 6816–6854.
2 T. Kim, W. Song, D.-Y. Son, L. K. Ono and Y. Qi, *J. Mater. Chem. A*, 2019, **7**, 2942–2964.
3 W. T. Mook, M. K. Aroua and G. Issabayeva, *Renewable Sustainable Energy Rev.*, 2014, **38**, 36–46.
4 M.-M. Titirici, R. J. White, N. Brun, V. L. Budarin, D. S. Su, F. del Monte, J. H. Clark and M. J. MacLachlan, *Chem. Soc. Rev.*, 2015, **44**, 250–290.
5 W.-J. Liu, H. Jiang and H.-Q. Yu, *Energy Environ. Sci.*, 2019, **12**, 1751–1779.
6 S. Zhou, L. Zhou, Y. Zhang, J. Sun, J. Wen and Y. Yuan, *J. Mater. Chem. A*, 2019, **7**, 4217–4229.
7 L. Jiang, Y. Liu, S. Liu, G. Zeng, X. Hu, X. Hu, Z. Guo, X. Tan, L. Wang and Z. Wu, *Environ. Sci. Technol.*, 2017, **51**, 6352–6359.
8 X.-f. Tan, Y.-g. Liu, Y.-l. Gu, Y. Xu, G.-m. Zeng, X.-j. Hu, S.-b. Liu, X. Wang, S.-m. Liu and J. Li, *Bioresour. Technol.*, 2016, **212**, 318–333.
9 H.-p. Feng, L. Tang, G.-m. Zeng, J. Tang, Y.-c. Deng, M. Yan, Y.-n. Liu, Y.-y. Zhou, X.-y. Ren and S. Chen, *J. Mater. Chem. A*, 2018, **6**, 7310–7337.
10 Z. Bi, Q. Kong, Y. Cao, G. Sun, F. Su, X. Wei, X. Li, A. Ahmad, L. Xie and C.-M. Chen, *J. Mater. Chem. A*, 2019, **7**, 16028–16045.
11 Z. Zhang, Z. P. Cano, D. Luo, H. Dou, A. Yu and Z. Chen, *J. Mater. Chem. A*, 2019, **7**, 20985–21003.
12 M.-f. Li, Y.-g. Liu, G.-m. Zeng, N. Liu and S.-b. Liu, *Chemosphere*, 2019, **226**, 360–380.
13 K. Lu, Z. Hu, J. Ma, H. Ma, L. Dai and J. Zhang, *Nat. Commun.*, 2017, **8**, 527.
14 J. Zhang, H. Li, P. Guo, H. Ma and X. S. Zhao, *J. Mater. Chem. A*, 2016, **4**, 8497–8511.
15 Y. Luo, Y. Yan, S. Zheng, H. Xue and H. Pang, *J. Mater. Chem. A*, 2019, **7**, 901–924.
16 X. Tan, Y. Liu, G. Zeng, X. Wang, X. Hu, Y. Gu and Z. Yang, *Chemosphere*, 2015, **125**, 70–85.
17 X.-f. Tan, S.-b. Liu, Y.-g. Liu, Y.-l. Gu, G.-m. Zeng, X.-j. Hu, X. Wang, S.-h. Liu and L.-h. Jiang, *Bioresour. Technol.*, 2017, **227**, 359–372.
18 Y. Ding, Y. Liu, S. Liu, X. Huang, Z. Li, X. Tan, G. Zeng and L. Zhou, *Pedosphere*, 2017, **27**, 645–661.
19 C. Zhang, G. Zeng, D. Huang, C. Lai, M. Chen, M. Cheng, W. Tang, L. Tang, H. Dong, B. Huang, X. Tan and R. Wang, *Chem. Eng. J.*, 2019, **373**, 902–922.
20 T. Kan, V. Strezov and T. J. Evans, *Renewable Sustainable Energy Rev.*, 2016, **57**, 1126–1140.
21 A. Demirbaş, *Energy Convers. Manage.*, 2001, **42**, 1357–1378.
22 S. Du, J. A. Valla and G. M. Bollas, *Green Chem.*, 2013, **15**, 3214–3229.
23 B. V. Babu, *Biofuels, Bioprod. Biorefin.*, 2008, **2**, 393–414.
24 S. Wang, G. Dai, H. Yang and Z. Luo, *Prog. Energy Combust. Sci.*, 2017, **62**, 33–86.
25 J. J. Manyà, *Environ. Sci. Technol.*, 2012, **46**, 7939–7954.
26 Z. Wang, D. Shen, C. Wu and S. Gu, *Green Chem.*, 2018, **20**, 5031–5057.
27 H. Ru, N. Bai, K. Xiang, W. Zhou, H. Chen and X. S. Zhao, *Electrochim. Acta*, 2016, **194**, 10–16.

28 A. J. Smith, M. J. MacDonald, L. D. Ellis, M. N. Obrovac and J. R. Dahn, *Carbon*, 2012, **50**, 3717–3723.
29 M. J. Antal and M. Grønli, *Ind. Eng. Chem. Res.*, 2003, **42**, 1619–1640.
30 R.-Z. Wang, D.-L. Huang, Y.-G. Liu, C. Zhang, C. Lai, G.-M. Zeng, M. Cheng, X.-M. Gong, J. Wan and H. Luo, *Bioresour. Technol.*, 2018, **261**, 265–271.
31 L. Zhou, Y. Liu, S. Liu, Y. Yin, G. Zeng, X. Tan, X. Hu, X. Hu, L. Jiang, Y. Ding, S. Liu and X. Huang, *Bioresour. Technol.*, 2016, **218**, 351–359.
32 W.-J. Liu, H. Jiang and H.-Q. Yu, *Chem. Rev.*, 2015, **115**, 12251–12285.
33 O. Fromm, A. Heckmann, U. C. Rodehorst, J. Frerichs, D. Becker, M. Winter and T. Placke, *Carbon*, 2018, **128**, 147–163.
34 J. Yu, L. Tang, Y. Pang, G. Zeng, H. Feng, J. Zou, J. Wang, C. Feng, X. Zhu, X. Ouyang and J. Tan, *Appl. Catal., B*, 2020, **260**, 118160.
35 S. Gao, K. Geng, H. Liu, X. Wei, M. Zhang, P. Wang and J. Wang, *Energy Environ. Sci.*, 2015, **8**, 221–229.
36 L. Jiang, L. Sheng and Z. Fan, *Sci. China Mater.*, 2018, **61**, 133–158.
37 M. Sevilla and R. Mokaya, *Energy Environ. Sci.*, 2014, **7**, 1250–1280.
38 M. Danish and T. Ahmad, *Renewable Sustainable Energy Rev.*, 2018, **87**, 1–21.
39 J. Wang and S. Kaskel, *J. Mater. Chem.*, 2012, **22**, 23710–23725.
40 Y. Huang, E. Ma and G. Zhao, *Ind. Crops Prod.*, 2015, **69**, 447–455.
41 T. Otowa, R. Tanibata and M. Itoh, *Gas Sep. Purif.*, 1993, **7**, 241–245.
42 D. Lozano-Castelló, J. M. Calo, D. Cazorla-Amorós and A. Linares-Solano, *Carbon*, 2007, **45**, 2529–2536.
43 E. Raymundo-Piñero, P. Azaïs, T. Cacciaguerra, D. Cazorla-Amorós, A. Linares-Solano and F. Béguin, *Carbon*, 2005, **43**, 786–795.
44 J. Romanos, M. Beckner, T. Rash, L. Firlej, B. Kuchta, P. Yu, G. Suppes, C. Wexler and P. Pfeifer, *Nanotechnology*, 2011, **23**, 015401.
45 A. Zubrik, M. Matik, S. Hredzák, M. Lovás, Z. Danková, M. Kováčová and J. Briančin, *J. Cleaner Prod.*, 2017, **143**, 643–653.
46 T. Wang, Y. Zhai, Y. Zhu, C. Li and G. Zeng, *Renewable Sustainable Energy Rev.*, 2018, **90**, 223–247.
47 M. Song, Y. Zhou, X. Ren, J. Wan, Y. Du, G. Wu and F. Ma, *J. Colloid Interface Sci.*, 2019, **535**, 276–286.
48 L. Xing, X. Chen, Z. Tan, M. Chi, W. Xie, J. Huang, Y. Liang, M. Zheng, H. Hu, H. Dong, Y. Liu and Y. Xiao, *ACS Sustainable Chem. Eng.*, 2019, **7**, 6601–6610.
49 J. Han, J. H. Kwon, J.-W. Lee, J. H. Lee and K. C. Roh, *Carbon*, 2017, **118**, 431–437.
50 S. Sankar, A. T. A. Ahmed, A. I. Inamdar, H. Im, Y. B. Im, Y. Lee, D. Y. Kim and S. Lee, *Mater. Des.*, 2019, **169**, 107688.
51 Q. Zhang, K. Han, S. Li, M. Li, J. Li and K. Ren, *Nanoscale*, 2018, **10**, 2427–2437.
52 G. Yuan, Y. Liang, H. Hu, H. Li, Y. Xiao, H. Dong, Y. Liu and M. Zheng, *ACS Appl. Mater. Interfaces*, 2019, **11**, 26946–26955.
53 X. Chen, M. Chi, L. Xing, X. Xie, S. Liu, Y. Liang, M. Zheng, H. Hu, H. Dong, Y. Liu, S. P. Jiang and Y. Xiao, *ACS Sustainable Chem. Eng.*, 2019, **7**, 5845–5855.
54 S. Song, F. Ma, G. Wu, D. Ma, W. Geng and J. Wan, *J. Mater. Chem. A*, 2015, **3**, 18154–18162.
55 M. Li, H. Xiao, T. Zhang, Q. Li and Y. Zhao, *ACS Sustainable Chem. Eng.*, 2019, **7**, 4716–4723.
56 W. Ma, N. Wang, Y. Du, P. Xu, B. Sun, L. Zhang and K.-Y. A. Lin, *ACS Sustainable Chem. Eng.*, 2019, **7**, 2718–2727.
57 C. Chen, T. Ma, Y. Shang, B. Gao, B. Jin, H. Dan, Q. Li, Q. Yue, Y. Li, Y. Wang and X. Xu, *Appl. Catal., B*, 2019, **250**, 382–395.
58 K. Huang, S.-H. Chai, R. T. Mayes, G. M. Veith, K. L. Browning, M. A. Sakwa-Novak, M. E. Potter, C. W. Jones, Y.-T. Wu and S. Dai, *Chem. Commun.*, 2015, **51**, 17261–17264.
59 K. Huang, S.-H. Chai, R. T. Mayes, S. Tan, C. W. Jones and S. Dai, *Microporous Mesoporous Mater.*, 2016, **230**, 100–108.
60 Y. Zhang, L. Liu, P. Zhang, J. Wang, M. Xu, Q. Deng, Z. Zeng and S. Deng, *Chem. Eng. J.*, 2019, **355**, 309–319.
61 Y. Li, S. Liu, Y. Liang, Y. Xiao, H. Dong, M. Zheng, H. Hu and Y. Liu, *ACS Sustainable Chem. Eng.*, 2019, **7**, 13827–13835.
62 G. Yuan, W. Huang, K. Guan, H. Li, Y. Xie, Y. Liang, Y. Liu and M. Zheng, *J. Mater. Chem. A*, 2019, **7**, 26469–26478.
63 H. Hou, X. Qiu, W. Wei, Y. Zhang and X. Ji, *Adv. Energy Mater.*, 2017, **7**, 1602898.
64 J. Tu, J. Wang, S. Li, W.-L. Song, M. Wang, H. Zhu and S. Jiao, *Nanoscale*, 2019, **11**, 12537–12546.
65 Y. Zhai, Y. Dou, D. Zhao, P. F. Fulvio, R. T. Mayes and S. Dai, *Adv. Mater.*, 2011, **23**, 4828–4850.
66 W. Luo, J. Schardt, C. Bommier, B. Wang, J. Razink, J. Simonsen and X. Ji, *J. Mater. Chem. A*, 2013, **1**, 10662–10666.
67 K.-l. Hong, L. Qie, R. Zeng, Z.-q. Yi, W. Zhang, D. Wang, W. Yin, C. Wu, Q.-j. Fan, W.-x. Zhang and Y.-h. Huang, *J. Mater. Chem. A*, 2014, **2**, 12733–12738.
68 A. B. Fuertes and S. Alvarez, *Carbon*, 2004, **42**, 3049–3055.
69 E. Thompson, A. E. Danks, L. Bourgeois and Z. Schnepp, *Green Chem.*, 2015, **17**, 551–556.
70 C. J. Thambiliyagodage, S. Ulrich, P. T. Araujo and M. G. Bakker, *Carbon*, 2018, **134**, 452–463.
71 A. Ōya and S. Ōtani, *Carbon*, 1981, **19**, 391–400.
72 M. Sevilla and A. B. Fuertes, *Carbon*, 2006, **44**, 468–474.
73 A. Ōya and H. Marsh, *J. Mater. Sci.*, 1982, **17**, 309–322.
74 M. Sevilla, C. Sanchís, T. Valdés-Solís, E. Morallón and A. B. Fuertes, *J. Phys. Chem. C*, 2007, **111**, 9749–9756.
75 A. Baçaoui, A. Yaacoubi, A. Dahbi, C. Bennouna, R. Phan Tan Luu, F. J. Maldonado-Hodar, J. Rivera-Utrilla and C. Moreno-Castilla, *Carbon*, 2001, **39**, 425–432.
76 Z. Xu, D. Cai, Z. Hu, F. Wang and L. Gan, *Electrochim. Acta*, 2014, **117**, 486–491.
77 A. Ōya and S. Ōtani, *Carbon*, 1979, **17**, 131–137.

78 A.-H. Lu, W.-C. Li, E.-L. Salabas, B. Spliethoff and F. Schüth, *Chem. Mater.*, 2006, **18**, 2086–2094.
79 A. Ōya and H. Marsh, *J. Mater. Sci.*, 1982, **17**, 309–322.
80 F. J. Derbyshire, A. E. B. Presland and D. L. Trimm, *Carbon*, 1975, **13**, 111–113.
81 Y. Liu, Q. Liu, J. Gu, D. Kang, F. Zhou, W. Zhang, Y. Wu and D. Zhang, *Carbon*, 2013, **64**, 132–140.
82 B. Chang, Y. Guo, Y. Li, H. Yin, S. Zhang, B. Yang and X. Dong, *J. Mater. Chem. A*, 2015, **3**, 9565–9577.
83 M. Zhao and H. Song, *J. Mater. Sci. Technol.*, 2011, **27**, 266–270.
84 Q. Liu, J. Gu, W. Zhang, Y. Miyamoto, Z. Chen and D. Zhang, *J. Mater. Chem.*, 2012, **22**, 21183–21188.
85 A. Gutiérrez-Pardo, J. Ramírez-Rico, R. Cabezas-Rodríguez and J. Martínez-Fernández, *J. Power Sources*, 2015, **278**, 18–26.
86 F. Wu, R. Huang, D. Mu, B. Wu and Y. Chen, *Electrochim. Acta*, 2016, **187**, 508–516.
87 C. Wang, D. Ma and X. Bao, *J. Phys. Chem. C*, 2008, **112**, 17596–17602.
88 Z. Qiao, S. Hwang, X. Li, C. Wang, W. Samarakoon, S. Karakalos, D. Li, M. Chen, Y. He, M. Wang, Z. Liu, G. Wang, H. Zhou, Z. Feng, D. Su, J. S. Spendelow and G. Wu, *Energy Environ. Sci.*, 2019, **12**, 2830–2841.
89 C. Chang, H. Wang, Y. Zhang, S. Wang, X. Liu and L. Li, *ACS Sustainable Chem. Eng.*, 2019, **7**, 10763–10772.
90 S. Yang, S. Wang, X. Liu and L. Li, *Carbon*, 2019, **147**, 540–549.
91 L. Sun, C. Tian, M. Li, X. Meng, L. Wang, R. Wang, J. Yin and H. Fu, *J. Mater. Chem. A*, 2013, **1**, 6462–6470.
92 L. Wan, W. Wei, M. Xie, Y. Zhang, X. Li, R. Xiao, J. Chen and C. Du, *Electrochim. Acta*, 2019, **311**, 72–82.
93 H. Jin, J. Hu, S. Wu, X. Wang, H. Zhang, H. Xu and K. Lian, *J. Power Sources*, 2018, **384**, 270–277.
94 Y. Cai, Y. Luo, H. Dong, X. Zhao, Y. Xiao, Y. Liang, H. Hu, Y. Liu and M. Zheng, *J. Power Sources*, 2017, **353**, 260–269.
95 Y. Gong, D. Li, C. Luo, Q. Fu and C. Pan, *Green Chem.*, 2017, **19**, 4132–4140.
96 Y. Shen, *J. Mater. Chem. A*, 2015, **3**, 13114–13188.
97 W.-J. Liu, K. Tian, Y.-R. He, H. Jiang and H.-Q. Yu, *Environ. Sci. Technol.*, 2014, **48**, 13951–13959.
98 J. Xia, N. Zhang, S. Chong, D. Li, Y. Chen and C. Sun, *Green Chem.*, 2018, **20**, 694–700.
99 J. i. Hayashi, T. Horikawa, I. Takeda, K. Muroyama and F. Nasir Ani, *Carbon*, 2002, **40**, 2381–2386.
100 J. i. Hayashi, A. Kazehaya, K. Muroyama and A. P. Watkinson, *Carbon*, 2000, **38**, 1873–1878.
101 J. Niu, R. Shao, M. Liu, Y. Zan, M. Dou, J. Liu, Z. Zhang, Y. Huang and F. Wang, *Adv. Funct. Mater.*, 2019, **29**, 1905095.
102 X. Li, B. Y. Guan, S. Gao and X. W. Lou, *Energy Environ. Sci.*, 2019, **12**, 648–655.
103 M. Salanne, B. Rotenberg, K. Naoi, K. Kaneko, P. L. Taberna, C. P. Grey, B. Dunn and P. Simon, *Nat. Energy*, 2016, **1**, 16070.
104 P. Simon and Y. Gogotsi, *Nat. Mater.*, 2008, **7**, 845.
105 S. Zhang and N. Pan, *Adv. Energy Mater.*, 2015, **5**, 1401401.
106 H. Jiang, L. Yang, C. Li, C. Yan, P. S. Lee and J. Ma, *Energy Environ. Sci.*, 2011, **4**, 1813–1819.
107 G. Wang, L. Zhang and J. Zhang, *Chem. Soc. Rev.*, 2012, **41**, 797–828.
108 Y. Wang, Y. Song and Y. Xia, *Chem. Soc. Rev.*, 2016, **45**, 5925–5950.
109 N.-S. Choi, Z. Chen, S. A. Freunberger, X. Ji, Y.-K. Sun, K. Amine, G. Yushin, L. F. Nazar, J. Cho and P. G. Bruce, *Angew. Chem., Int. Ed.*, 2012, **51**, 9994–10024.
110 Y. Liu, Z. Xiao, Y. Liu and L.-Z. Fan, *J. Mater. Chem. A*, 2018, **6**, 160–166.
111 X. Lu, M. Yu, G. Wang, Y. Tong and Y. Li, *Energy Environ. Sci.*, 2014, **7**, 2160–2181.
112 W. Qian, F. Sun, Y. Xu, L. Qiu, C. Liu, S. Wang and F. Yan, *Energy Environ. Sci.*, 2014, **7**, 379–386.
113 A. Eftekhari, *J. Mater. Chem. A*, 2018, **6**, 2866–2876.
114 P. Sharma and T. S. Bhatti, *Energy Convers. Manage.*, 2010, **51**, 2901–2912.
115 Y. Gogotsi and P. Simon, *Science*, 2011, **334**, 917.
116 J. Lee, J. Kim and T. Hyeon, *Adv. Mater.*, 2006, **18**, 2073–2094.
117 Y. Shao, M. F. El-Kady, J. Sun, Y. Li, Q. Zhang, M. Zhu, H. Wang, B. Dunn and R. B. Kaner, *Chem. Rev.*, 2018, **118**, 9233–9280.
118 C. Zhong, Y. Deng, W. Hu, J. Qiao, L. Zhang and J. Zhang, *Chem. Soc. Rev.*, 2015, **44**, 7484–7539.
119 J. Yan, Q. Wang, T. Wei and Z. Fan, *Adv. Energy Mater.*, 2014, **4**, 1300816.
120 X. Chen, R. Paul and L. Dai, *Natl. Sci. Rev.*, 2017, **4**, 453–489.
121 A. Borenstein, O. Hanna, R. Attias, S. Luski, T. Brousse and D. Aurbach, *J. Mater. Chem. A*, 2017, **5**, 12653–12672.
122 M. Zhou, J. Catanach, J. Gomez, S. Richins and S. Deng, *ACS Appl. Mater. Interfaces*, 2017, **9**, 4362–4373.
123 T. Liu, F. Zhang, Y. Song and Y. Li, *J. Mater. Chem. A*, 2017, **5**, 17705–17733.
124 X.-Y. Yang, L.-H. Chen, Y. Li, J. C. Rooke, C. Sanchez and B.-L. Su, *Chem. Soc. Rev.*, 2017, **46**, 481–558.
125 L. Qie, W. Chen, H. Xu, X. Xiong, Y. Jiang, F. Zou, X. Hu, Y. Xin, Z. Zhang and Y. Huang, *Energy Environ. Sci.*, 2013, **6**, 2497–2504.
126 P. Hao, Z. Zhao, J. Tian, H. Li, Y. Sang, G. Yu, H. Cai, H. Liu, C. P. Wong and A. Umar, *Nanoscale*, 2014, **6**, 12120–12129.
127 M.-H. Sun, S.-Z. Huang, L.-H. Chen, Y. Li, X.-Y. Yang, Z.-Y. Yuan and B.-L. Su, *Chem. Soc. Rev.*, 2016, **45**, 3479–3563.
128 H. Sun, J. Zhu, D. Baumann, L. Peng, Y. Xu, I. Shakir, Y. Huang and X. Duan, *Nat. Rev. Mater.*, 2019, **4**, 45–60.
129 Z. Yu, L. Tetard, L. Zhai and J. Thomas, *Energy Environ. Sci.*, 2015, **8**, 702–730.
130 Z. Sun, M. Zheng, H. Hu, H. Dong, Y. Liang, Y. Xiao, B. Lei and Y. Liu, *Chem. Eng. J.*, 2018, **336**, 550–561.
131 L. Peng, Y. Cai, Y. Luo, G. Yuan, J. Huang, C. Hu, H. Dong, Y. Xiao, Y. Liang, Y. Liu and M. Zheng, *ACS Sustainable Chem. Eng.*, 2018, **6**, 12716–12726.
132 L. Hao, X. Li and L. Zhi, *Adv. Mater.*, 2013, **25**, 3899–3904.
133 J. P. Paraknowitsch and A. Thomas, *Energy Environ. Sci.*, 2013, **6**, 2839–2855.

134 G. Hasegawa, T. Deguchi, K. Kanamori, Y. Kobayashi, H. Kageyama, T. Abe and K. Nakanishi, *Chem. Mater.*, 2015, **27**, 4703–4712.
135 M. R. Benzigar, S. N. Talapaneni, S. Joseph, K. Ramadass, G. Singh, J. Scaranto, U. Ravon, K. Al-Bahily and A. Vinu, *Chem. Soc. Rev.*, 2018, **47**, 2680–2721.
136 Q. Shi, R. Zhang, Y. Lv, Y. Deng, A. A. Elzatahrya and D. Zhao, *Carbon*, 2015, **84**, 335–346.
137 J. Zhu, J. Yang, R. Miao, Z. Yao, X. Zhuang and X. Feng, *J. Mater. Chem. A*, 2016, **4**, 2286–2292.
138 K. Wang, N. Zhao, S. Lei, R. Yan, X. Tian, J. Wang, Y. Song, D. Xu, Q. Guo and L. Liu, *Electrochim. Acta*, 2015, **166**, 1–11.
139 D. Qiu, N. Guo, A. Gao, L. Zheng, W. Xu, M. Li, F. Wang and R. Yang, *Electrochim. Acta*, 2019, **294**, 398–405.
140 C. Chang, M. Li, H. Wang, S. Wang, X. Liu, H. Liu and L. Li, *J. Mater. Chem. A*, 2019, **7**, 19939–19949.
141 D. Andre, S.-J. Kim, P. Lamp, S. F. Lux, F. Maglia, O. Paschos and B. Stiaszny, *J. Mater. Chem. A*, 2015, **3**, 6709–6732.
142 D. Larcher and J. M. Tarascon, *Nat. Chem.*, 2014, **7**, 19.
143 M. Winter, B. Barnett and K. Xu, *Chem. Rev.*, 2018, **118**, 11433–11456.
144 M. Li, J. Lu, Z. Chen and K. Amine, *Adv. Mater.*, 2018, **30**, 1800561.
145 B. Scrosati, J. Hassoun and Y.-K. Sun, *Energy Environ. Sci.*, 2011, **4**, 3287–3295.
146 Z. Liu, Q. Yu, Y. Zhao, R. He, M. Xu, S. Feng, S. Li, L. Zhou and L. Mai, *Chem. Soc. Rev.*, 2019, **48**, 285–309.
147 M. Armand and J. M. Tarascon, *Nature*, 2008, **451**, 652–657.
148 J. M. Tarascon and M. Armand, *Nature*, 2001, **414**, 359–367.
149 H. Zhang, H. Zhao, M. A. Khan, W. Zou, J. Xu, L. Zhang and J. Zhang, *J. Mater. Chem. A*, 2018, **6**, 20564–20620.
150 Y. Hu and X. Sun, *J. Mater. Chem. A*, 2014, **2**, 10712–10738.
151 R. Yazami and P. Touzain, *J. Power Sources*, 1983, **9**, 365–371.
152 J.-G. Wang, D. Jin, H. Liu, C. Zhang, R. Zhou, C. Shen, K. Xie and B. Wei, *Nano Energy*, 2016, **22**, 524–532.
153 Y. Xia, Z. Xiao, X. Dou, H. Huang, X. Lu, R. Yan, Y. Gan, W. Zhu, J. Tu, W. Zhang and X. Tao, *ACS Nano*, 2013, **7**, 7083–7092.
154 X. Zhou, F. Chen, T. Bai, B. Long, Q. Liao, Y. Ren and J. Yang, *Green Chem.*, 2016, **18**, 2078–2088.
155 A. Magasinski, P. Dixon, B. Hertzberg, A. Kvit, J. Ayala and G. Yushin, *Nat. Mater.*, 2010, **9**, 353–358.
156 J. Liu, P. Kopold, P. A. van Aken, J. Maier and Y. Yu, *Angew. Chem., Int. Ed.*, 2015, **54**, 9632–9636.
157 C. Wang, H. Wu, Z. Chen, M. T. McDowell, Y. Cui and Z. Bao, *Nat. Chem.*, 2013, **5**, 1042.
158 D. Lin, Z. Lu, P.-C. Hsu, H. R. Lee, N. Liu, J. Zhao, H. Wang, C. Liu and Y. Cui, *Energy Environ. Sci.*, 2015, **8**, 2371–2376.
159 M. Pasta, C. D. Wessells, R. A. Huggins and Y. Cui, *Nat. Commun.*, 2012, **3**, 1149.
160 D. Song, J. Park, K. Kim, L. S. Lee, J. Y. Seo, Y.-K. Oh, Y.-J. Kim, M.-H. Ryou, Y. M. Lee and K. Lee, *Electrochim. Acta*, 2017, **250**, 59–67.
161 Y. Son, J. Sung, Y. Son and J. Cho, *Curr. Opin. Electrochem.*, 2017, **6**, 77–83.
162 S. Liu, J. Feng, X. Bian, Y. Qian, J. Liu and H. Xu, *Nano Energy*, 2015, **13**, 651–657.
163 L. Wang, X. He, J. Li, W. Sun, J. Gao, J. Guo and C. Jiang, *Angew. Chem., Int. Ed.*, 2012, **51**, 9034–9037.
164 P. V. Prikhodchenko, J. Gun, S. Sladkevich, A. A. Mikhaylov, O. Lev, Y. Y. Tay, S. K. Batabyal and D. Y. W. Yu, *Chem. Mater.*, 2012, **24**, 4750–4757.
165 Y. Huang, Z. Lin, M. Zheng, T. Wang, J. Yang, F. Yuan, X. Lu, L. Liu and D. Sun, *J. Power Sources*, 2016, **307**, 649–656.
166 J. Zang, J. Ye, H. Qian, Y. Lin, X. Zhang, M. Zheng and Q. Dong, *Electrochim. Acta*, 2018, **260**, 783–788.
167 A. Eftekhari, *Energy Storage Materials*, 2017, **7**, 157–180.
168 T. Yuan, Y. Jiang, W. Sun, B. Xiang, Y. Li, M. Yan, B. Xu and S. Dou, *Adv. Funct. Mater.*, 2016, **26**, 2198–2206.
169 P. L. Taberna, S. Mitra, P. Poizot, P. Simon and J. M. Tarascon, *Nat. Mater.*, 2006, **5**, 567–573.
170 Z. Cai, L. Xu, M. Yan, C. Han, L. He, K. M. Hercule, C. Niu, Z. Yuan, W. Xu, L. Qu, K. Zhao and L. Mai, *Nano Lett.*, 2015, **15**, 738–744.
171 B. Lee, Y. Ko, G. Kwon, S. Lee, K. Ku, J. Kim and K. Kang, *Joule*, 2018, **2**, 61–75.
172 J. Hou, C. Cao, F. Idrees and X. Ma, *ACS Nano*, 2015, **9**, 2556–2564.
173 G. Yuan, H. Li, H. Hu, Y. Xie, Y. Xiao, H. Dong, Y. Liang, Y. Liu and M. Zheng, *Electrochim. Acta*, 2019, **326**, 134974.
174 J. Zhu, S. Liu, Y. Liu, T. Meng, L. Ma, H. Zhang, M. Kuang and J. Jiang, *ACS Sustainable Chem. Eng.*, 2018, **6**, 13662–13669.
175 E. D. Wachsman and K. T. Lee, *Science*, 2011, **334**, 935–939.
176 O. Z. Sharaf and M. F. Orhan, *Renewable Sustainable Energy Rev.*, 2014, **32**, 810–853.
177 M. Winter and R. J. Brodd, *Chem. Rev.*, 2004, **104**, 4245–4270.
178 H. S. Wroblowa, P. Yen Chi and G. Razumney, *J. Electroanal. Chem. Interfacial Electrochem.*, 1976, **69**, 195–201.
179 S. Sui, X. Wang, X. Zhou, Y. Su, S. Riffat and C.-j. Liu, *J. Mater. Chem. A*, 2017, **5**, 1808–1825.
180 L. Yang, J. Shui, L. Du, Y. Shao, J. Liu, L. Dai and Z. Hu, *Adv. Mater.*, 2019, **31**, 1804799.
181 G. Wu, K. L. More, C. M. Johnston and P. Zelenay, *Science*, 2011, **332**, 443–447.
182 C. Zhu, H. Li, S. Fu, D. Du and Y. Lin, *Chem. Soc. Rev.*, 2016, **45**, 517–531.
183 L. Dai, Y. Xue, L. Qu, H.-J. Choi and J.-B. Baek, *Chem. Rev.*, 2015, **115**, 4823–4892.
184 J. Deng, M. Li and Y. Wang, *Green Chem.*, 2016, **18**, 4824–4854.
185 N. Daems, X. Sheng, I. F. J. Vankelecom and P. P. Pescarmona, *J. Mater. Chem. A*, 2014, **2**, 4085–4110.
186 H. Wang, T. Maiyalagan and X. Wang, *ACS Catal.*, 2012, **2**, 781–794.
187 K. Gong, F. Du, Z. Xia, M. Durstock and L. Dai, *Science*, 2009, **323**, 760–764.
188 K. Chatterjee, M. Ashokkumar, H. Gullapalli, Y. Gong, R. Vajtai, P. Thanikaivelan and P. M. Ajayan, *Carbon*, 2018, **130**, 645–651.

189 D. He, W. Zhao, P. Li, Z. Liu, H. Wu, L. Liu, K. Han, L. Liu, Q. Wan, F. K. Butt and X. Qu, *Appl. Surf. Sci.*, 2019, **465**, 303–312.
190 C. Tang, H.-F. Wang, X. Chen, B.-Q. Li, T.-Z. Hou, B. Zhang, Q. Zhang, M.-M. Titirici and F. Wei, *Adv. Mater.*, 2016, **28**, 6845–6851.
191 P. Kaur, G. Verma and S. S. Sekhon, *Prog. Mater. Sci.*, 2019, **102**, 1–71.
192 L. Liu, G. Zeng, J. Chen, L. Bi, L. Dai and Z. Wen, *Nano Energy*, 2018, **49**, 393–402.
193 L. Xu, H. Fan, L. Huang, J. Xia, S. Li, M. Li, H. Ding and K. Huang, *Electrochim. Acta*, 2017, **239**, 1–9.
194 S. Gao, X. Wei, H. Liu, K. Geng, H. Wang, H. Moehwald and D. Shchukin, *J. Mater. Chem. A*, 2015, **3**, 23376–23384.
195 S. Gao, L. Li, K. Geng, X. Wei and S. Zhang, *Nano Energy*, 2015, **16**, 408–418.
196 S. Gao, X. Li, L. Li and X. Wei, *Nano Energy*, 2017, **33**, 334–342.
197 C. Guo, R. Hu, W. Liao, Z. Li, L. Sun, D. Shi, Y. Li and C. Chen, *Electrochim. Acta*, 2017, **236**, 228–238.
198 C. Zhu, D. Du, A. Eychmüller and Y. Lin, *Chem. Rev.*, 2015, **115**, 8896–8943.
199 Y. Zhao, X. Li, X. Jia and S. Gao, *Nano Energy*, 2019, **58**, 384–391.
200 H. T. Chung, D. A. Cullen, D. Higgins, B. T. Sneed, E. F. Holby, K. L. More and P. Zelenay, *Science*, 2017, **357**, 479–484.
201 M. Li, Y. Xiong, X. Liu, C. Han, Y. Zhang, X. Bo and L. Guo, *J. Mater. Chem. A*, 2015, **3**, 9658–9667.
202 D. Wu, C. Zhu, Y. Shi, H. Jing, J. Hu, X. Song, D. Si, S. Liang and C. Hao, *ACS Sustainable Chem. Eng.*, 2019, **7**, 1137–1145.
203 G. Wang, J. Li, M. Liu, L. Du and S. Liao, *ACS Appl. Mater. Interfaces*, 2018, **10**, 32133–32141.
204 P. Zhang, S. Liu, X. Tan, Y. Liu, G. Zeng, Z. Yin, S. Ye and Z. Zeng, *Process Saf. Environ. Prot.*, 2019, **128**, 329–341.
205 S. Zhang, M. Zeng, J. Li, J. Li, J. Xu and X. Wang, *J. Mater. Chem. A*, 2014, **2**, 4391–4397.
206 S. Ye, G. Zeng, H. Wu, J. Liang, C. Zhang, J. Dai, W. Xiong, B. Song, S. Wu and J. Yu, *Resour., Conserv. Recycl.*, 2019, **140**, 278–285.
207 S.-j. Liu, Y.-g. Liu, X.-f. Tan, S.-b. Liu, M.-f. Li, N. Liu, Z.-h. Yin, S.-r. Tian and Y.-h. Zhou, *J. Chem. Technol. Biotechnol.*, 2019, **94**, 2187–2197.
208 Z.-w. Zeng, X.-f. Tan, Y.-g. Liu, S.-r. Tian, G.-m. Zeng, L.-h. Jiang, S.-b. Liu, J. Li, N. Liu and Z.-h. Yin, *Front. Chem.*, 2018, **6**, 80.
209 Z. Liu, F. Zhang, T. Liu, N. Peng and C. Gai, *J. Environ. Manage.*, 2016, **182**, 446–454.
210 K. Gupta, D. Gupta and O. P. Khatri, *Appl. Surf. Sci.*, 2019, **476**, 647–657.
211 X. Xiao, B. Chen, L. Zhu and J. L. Schnoor, *Environ. Sci. Technol.*, 2017, **51**, 12644–12652.
212 D. Zhong, Y. Zhang, L. Wang, J. Chen, Y. Jiang, D. C. W. Tsang, Z. Zhao, S. Ren, Z. Liu and J. C. Crittenden, *Environ. Pollut.*, 2018, **243**, 1302–1309.
213 Y. Chen, X. Zhang, W. Chen, H. Yang and H. Chen, *Bioresour. Technol.*, 2017, **246**, 101–109.
214 X. Zhu, Y. Liu, F. Qian, C. Zhou, S. Zhang and J. Chen, *Bioresour. Technol.*, 2014, **154**, 209–214.
215 S. Chen, Y. Huang, X. Han, Z. Wu, C. Lai, J. Wang, Q. Deng, Z. Zeng and S. Deng, *Chem. Eng. J.*, 2018, **352**, 306–315.
216 K. S. Novoselov, A. K. Geim, S. V. Morozov, D. Jiang, Y. Zhang, S. V. Dubonos, I. V. Grigorieva and A. A. Firsov, *Science*, 2004, **306**, 666–669.
217 E. Stolyarova, K. T. Rim, S. Ryu, J. Maultzsch, P. Kim, L. E. Brus, T. F. Heinz, M. S. Hybertsen and G. W. Flynn, *Proc. Natl. Acad. Sci. U. S. A.*, 2007, **104**, 9209–9212.
218 K. C. Kemp, H. Seema, M. Saleh, N. H. Le, K. Mahesh, V. Chandra and K. S. Kim, *Nanoscale*, 2013, **5**, 3149–3171.
219 J. Wang, Z. Chen and B. Chen, *Environ. Sci. Technol.*, 2014, **48**, 4817–4825.
220 G. Zhao, L. Jiang, Y. He, J. Li, H. Dong, X. Wang and W. Hu, *Adv. Mater.*, 2011, **23**, 3959–3963.
221 S. Chen, J. Wang, Z. Wu, Q. Deng, W. Tu, G. Dai, Z. Zeng and S. Deng, *J. Colloid Interface Sci.*, 2018, **523**, 110–120.
222 P. Zhang, X. Wen, L. Wang, Y. Zhong, Y. Su, Y. Zhang, J. Wang, J. Yang, Z. Zeng and S. Deng, *Chem. Eng. J.*, 2020, **381**, 122731.
223 J. Zhang, P. Zhang, M. Li, Z. Shan, J. Wang, Q. Deng, Z. Zeng and S. Deng, *Ind. Eng. Chem. Res.*, 2019, **58**, 14929–14937.
224 F. Yang, J. Wang, L. Liu, P. Zhang, W. Yu, Q. Deng, Z. Zeng and S. Deng, *ACS Sustainable Chem. Eng.*, 2018, **6**, 15550–15559.
225 J. Wang, P. Zhang, L. Liu, Y. Zhang, J. Yang, Z. Zeng and S. Deng, *Chem. Eng. J.*, 2018, **348**, 57–66.
226 B. Yuan, J. Wang, Y. Chen, X. Wu, H. Luo and S. Deng, *J. Mater. Chem. A*, 2016, **4**, 2263–2276.
227 Y. Guo, Z. Zeng, Y. Liu, Z. Huang, Y. Cui and J. Yang, *J. Mater. Chem. A*, 2018, **6**, 4055–4067.
228 B.-C. Huang, J. Jiang, G.-X. Huang and H.-Q. Yu, *J. Mater. Chem. A*, 2018, **6**, 8978–8985.
229 W.-D. Oh and T.-T. Lim, *Chem. Eng. J.*, 2019, **358**, 110–133.
230 H. Sun, X. Yang, L. Zhao, T. Xu and J. Lian, *J. Mater. Chem. A*, 2016, **4**, 9455–9465.
231 L. Tang, Y. Liu, J. Wang, G. Zeng, Y. Deng, H. Dong, H. Feng, J. Wang and B. Peng, *Appl. Catal., B*, 2018, **231**, 1–10.
232 X. Duan, H. Sun and S. Wang, *Acc. Chem. Res.*, 2018, **51**, 678–687.
233 Q. Zhao, Q. Mao, Y. Zhou, J. Wei, X. Liu, J. Yang, L. Luo, J. Zhang, H. Chen, H. Chen and L. Tang, *Chemosphere*, 2017, **189**, 224–238.
234 X. Duan, Z. Ao, L. Zhou, H. Sun, G. Wang and S. Wang, *Appl. Catal., B*, 2016, **188**, 98–105.
235 R.-Z. Wang, D.-L. Huang, Y.-G. Liu, C. Zhang, C. Lai, X. Wang, G.-M. Zeng, X.-M. Gong, A. Duan, Q. Zhang and P. Xu, *Chem. Eng. J.*, 2019, **371**, 380–403.
236 Y.-n. Zhang, Q. Niu, X. Gu, N. Yang and G. Zhao, *Nanoscale*, 2019, **11**, 11992–12014.
237 M. M. Khin, A. S. Nair, V. J. Babu, R. Murugan and S. Ramakrishna, *Energy Environ. Sci.*, 2012, **5**, 8075–8109.

238 H. Yi, D. Huang, L. Qin, G. Zeng, C. Lai, M. Cheng, S. Ye, B. Song, X. Ren and X. Guo, *Appl. Catal., B*, 2018, **239**, 408–424.
239 F. Perreault, A. Fonseca de Faria and M. Elimelech, *Chem. Soc. Rev.*, 2015, **44**, 5861–5896.
240 P. Zhang, X. Tan, S. Liu, Y. Liu, G. Zeng, S. Ye, Z. Yin, X. Hu and N. Liu, *Chem. Eng. J.*, 2019, **378**, 122141.
241 H. Fu, S. Ma, P. Zhao, S. Xu and S. Zhan, *Chem. Eng. J.*, 2019, **360**, 157–170.
242 S.-H. Ho, Y.-d. Chen, R. Li, C. Zhang, Y. Ge, G. Cao, M. Ma, X. Duan, S. Wang and N.-q. Ren, *Water Res.*, 2019, **159**, 77–86.
243 C. Liu, L. Chen, D. Ding and T. Cai, *Appl. Catal., B*, 2019, **254**, 312–320.
244 H. Fu, P. Zhao, S. Xu, G. Cheng, Z. Li, Y. Li, K. Li and S. Ma, *Chem. Eng. J.*, 2019, **375**, 121980.
245 S. Zhu, X. Huang, F. Ma, L. Wang, X. Duan and S. Wang, *Environ. Sci. Technol.*, 2018, **52**, 8649–8658.
246 W. Tian, H. Zhang, Z. Qian, T. Ouyang, H. Sun, J. Qin, M. O. Tadé and S. Wang, *Appl. Catal., B*, 2018, **225**, 76–83.
247 C. Wang, J. Kang, P. Liang, H. Zhang, H. Sun, M. O. Tadé and S. Wang, *Environ. Sci.: Nano*, 2017, **4**, 170–179.
248 W.-D. Oh, G. Lisak, R. D. Webster, Y.-N. Liang, A. Veksha, A. Giannis, J. G. S. Moo, J.-W. Lim and T.-T. Lim, *Appl. Catal., B*, 2018, **233**, 120–129.
249 K. Li, Z. Huang, S. Zhu, S. Luo, L. Yan, Y. Dai, Y. Guo and Y. Yang, *Appl. Catal., B*, 2019, **243**, 386–396.
250 S. Ye, M. Yan, X. Tan, J. Liang, G. Zeng, H. Wu, B. Song, C. Zhou, Y. Yang and H. Wang, *Appl. Catal., B*, 2019, **250**, 78–88.
251 H. Zhao, Y. Cheng, W. Liu, L. Yang, B. Zhang, L. P. Wang, G. Ji and Z. Xu, *Nano-Micro Lett.*, 2019, **11**, 24.
252 H. Wang, Z. Xu, A. Kohandehghan, Z. Li, K. Cui, X. Tan, T. J. Stephenson, C. K. King'ondu, C. M. B. Holt, B. C. Olsen, J. K. Tak, D. Harfield, A. O. Anyia and D. Mitlin, *ACS Nano*, 2013, **7**, 5131–5141.
253 F. Sun, L. Wang, Y. Peng, J. Gao, X. Pi, Z. Qu, G. Zhao and Y. Qin, *Appl. Surf. Sci.*, 2018, **436**, 486–494.
254 G. Xu, J. Han, B. Ding, P. Nie, J. Pan, H. Dou, H. Li and X. Zhang, *Green Chem.*, 2015, **17**, 1668–1674.
255 H. Chen, D. Liu, Z. Shen, B. Bao, S. Zhao and L. Wu, *Electrochim. Acta*, 2015, **180**, 241–251.
256 C. Chen, D. Yu, G. Zhao, B. Du, W. Tang, L. Sun, Y. Sun, F. Besenbacher and M. Yu, *Nano Energy*, 2016, **27**, 377–389.
257 Q. Niu, K. Gao, Q. Tang, L. Wang, L. Han, H. Fang, Y. Zhang, S. Wang and L. Wang, *Carbon*, 2017, **123**, 290–298.
258 D. Zhang, G. Wang, L. Xu, J. Lian, J. Bao, Y. Zhao, J. Qiu and H. Li, *Appl. Surf. Sci.*, 2018, **451**, 298–305.
259 B. Liu, H. Chen, Y. Gao and H. Li, *Electrochim. Acta*, 2016, **189**, 93–100.
260 X. Zhang, K. Zhang, H. Li, Q. Cao, L. e. Jin and P. Li, *J. Power Sources*, 2017, **344**, 176–184.
261 X. Zhang, H. Li, K. Zhang, Q. Wang, B. Qin, Q. Cao and L. e. Jin, *J. Electrochem. Soc.*, 2018, **165**, A2084–A2092.
262 W. Tian, Q. Gao, Y. Tan and Z. Li, *Carbon*, 2017, **119**, 287–295.
263 C.-L. Ban, Z. Xu, D. Wang, Z. Liu and H. Zhang, *ACS Sustainable Chem. Eng.*, 2019, **7**, 10742–10750.
264 G. Sun, L. Qiu, M. Zhu, K. Kang and X. Guo, *Ind. Crops Prod.*, 2018, **125**, 41–49.
265 R.-J. Mo, Y. Zhao, M.-M. Zhao, M. Wu, C. Wang, J.-P. Li, S. Kuga and Y. Huang, *Chem. Eng. J.*, 2018, **346**, 104–112.
266 X. Song, X. Ma, Y. Li, L. Ding and R. Jiang, *Appl. Surf. Sci.*, 2019, **487**, 189–197.
267 J. Luo, H. Zhang, Z. Zhang, J. Yu and Z. Yang, *Carbon*, 2019, **155**, 1–8.
268 V. Selvamani, R. Ravikumar, V. Suryanarayanan, D. Velayutham and S. Gopukumar, *Electrochim. Acta*, 2015, **182**, 1–10.
269 Y. Liu, J. Ruan, S. Sang, Z. Zhou and Q. Wu, *Electrochim. Acta*, 2016, **215**, 388–397.
270 G. Wang, Y. Deng, J. Yu, L. Zheng, L. Du, H. Song and S. Liao, *ACS Appl. Mater. Interfaces*, 2017, **9**, 32168–32178.
271 Q. Wei, X. Yang, G. Zhang, D. Wang, L. Zuin, D. Banham, L. Yang, S. Ye, Y. Wang, M. Mohamedi and S. Sun, *Appl. Catal., B*, 2018, **237**, 85–93.
272 N. Wang, T. Li, Y. Song, J. Liu and F. Wang, *Carbon*, 2018, **130**, 692–700.